



**Trinity College Dublin**  
Coláiste na Tríonóide, Baile Átha Cliath  
The University of Dublin

---

# Thermal transport in thin films and across interfaces of dissimilar phase materials

---

Kenny Yu

A thesis presented in partial fulfilment of the requirements

for the degree of

Doctor of Philosophy

School of Physics

Faculty of Engineering, Mathematics and Science

Trinity College

University of Dublin

Academic Supervisor: Professor David McCloskey

Industry Supervisor: Dr Ryan Enright

2023

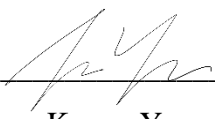
# Declaration

I declare that this thesis has not been submitted as an exercise for a degree at this or any other university and it is entirely my own work.

I agree to deposit this thesis in the University's open access institutional repository or allow the Library to do so on my behalf, subject to Irish Copyright Legislation and Trinity College Library conditions of use and acknowledgement.

I consent to the examiner retaining a copy of the thesis beyond the examining period, should they so wish (EU GDPR May 2018).

Signed:

  
\_\_\_\_\_

Kenny Yu

Date: 30/09/2022

ID No.: 13300855

# Abstract

As electronic and photonic devices steadily become more miniaturised and integrated the power density and heat flux that is required is increasing rapidly. Electronic and photonic circuits are now being integrated on the same chip and require very different thermal management strategies. Microscale thermal management solutions such as thin film thermoelectrics, microfluidics, and nanoporous evaporators are now being considered as they can provide tailored localised thermal management at chip level for hotspot control and thermal tuning of optical components. In addition to handling the higher total heat flux, they are also typically designed to handle localised hot spots which cannot be achieved using conventional macroscale solutions. However, information on the electronic and thermal properties of thin films is often required in the development and design of microscale thermal solutions as thin film properties deviate significantly from bulk. Also, a decrease in device size means that the surface-to-volume ratio increases, therefore interfacial properties begin to dominate over the material properties in thermal transport. Therefore, understanding, predicting, and controlling thermal transport through thin films and across interfaces is critical to the advancement of future integrated microscale thermal management solutions.

In this thesis we develop a custom non-contact thermal measurement technique known as frequency domain thermoreflectance (FDTR) and apply this to quantify a range of thin films and interfaces of interest to integrated microscale thermal management. The first part of this thesis is centred around the use of FDTR to quantify thermal properties to aid in the development of microscale thermoelectric coolers ( $\mu$ TECs). Using kinetic theory and measured thermal properties, the size effect of an electrodeposited  $\text{Bi}_2\text{Te}_3$  thermoelectric film in a development  $\mu$ TEC test device is investigated.

The second part of this thesis focuses on investigating the relationship between thermal transport and wettability across solid-liquid interfaces by using self-assembled monolayer (SAM). The results from FDTR suggest that surface contamination can greatly influence the thermal boundary conductance (TBC), which is beyond being proportional to the thermodynamic work of adhesion.

The third and final part of the thesis focuses on investigating the effect of physisorbed contaminant on interfacial thermal transport by using a known species. In addition to the use of FDTR, we develop a continuum theory to aid the investigation. The experimental and theoretical results shows that the effective Au-H<sub>2</sub>O TBC with a C<sub>9</sub>H<sub>20</sub> interlayer is more than twice lower as compared to Au-H<sub>2</sub>O without an interlayer. The theoretical model shows that the bonding potential energy of the interlayer does indeed play a dominating role in the effective interfacial thermal transport.

# Table of contents

<b>Declaration</b>	<b>ii</b>
<b>Abstract</b>	<b>iii</b>
<b>Publications</b>	<b>viii</b>
<b>Acknowledgements</b>	<b>ix</b>
<b>List of symbols, acronyms, and abbreviations</b>	<b>xi</b>
<b>List of figures</b>	<b>xvi</b>
<b>List of tables</b>	<b>xxii</b>
<b>Chapter 1. Introduction . . . . .</b>	<b>1</b>
1.1 Motivation	1
1.2 Integrated microscale thermal management	4
1.2.1 Microfluidics	4
1.2.2 Thin film thermoelectrics	8
1.2.3 Two-phase evaporators	11
1.3 Thesis outline	13
<b>Chapter 2. Theories and concepts of heat transport . . . . .</b>	<b>16</b>
2.1 Introduction	16
2.2 Heat carriers	16
2.2.1 Phonons, phonon dispersion relations, and phonon density of states	18
2.3 Interfacial heat transport	25
2.3.1 Acoustic mismatch model (AMM)	27
2.3.2 Diffuse mismatch model (DMM)	28
2.4 Summary	30
<b>Chapter 3. Characterisation methods . . . . .</b>	<b>31</b>
3.1 Introduction	31
3.2 Scanning electron microscopy (SEM)	31
3.2.1 Emitted X-ray photons and ejected electrons	32
3.3 Atomic force microscopy (AFM)	33
3.3.1 Operation modes	34
3.4 Four-point probe (4PP)	36
3.4.1 Geometric correction	38
3.4.1 Cox-Strack method	39
3.5 Contact angle goniometry (CAG)	40

3.5.1 Thermodynamic work of adhesion	41
3.6 Frequency-domain thermoreflectance (FDTR)	42
3.6.1 Instrumentation and Optics	44
3.6.2 Spot size characterisation	47
3.6.3 Fabrication and characterisation of thermoreflectance transducer	49
3.6.4 Heat transfer and signal analysis	50
3.6.5 Sensitivity analysis	58
3.6.6 Uncertainty analysis	60
3.7 Summary	62
<b>Chapter 4. Impact of thermal properties on thermoelectric performance . . . . .</b>	<b>64</b>
4.1 Introduction	64
4.2 Materials	66
4.3 Results and discussion	68
4.3.1 Measurement of electrodeposited Bi <sub>2</sub> Te <sub>3</sub> film thermal conductivity	69
4.3.2 Performance of electrodeposited Bi <sub>2</sub> Te <sub>3</sub> thermoelectric device	71
4.3.3 Phonon scattering in electrodeposited Bi <sub>2</sub> Te <sub>3</sub> film	73
4.3.4 Thermal boundary conductance (TBC) across Bi <sub>2</sub> Te <sub>3</sub> -W interface	75
4.4 Conclusions	76
<b>Chapter 5. Effect of wettability on interfacial thermal transport . . . . .</b>	<b>78</b>
5.1 Introduction	78
5.2 Materials and methods	79
5.2.1 Sample preparation and fabrication	79
5.2.2 Bidirectional heat transfer model for thermoreflectance techniques	82
5.2.3 AMM for solid-liquid interfaces	83
5.3 Results and discussions	90
5.3.1 Quantifying effective Au-H <sub>2</sub> O TBC using FDTR and AMM	94
5.3.2 Measurement of effective Au-C <sub>2</sub> H <sub>6</sub> O TBC using FDTR	99
5.4 Conclusions	101
<b>Chapter 6. Effect of alkane interlayer on interfacial thermal transport . . . . .</b>	<b>103</b>
6.1 Introduction	103
6.2 Materials and methods	105
6.2.1 Sample preparation and fabrication	106
6.2.2 AMM for weakly bonded complex solid-liquid interfaces	107
6.3 Results and discussions	110

6.3.1 Measurement of effective Au-C <sub>9</sub> H <sub>20</sub> -H <sub>2</sub> O TBC using FDTR	110
6.3.2 Effect of C <sub>9</sub> H <sub>20</sub> interlayer has on effective Au-H <sub>2</sub> O TBC using AMM	113
6.3.3 Sensitivity in measuring Au-C <sub>9</sub> H <sub>20</sub> TBC using FDTR	118
6.4 Conclusions	120
<b>Chapter 7. Conclusions . . . . .</b>	<b>122</b>
7.1 Summary of the thesis	122
7.2 Outlook for future work	123
7.2.1 Enhancing TR measurement sensitivity	123
7.2.2 Temperature- and pressure-controlled FDTR measurements	125
7.2.3 Liquid-vapour, and steady state studies using FDTR	127
<b>Appendix A</b>	<b>131</b>
Derivation of adhesion energy from surface traction	131
<b>References</b>	<b>133</b>

## Publications

- [I] **K. Yu**, R. Enright, and D. McCloskey, “Effect of alkane interlayer has on thermal transport across solid-liquid interfaces,” *Manuscript submitted to AIP Applied Physics Letters*
- [II] **K. Yu**, R. Enright, and D. McCloskey, “Quantifying interfacial thermal conductance at solid-liquid interfaces using frequency-domain thermorefectance and analytical methods,” in *2022 21st IEEE Intersociety Conference on Thermal and Thermomechanical Phenomena in Electronic Systems (iTherm)*, 2022, pp. 1-6, doi: 10.1109/iTherm54085.2022.9899691.
- [III] S. Corbett, D. Gautam, S. Lal, **K. Yu**, N. Balla, G. Cunningham, K. M. Razeeb, R. Enright, and D. McCloskey, “Electrodeposited Thin-Film Micro-Thermoelectric Coolers with Extreme Heat Flux Handling and Microsecond Time Response,” *ACS Appl. Mater. Interfaces*, 2021, vol. 13, no. 1, 1773–82, doi: 10.1021/acsami.0c16614
- [IV] **K. Yu**, R. Enright, and D. McCloskey, “Monte Carlo analysis of frequency domain thermorefectance data for quantitative measurement of interfacial thermal conductance at solid-liquid interfaces modified with self-assembled monolayers,” in *Journal of Physics: Conference Series*, 2021, vol. 2116, no. 1, doi: 10.1088/1742-6596/2116/1/012042.
- [V] P. Darragh, **K. Yu**, M. Morris, D. McCloskey, and R. Enright, “Quantifying Enhanced Interfacial Thermal Conductance At Solid-Fluorocarbon Liquid Interfaces Modified With Self-Assembled Monolayers,” in *Proc. of the Int. Symp. on Therm. Effects in Gas flow in Microscale*, 2019, pp. 1–14, [istegim2019.sciencesconf.org/283392](http://istegim2019.sciencesconf.org/283392).



# Acknowledgements

Completing a PhD and writing a thesis can be an insurmountable challenge, but with the support and advice of the amazing people in my life, I have been able to learn more than I ever thought possible.

First and foremost, I would like to thank my supervisors, Dave McCloskey and Ryan Enright, for giving me the opportunity and the fantastic experience. I am forever grateful for the continuous guidance and support throughout my time at Trinity College and Bell Labs. Dave and Ryan helped me become a better researcher, writer, and even a better person.

I want to thank Naveen Balla for being a fantastic teacher and role model. His endless patience as my optics teacher has been instrumental in my success over the past four years.

I want to thank Simon Corbett. Not only has Simon unfailingly been happy to advise or discuss my research, but his support has included fixing my lab door, so accidental door slamming no longer undid my sensitive optical work.

I want to thank Chris Murray for all the advice and inexhaustible assistance and my chemistry counterpart, Philip Darragh, for his collaboration and for his company during our many trips to buy sandwiches and chips. I would like to thank Erik Soderholm, and, more recently, Eoin Cotter, Evan Roy, Nishtha Shelly for keeping me company in SNIAM and Oskar Ronan for always making me laugh in CRANN.

I want to extend my thanks to Shenghui Lei for the short but valuable life and career advice at Bell Labs, and I would like to express my gratitude to my ex- and future Intel colleagues Dave White, Alan Jacob, and Andy Murray for their continuous support and encouragement.

Most importantly, I would like to thank my lovely partner, Megan. Without her unconditional love and support, I would not have made it this far. Although she always thinks I am always right, little does she know she is, in fact, the one who is always right. I admire her incredible emotional intelligence, unparalleled creativity and thoughtfulness. Thank you for always being there for me.

I would like to thank my family Poling Wong, Shunhin Yu, Szeming Yu, and Szeman Yu and all my family and friends around the world.

And finally, I would like to acknowledge and thank the Irish Research Council for funding my project; the funding and support is deeply appreciated.

# List of symbols, acronyms, and abbreviations

## Symbols

$a$	lattice constant [m]
$\psi$	wave function
$A$	amplitude
$t$	time [s]
$k$	wavenumber [ $\text{m}^{-1}$ ]
$\lambda$	wavelength [m]
$\omega$	angular frequency [rad/s]
$f$	ordinary frequency [Hz]
$K$	spring constant [ $\text{N m}^{-1}$ ]
$E$	Energy [J or $\text{kg m}^2 \text{s}^{-2}$ ]
$\hbar$	reduced Planck constant [J s]
$h$	Planck constant [ $\text{J Hz}^{-1}$ ]
$i$	indexing integer
$m$	mass [kg]
$\mathbf{k}$	wavevector [ $\text{m}^{-1}$ ]
$\mathcal{D}$	phonon density of states
$\mathcal{N}$	number of states
$\rho_N$	number density [ $\text{m}^{-3}$ ]
$v$	velocity [ $\text{m s}^{-1}$ ]
$j$	phonon branch indices
$G$	thermal boundary conductance [ $\text{W m}^{-2} \text{K}^{-1}$ ]
$T$	temperature [K]
$q$	heat flux [ $\text{W m}^{-2}$ ]
$z$	cross-plane coordinate [m]
$\mathcal{T}$	phonon transmission probability
$f^0$	equilibrium carrier distribution function
$\theta$	azimuth angle [degree]
$\varphi$	elevation angle [degree]
$k_B$	Boltzmann constant [ $\text{J K}^{-1}$ ]

$\mathcal{M}$	number of allowable phonon modes
$c$	heat capacity [J K <sup>-1</sup> ]
$Z$	acoustic impedance [kg m <sup>-2</sup> s <sup>-1</sup> ]
$d$	distance [m]
$I$	current [A]
$V$	voltage [V or kg m <sup>2</sup> s <sup>-3</sup> A <sup>-1</sup> ]
$C$	correction factor
$\mathcal{R}$	electrical resistance [ $\Omega$ ]
$\rho_r$	electrical resistivity [ $\Omega$ m or V m A <sup>-2</sup> ]
$\sigma_c$	electrical conductivity [S m <sup>-1</sup> or A <sup>2</sup> V <sup>-1</sup> m <sup>-1</sup> ]
$\kappa$	thermal conductivity [W m <sup>-1</sup> K <sup>-1</sup> ]
$L$	Lorenz number [W $\Omega$ K <sup>-2</sup> ]
$\gamma$	interfacial energy [J m <sup>-2</sup> ]
$\Delta\gamma$	work of adhesion [J m <sup>-2</sup> ]
$C_V$	volumetric heat capacity [J m <sup>-3</sup> K <sup>-1</sup> ]
$\rho$	mass density [kg m <sup>-3</sup> ]
$c_p$	specific heat capacity [J kg <sup>-1</sup> K <sup>-1</sup> ]
$\kappa_{TR}$	thermoreflectance coefficient [K <sup>-1</sup> ]
$R$	reflectivity
$n$	refractive index
$k_\epsilon$	extinction coefficient [m <sup>-1</sup> ]
$w$	beam waist radius [m]
$I_V$	intensity [W m <sup>-2</sup> ]
$P$	power [W]
$M$	magnification factor
$\perp$	in-plane
$\parallel$	cross-plane
$\phi$	phase [rad]
$i$	complex number
$Z$	transfer function
$\alpha_{gr}$	product of photodetector gain and photodiode responsivity
$k_H$	Hankel transform variable

<b>M</b>	matrix
$J$	Bessel function of the first kind
$l_d$	thermal diffusion length [m]
$\alpha_d$	thermal diffusivity [ $\text{m}^2 \text{s}^{-1}$ ]
$U$	potential energy [J]
$\varepsilon$	depth of the potential well [J]
$\sigma$	distance at which the interparticle potential vanishes [m]
$r$	distance between centre of particles [m]
$F$	force [N or $\text{kg m s}^{-2}$ ]
$ZT$	thermoelectric figure of merit
$S$	Seebeck coefficient [ $\text{V K}^{-1}$ ]
$\eta$	efficiency
$u$	fluid velocity [ $\text{m s}^{-1}$ ]
$d$	distance [m]
$w$	$1/e^2$ beam radius [m]
$\sigma_{\text{sd}}$	standard deviation
$\alpha_{\text{gr}}$	product of the gain and responsivity of the photodetector and photodiode, respectively
$H$	frequency response
$\mathcal{G}$	Green's function
$I_V$	energy intensity
$\mathcal{S}$	sensitivity [radians]
$f_x$	probability density function
$CI$	confidence interval
$\mu$	mean value
$j$	indexing integer
$\ell$	mean free path [m]
$M_u$	molar mass [ $\text{g mol}^{-1}$ ]
$N_A$	Avogadro constant [ $\text{mol}^{-1}$ ]
$\tau_\alpha$	viscoelastic relaxation time [s]
$G_\infty$	infinite-frequency shear modulus [ $\text{Pa}$ or $\text{kg m}^{-1} \text{s}^{-2}$ ]
$\eta$	shear viscosity [ $\text{m}^2 \text{s}^{-1}$ ]
$C_H$	Hamaker constant

$\Gamma$  average energy transmission

## Acronyms

$3\omega$	3-omega
4PP	four-point probe
AC	alternating current
AFM	atomic force microscopy
AMM	acoustic mismatch model
CAG	contact angle goniometry
CCD	charge-coupled device
CCD-TR	charge-coupled device based thermorefectance
CPU	central processing unit
CW	continuous wave
DC	direct current
DMM	diffuse mismatch model
DOS	density of states
FCC	face-centred cubic
FCC	face-centred cubic
FDTR	frequency-domain thermorefectance
FESEM	field emission scanning electron microscopy
FWHM	full width at half maximum
HPLC	high performance liquid chromatography
LA	longitudinal acoustic
OI	optical isolator
PSF	point spread function
RMS	root mean square
RTD	resistance temperature detector
SAM	self-assembled monolayers
SEM	scanning electron microscopy
TA	transverse acoustic
TBC	thermal boundary conductance
TBR	thermal boundary resistance
TDTR	time-domain thermorefectance

TEC	thermoelectric cooler
TIM	thermal interface material

### Abbreviations and chemical formulas

1DT	1-Decanethiol, $\text{CH}_3(\text{CH}_2)_9\text{SH}$
Al	aluminium
$\text{Al}_2\text{O}_3$	aluminium oxide
Au	gold
$\text{Bi}_2\text{Te}_3$	bismuth telluride
$\text{C}_2\text{H}_6\text{O}$	ethanol
$\text{C}_9\text{H}_{20}$	nonane
$\text{CH}_2\text{I}_2$	diiodomethane
GaN	gallium nitride
$\text{H}_2\text{O}$	water
n-type	negatively dopped
PFDT	1H,1H,2H,2H-Perfluorodecanethiol, $\text{CF}_3(\text{CF}_2)_7\text{CH}_2\text{CH}_2\text{SH}$
Pt	platinum
p-type	positively dopped
Si	silicon
$\text{SiO}_2$	silicon dioxide
$\text{TEM}_{00}$	lowest-order transverse mode
Ti	titanium
W	tungsten

# List of figures

- Figure 1.1: Electronic chip power and heat flux trend over the past two decades. Taken from literature [11]. 2
- Figure 1.2: Key material properties differences between GaN and Si for electronic and photonic devices. Taken from literature [20]. 4
- Figure 1.3: Typical schematic illustration of a CPU being cooled using a cold plate, where TIM is used to act as a thermal bridge between the CPU and the cold plate. Taken from literature [23]. 5
- Figure 1.4: GaN based AC-DC converter. (a) Schematic illustration of integrated manifold microchannels. (b) Conversion efficiency versus power of the air-cooled, and (c) temperature rise versus power of the air-cooled and liquid-cooled AC-DC converter. Taken from literature [24]. 6
- Figure 1.5: Boundary layer development of working fluid flowing along a heated surface. Taken from literature [26]. 7
- Figure 1.6: Schematic of a typical photonic device with last generation state-of-the-art thermal management solution. Taken from literature [32]. 8
- Figure 1.7: Schematic diagram of a single thermoelectric module. Adapted from literature [34]. 9
- Figure 1.8: Bulk and thin film thermoelectric performance chart. Adapted from literature [36]. 10
- Figure 1.9: Illustration of a cross-sectional view of a typical heat pipe. Working fluid evaporates on the hot side, then the vapor travels to the cold side and condenses onto the cold surfaces. After the condensation process, working fluid are circulated back to the hot side via capillary action. Taken from literature [37]. 12
- Figure 1.10: Schematic of a nanoporous membrane two-phase microscale evaporator design. Taken from literature [10]. 13
- Figure 2.1: (a) A simple schematic of an oscillatory motion of atoms along a short monatomic lattice with spring constant,  $K$ , for a longitudinal acoustic wave. (b) A truncated plane wave using Eq. (2.1). (c) A representation of a wave group. (d) A representation of a gas of phonon particles. 18
- Figure 2.2: Dispersion relation for spring-mass array of: (a) a monatomic chain; (b) a diatomic chain. 21
- Figure 2.3: (a) First Brillouin zone and high symmetry points for FCC structure. (b) Phonon dispersion curves for bulk Au along with the associated phonon DOS, where the plot is taken from literature [50]. The theoretical estimations of the phonon DOS were calculated using a fourth-neighbour general force constants model [51] and the



experimental data were measured using the plasmon resonant Raman scattering method [50].	22
Figure 2.4: (a) A comparison between dispersion relation for a monatomic chain with and without Debye approximation (b) A comparison between the phonon DOS of Au from theory, experiment, and Debye approximation, where the results from theory and experiment are taken from literature [50], [51]. The dash and solid vertical lines represent the transverse and longitudinal cutoff frequency, respectively.	24
Figure 3.1: A schematic of a scanning electron microscope.	32
Figure 3.2: A simple schematic illustration of electron-matter interaction volume when an electron beam strikes a sample surface. Adapted from literature [69].	33
Figure 3.3: A schematic of an atomic force microscope, where the reflected beam picked up by the photodetector is used for analysis and to simultaneously provide a feedback signal to finely adjust the cantilever height or vibrate via a piezoelectric device.	35
Figure 3.4: Dimensionless Lennard-Jones potential as a function of interparticle distance. The highlighted regions indicate the respective LJ potential regime for each AFM operation mode.	36
Figure 3.5: Schematic of an 4PP array configuration, where $d_l$ and $d_w$ are the length and width of the rectangular material, $d_t$ is thickness and $d_s$ is the spacing between probe needles. A current $I$ is sourced between the outer electronics and the potential drop across the inner electronics is measured.	37
Figure 3.6: (a) Schematic cross-sectional view of a typical multilayer test device with test layer thickness $d_t$ . (b) A plan view of the same test device in (a) with circular contact pad diameter $d_d$ . Probe needles $P_1$ and $P_2$ are positioned in contact with the top contact pad, while $P_3$ and $P_4$ are in contact with the substrate or backside of the layer of interest if possible.	39
Figure 3.7: A schematic of a contact angle goniometer, with manual focusing microscope.	41
Figure 3.8: (a) Absorbance, and (b) thermoreflectance spectrum over a range of wavelengths, where the dashed lines indicate negative values. Taken from literature [105].	44
Figure 3.9: (a) A schematic of the FDTR setup used in this work. A charge-coupled device (CCD) camera is used check that the pump and probe beams are coaxially aligned and Gaussian-shaped. Optical isolators (OI) are used to prevent unwanted feedback into the respective laser cavity. Matching detectors, cables, and optical paths for the pump and probe beams are used and practiced, respectively, to minimize additional phase difference to the measured phase response. (b) Picture of the FDTR setup that was built in the Nanothermal Research Group optical characterisation lab.	45

- Figure 3.10: (a) A 10  $\mu\text{m}$  radius pillar from an ultra-high precision micro-pillar matrix sample fabricated by Ryan Enright was used to calibrate the first CCD camera for spot size measurements. (b) An example of the pump and probe spot size imaged using the calibrated CCD camera and their respective cross section, where the circle markers and solid lines represent data and fit (using `ezfit` Matlab function [109]), respectively. 49
- Figure 3.11: A 3D AFM image of a typical Au transducer surface fabricated using the Ferrotec Temescal FC-2000 electron beam evaporation system. 50
- Figure 3.12: A schematic of a multi-layered stacked structure with parameters for each layer in the heat diffusion model. The red region on top of layer  $i = 1$  represents a Gaussian heat source applied on the surface by the pump and probe beams. Quantities with subscript  $\perp$  or  $\parallel$  are the in-plane or cross-plane, and are perpendicular or parallel relative to the pump beam, respectively. For isotropic materials, in-plane thermal conductivity and cross-plane thermal conductivity are equal. The TBC in the model is the TBC between the layer of interest and the next layer. 51
- Figure 3.13: A typical FDTR phase lag data and fit for a fused silica sample with 90 nm thick Au transducer layer on top. The thermal conductivity of the  $\text{SiO}_2$  was fitted to be  $\kappa = 1.38 \text{ W m}^{-1} \text{ K}^{-1}$  using Eq. (3.45). 58
- Figure 3.14: Using the measured values of the Au- $\text{SiO}_2$  sample: (a) A phase difference plot, where the phase difference is calculated by subtracting the phase lag with -10%  $\text{SiO}_2$  thermal conductivity to the phase lag with +10%  $\text{SiO}_2$  thermal conductivity. (b) Theoretical sensitivity to the  $\text{SiO}_2$  thermal conductivity and volumetric heat capacity, and the TBC across Au- $\text{SiO}_2$  interface were calculated using Eq. (3.47). 59
- Figure 3.15: A flow chart of the Monte Carlo method being applied to FDTR data, where the missing vertical axis is the count scale, and the horizontal axis is the parameter value scale with their respective unit. Adapted from literature [127]. 61
- Figure 4.1: (a) Schematic cross section of single thermoelectric device structure. (b) Plan view image of a single 87  $\mu\text{m}$  square diameter pad. (c) A cross section SEM image about the 20  $\mu\text{m}$  circular pad. (d) A cross section SEM image about the centre of the 20  $\mu\text{m}$  circular pad with higher magnification compared to (c) a cross-section of the metal interfaces. 68
- Figure 4.2: Measured phase lag data and fit using Eq. (3.45) for the  $\text{Bi}_2\text{Te}_3$  based thermoelectric test device with 200 nm thick Au transducer on top. 69
- Figure 4.3: Thermal conductivity distribution and fit (using `lognfit` Matlab built-in function) of the measured  $\text{Bi}_2\text{Te}_3$  film, where solid lines represent mean, while dotted and dashed lines represent the lower and upper confidence intervals at 95%, respectively. 70
- Figure 4.4: (a) A phase difference plot, where the phase difference is calculated by subtracting the phase lag with -10%  $\text{Bi}_2\text{Te}_3$  thermal conductivity and volumetric heat capacity, respectively, while holding other parameters constant. (b) Theoretical

sensitivity to the thermal conductivity and volumetric heat capacity calculated using Eq. (3.47) based on the measured values for the thermoelectric test device.	71
Figure 4.5: Electrical conductivity and contact resistance measurements [140]. (a) Plan view optical images of the test pads. (b) Measured four-point resistance as a function of pad diameter and fit using Eq. (3.7). (c) Total resistance as a function of reciprocal pad diameter squared and the effect of contact resistance on total resistance.	73
Figure 4.6: Predicted TBC across $\text{Bi}_2\text{Te}_3$ -W interface as a function of temperature using Eq. (2.21) and (2.23) with acoustic values in Table 4.2, and experimental measurement of the TBC at room temperature using FDTR.	76
Figure 5.1: Simple structure diagrams of the investigated thiolated SAMs: (a) 1-Decanethiol (1DT). (b) 1H,1H,2H,2H-Perfluorodecanethiol (PFDT). Adapted from CRC Handbook of Chemistry and Physics [155]	80
Figure 5.2: Process steps for adhesion of SAM to Au surface.	81
Figure 5.3: Image of the liquid cell installed in the beam line of the custom FDTR setup.	82
Figure 5.4: Simple schematic of (a) a typical liquid cell structure, and (b) the bidirectional heat flow problem associated to the liquid cell structure separated into simpler and smaller multiple unidirectional heat flow problems. For clarity, a layer of $\text{SiO}_2$ is present on top of the liquid layer to incapsulate the working fluid and to observe the solid-liquid interface using CCD 2 through a second fluorescence microscope setup (see Figure 3.9). The $\text{SiO}_2$ can be neglected as the liquid layer is several microns thick and can be considered semi-infinite in the heat diffusion model.	83
Figure 5.5: Schematic illustration of the different set of acoustic propagation in frequency regime below and above Frenkel frequency for a liquid, where the longitudinal and transverse acoustic velocities in their respective frequency regime can be identified by the variable subscript. Adapted from literature [170].	87
Figure 5.6: Schematic illustration of energy transmission across solid-solid interface.	88
Figure 5.7: Simplified illustration of interfacial phonon processes: (a) 2-phonon scattering (i.e., elastic). (b) N-phonon scattering (i.e., inelastic).	89
Figure 5.8: AFM images of (a) $5 \times 5 \mu\text{m}$ , and (b) $1 \times 1 \mu\text{m}$ of Au, 1DT, and PFDT, respectively.	91
Figure 5.9: Advancing contact angle images for $\text{H}_2\text{O}$ , and diiodomethane ( $\text{CH}_2\text{I}_2$ ) on bare Au, 1DT, and PFDT, respectively. For scale reference, the dispensing needle has an outer diameter of $135 \mu\text{m}$ .	93
Figure 5.10: (a) Contact angle measurements for advancing and receding behaviour of $\text{H}_2\text{O}$ on 1DT, PFDT and bare Au. (b) Surface energies of 1DT, PFDT, and bare Au	

determined using the Fowkes method [181], [182] with advancing contact angle of H<sub>2</sub>O, and CH<sub>2</sub>I<sub>2</sub>. 94

Figure 5.11: Au transducer surface of a liquid cell observed from (a) CCD 1 (Au-SiO<sub>2</sub> interface) and indication of the locations of three sites measured in red, green, and blue, respectively. Surfaces in (b), (c), and (d) were observed through CCD 2 (Au-water interface), where some of the transmitted probe spot can be seen from CCD 2. CCD 1 is located on the FDTR side, while CCD 2 is from the second fluorescence microscope setup. 95

Figure 5.12: Schematic of a multilayered liquid cell sample structure interposed with SAM. The three terms are the resistances that makes up the effective Au-H<sub>2</sub>O TBR. 96

Figure 5.13: Thermal boundary conductance distribution of Au-PFDT-H<sub>2</sub>O, Au-1DT-H<sub>2</sub>O, and Au-H<sub>2</sub>O using Monte Carlo method [185], where solid lines represent mean, while dotted and dashed lines represent the lower and upper confidence intervals at 95%, respectively. 97

Figure 5.14: Effective TBC across Au-water interface as a function of the dimensionless work of adhesion. The lines represent the analytical model, unfilled markers represent simulation data, and filled markers represent experimental data. 99

Figure 5.15: Effective TBC across Au-C<sub>2</sub>H<sub>6</sub>O interface with and without hydrogenated SAMs. TDTR data taken from literature [156]. 101

Figure 6.1: Nonane: (a) Line drawing, and (b) ball and stick model. Adapted from CRC Handbook of Chemistry and Physics [155] 105

Figure 6.2: Schematic of multilayered liquid cell sample structure with C<sub>9</sub>H<sub>20</sub> interlayer. The laser induced heating spreads in all directions within the Au transducer. 107

Figure 6.3: Schematic illustration of the energy transmission across solid-nonane-liquid interfaces. 109

Figure 6.4: Schematic of multilayered liquid cell sample structure with C<sub>9</sub>H<sub>20</sub> interlayer. The three terms are the resistances that makes up the effective Au-H<sub>2</sub>O TBR. 110

Figure 6.5: (a) Measured phase lag data and fit (using Eq. (3.45)) for Au-SiO<sub>2</sub>, Au-H<sub>2</sub>O, and Au-C<sub>9</sub>H<sub>20</sub>-H<sub>2</sub>O samples. (b) Theoretical sensitivity to the thermal conductivity, volumetric heat capacity, and effective TBC were calculated using Eq. (3.47) based on the measured values for the SiO<sub>2</sub>-Au-C<sub>9</sub>H<sub>20</sub>-H<sub>2</sub>O-SiO<sub>2</sub> liquid cell. 112

Figure 6.6: (a) Advancing, and (b) receding contact angle images for H<sub>2</sub>O on C<sub>9</sub>H<sub>20</sub> saturated surfaces. 113

Figure 6.7: Average transmission at Au-C<sub>9</sub>H<sub>20</sub> interfaces; exit angle independent, and dependent average transmission at C<sub>9</sub>H<sub>20</sub>-H<sub>2</sub>O, and effective Au-C<sub>9</sub>H<sub>20</sub>-H<sub>2</sub>O interfaces, respectively. The dotted, dashed, and solid black line marks the Frenkel frequency of the H<sub>2</sub>O, Au transverse cutoff frequency, and Au longitudinal cutoff frequency, respectively. 114

- Figure 6.8: Overall TBC as a function of the intermediate layer's Lennard-Jones potential parameters with selected acoustic impedances using (a) Debye frequencies of the solid, and (b) Debye frequencies of the harder medium as defined in Section 5.2.3. 116
- Figure 6.9: AMM predictions and FDTR measurements of the effective Au-C<sub>9</sub>H<sub>20</sub>-H<sub>2</sub>O and Au-H<sub>2</sub>O TBC, respectively. The lower and upper bounds of the AMM predictions are calculated using the elastic and inelastic limits, respectively; while for FDTR, two-sigma standard deviations are presented using the Monte Carlo method described in Section 3.6.6. The dashed and dash-dotted lines are experimental data of Au-H<sub>2</sub>O with near-superhydrophobic using CH<sub>3</sub> terminated SAM and near-superhydrophilic using COOH terminated SAM surfaces, respectively, reported by Harikrishna *et al.* [157]. 118
- Figure 6.10: Theoretical sensitivity to the thermal conductivity, and TBC were calculated using Eq. (3.47) based on the measured values for the SiO<sub>2</sub>-Au-H<sub>2</sub>O-SiO<sub>2</sub> and SiO<sub>2</sub>-Au-C<sub>9</sub>H<sub>20</sub>-SiO<sub>2</sub> liquid cells, respectively. 119
- Figure 6.11: Sensitivity plot for TBC, where the dotted lines refers to the sensitivity of Au-H<sub>2</sub>O TBC, and Au-C<sub>9</sub>H<sub>20</sub> TBC when the support substrate (i.e., SiO<sub>2</sub>) thermal conductivity is artificially reduced to 10% of the bulk value, respectively. 120
- Figure 7.1: Sensitivity plot for working fluid thermal conductivity with structure SiO<sub>2</sub>-Au-H<sub>2</sub>O-SiO<sub>2</sub>, SiO<sub>2</sub>-Au-245fa-SiO<sub>2</sub>, and SiO<sub>2</sub>-aerogel-Au-245fa-SiO<sub>2</sub> with aerogel thickness 10 nm, 100 nm, 500 nm, and 1000 nm, respectively. Theoretical sensitivity to the thermal conductivities were calculated using Eq. (3.47) based on the measured values. The thermal conductivity value used for R-245fa is 0.88 W m<sup>-1</sup> K<sup>-1</sup> which is taken from the product data sheet [199]. 125
- Figure 7.2: (a) Solid, and (b) wireframe view of the mini environmental chamber designed using SolidWorks to experimentally characterise and test the thermal properties and performance of 3D die stacked architectures, respectively. 126
- Figure 7.3: Schematic illustration of a syringe pump-based microchannel flow loop. Taken from literature [206]. 128
- Figure 7.4: An illustration each stage of the ebullition cycle of a single vapor microbubble due to laser induced heating. Taken from literature [205]. 128
- Figure 7.5: Schematic of multilayered liquid cell sample structure with Al<sub>2</sub>O<sub>3</sub> nanostructured superhydrophilic surface along with a SEM image of the Al<sub>2</sub>O<sub>3</sub> surface morphology. 129
- Figure 7.6: A temperature rise observation plot using the FDTR, where the solid, dashed, dash-dotted and dotted lines represent the instance for nucleation point, pump laser off, probe laser off and both lasers on, respectively. The amplitude difference between the starting point and ending point is due to dewetting from excessive power used to stimulate nucleation. 130

# List of tables

Table 1.1: A comparison between $3\omega$ , TDTR, FDTR, where $\kappa$ is the thermal conductivity, and $G$ is the thermal boundary conductance [18].	3
Table 3.1. Summary of AFM operation modes [76].	34
Table 4.1. Thermoelectric characterisation in <i>Electrochimica Acta</i> (2000-2020), where 36 data sets were collected by Corbett [137].	66
Table 4.2: Acoustic and thermodynamic parameters used in DMM calculations. The acoustic velocities of $\text{Bi}_2\text{Te}_3$ are taken from literature [152]. The remaining parameters are taken from the CRC Handbook of Chemistry and Physics [153].	76
Table 5.1: Acoustic and thermodynamic parameters used in AMM calculations. *Calculated using Eq. (4.5).	90
Table 5.2: Measured thermal conductivity and TBC for $\text{C}_2\text{H}_6\text{O}$ in contact with bare Au, 1DT, and PFDT, respectively.	100
Table 6.1: Acoustic and thermodynamic parameters used in AMM calculations. *Extrapolated by assuming nonane longitudinal, and transverse sound velocities having a similar relationship to the adiabatic sound velocity as water. **Calculated using Eq. (4.5).	110

*This thesis is dedicated to my mother*





# Chapter 1.

## Introduction

### 1.1 Motivation

As the electronics devices are steadily becoming more miniaturised and integrated there is a commensurate increase in power density and heat flux which must be effectively dissipated. This trend means that heat dissipation is becoming a critical design aspect even at the chip level [1]–[3]. Modern integrated photonic devices also present unique thermal management problems requiring removal of high heat flux, fast time response, and stringent temperature stability and control [4]. These requirements are difficult to solve using conventional macroscopic thermal management solutions (i.e., natural convection [5], and forced convection [6]). As such, major advancements in integrated thermal management solutions such as microheaters [7], thin film thermoelectrics [8], microfluidics [9], and two-phase evaporators [10] could lead to a technological leap in on-chip electronic and photonic devices. Figure 1.1 shows that power and heat flux of electronic devices are progressively creeping up over the past two decades.

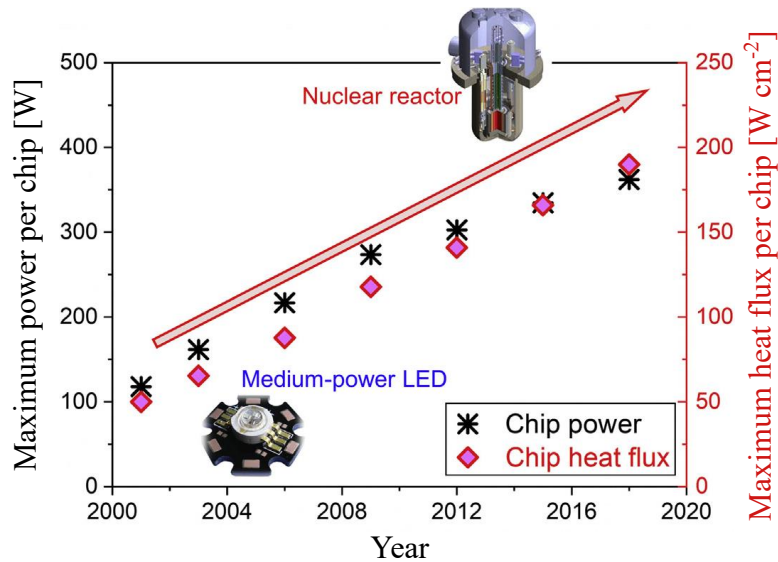


Figure 1.1: Electronic chip power and heat flux trend over the past two decades. Taken from literature [11].

Transitioning from macroscopic to microscopic integrated thermal management solutions could be very challenging and this work is motivated by the following two key reasons.

- Thin film properties: Device designs utilising thin film material will need to be investigated rigorously as thin film properties deviate significantly from bulk [12]. This means that small fabrication deviation from design could lead to a large thermal performance impact.
- Interfacial properties: Decrease in device size means that the surface-to-volume ratio increases, therefore interfacial properties begin to dominate over the material properties in such systems. Unfortunately, precisely controlling [13] and understanding [14] interfacial thermal transport is nontrivial.

While thermal transport and properties of embedded solid thin films can be studied using first principles approaches [15], [16], there is no experimental equivalent. Empirical approaches are usually used to determine the overall thermal performance of a system [17].

However, there are three widely accepted techniques used to measure thermal properties of thin films, namely 3-omega ( $3\omega$ ), time-domain thermoreflectance (TDTR), and frequency-domain thermoreflectance (FDTR) [18]. Table 1.1 shows a comparison between the three thin film capable thermal measurement techniques, where details in the table will be discussed in Section 3.6.

Table 1.1: A comparison between  $3\omega$ , TDTR, FDTR, where  $\kappa$  is the thermal conductivity, and  $G$  is the thermal boundary conductance [18].

	$3\omega$	TDTR	FDTR
Probing method	Metal bridge	Non-contact	Non-contact
Sensitive	$\kappa$	$\kappa, G$	$\kappa, G$
Mechanical stage problem	No	Yes	No
Modulation frequency	$0.05 < f < 200$ kHz	$f \sim 1 - 10$ MHz	$0.1 < f < 20$ MHz
Thermal diffusion length	$400 > l_d > 1$ $\mu\text{m}$	$l_d \sim 1 - 0.3$ $\mu\text{m}$	$30 > l_d > 0.2$ $\mu\text{m}$

This thesis will have a focus on the FDTR optical metrology technique to inform about the thermal properties and to better understand thermal transport in thin films and across dissimilar interfaces of systems for thermal management applications. FDTR has the advantage of being non-contact, it has no moving parts simplifying the alignment process, and it does not require expensive pulsed lasers system such as those used in TDTR. Three main microscopic integrated thermal management solutions are described in the following section, Section 1.2.

## 1.2 Integrated microscale thermal management

### 1.2.1 Microfluidics

With climbing demands for power, efficiency, and smaller form factor in electronic and photonic devices, wide-bandgap semiconductor materials such as gallium nitride (GaN) have become popular candidates recently in replacing silicon (Si) [19]. Figure 1.2 shows that GaN possess several favourable material characteristics over Si for advancing electronic and photonic technologies. However, one of the major hurdles in using GaN is to achieve sustainable thermal management for high heat flux applications.

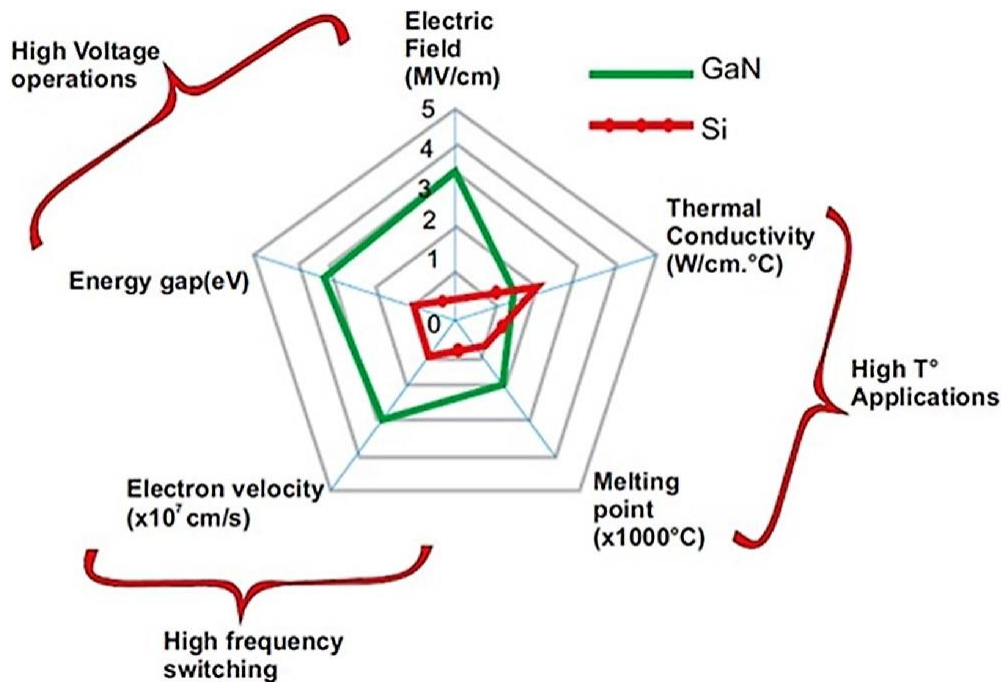


Figure 1.2: Key material properties differences between GaN and Si for electronic and photonic devices. Taken from literature [20].

Typically, Si based electronic devices such as central processing units (CPUs) in data centres are liquid cooled using a cold plate as shown Figure 1.3. Heat is transferred from the CPU and through the thermal interface material (TIM) to the cold plate, where the heat is then absorbed and carried away by the working fluid without phase change. However, even

current thermal design power data centre CPUs call for novel TIMs to create a better thermal bridge between a CPU and cold plate [21], and novel approaches in cold plate designs to remove the transferred heat for better performance, efficiency, and reliability [22].

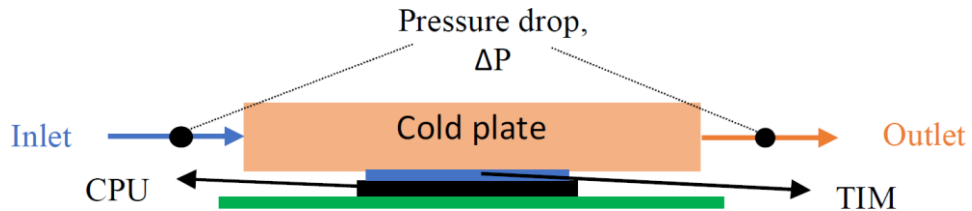
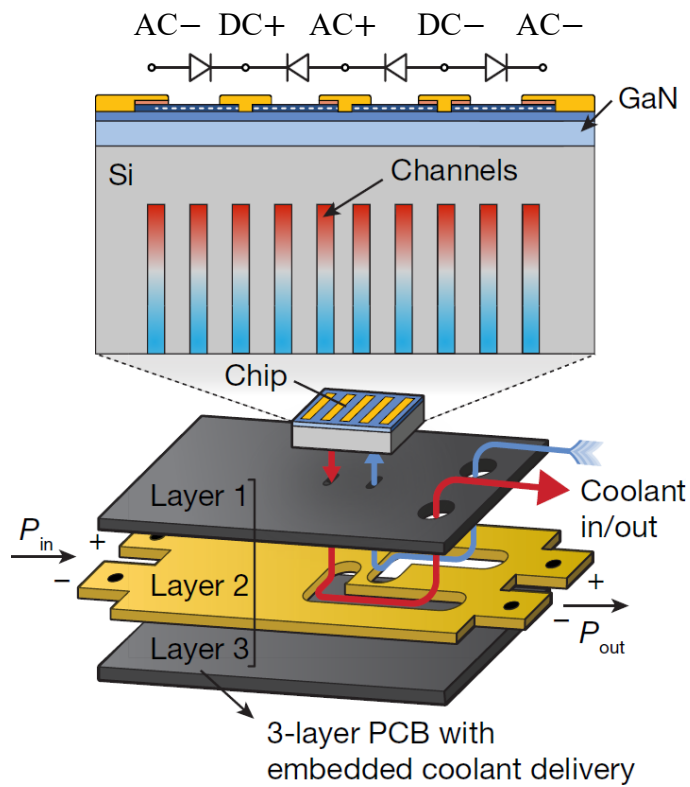


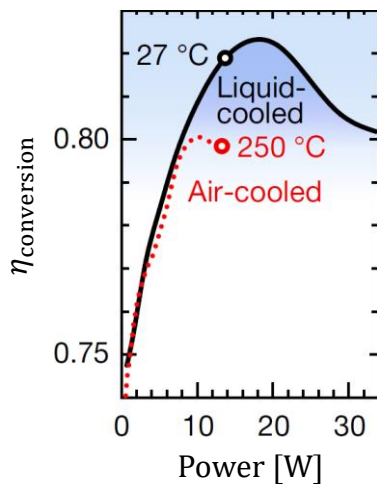
Figure 1.3: Typical schematic illustration of a CPU being cooled using a cold plate, where TIM is used to act as a thermal bridge between the CPU and the cold plate. Taken from literature [23].

To effectively remove high heat flux of GaN based devices, integrated microfluidics are proposed to bypass any inherent thermal resistance when using TIM [24]. Figure 1.4(a) shows how a GaN based alternating current (AC) to direct current (DC) converter can be cooled using manifold microchannels. Figure 1.4(b) shows the AC-DC conversion efficiency,  $\eta_{\text{conversion}}$ , is limited by heat dissipation capability. While Figure 1.4(c) shows that operating the AC-DC converter using manifold microchannels operates with temperature rise,  $\Delta T$ , well below that of the air-cooled solution. Reducing the temperature rise of the device not just improves on efficiency, but also increases device longevity [25].

(a)



(b)



(c)

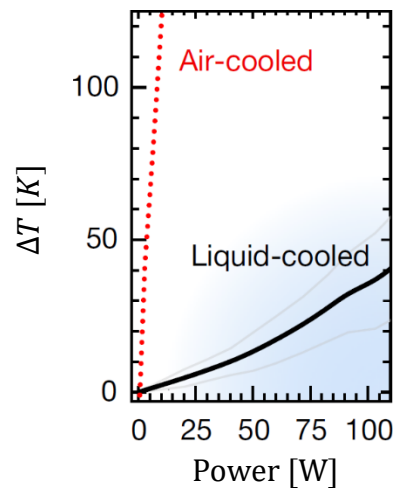


Figure 1.4: GaN based AC-DC converter. (a) Schematic illustration of integrated manifold microchannels. (b) Conversion efficiency versus power of the air-cooled, and (c) temperature rise versus power of the air-cooled and liquid-cooled AC-DC converter. Taken from literature [24].

Achieving a low pressure drop and a small temperature gradient are major challenges in microfluidic channel designs [24], as a higher pressure drop would require higher pumping power to sustain the flow rate, and a higher temperature gradient means that there

is non-uniform cooling. Reducing the pressure drop and attaining better temperature uniformity cannot simply be achieved just by increasing the number of parallel microchannels while occupying the same space. More microchannels means channel dimensions must be smaller, thus fluid flow could be heavily impacted by size effect. A rich list of different types of microchannel designs for managing heat flux  $> 0.1 \text{ kW cm}^{-2}$  can be found elsewhere [2]. Figure 1.5 shows the boundary layer development of a working fluid flowing along a heated surface with flux,  $q$ . Fluid velocity,  $u$ , and local temperature,  $T$ , are both functions of distance,  $y$ , away from the heated surface. The fluid velocity typically approaches to zero at the surface as the adhesion energy is greater than cohesion energy, and this is known as the no-slip condition. Since the layer of liquid molecules directly in contact with the surface is stationary, the surface temperature,  $T_{\text{surf}}$ , is the highest temperature in the temperature distribution. Therefore, microchannels that are too small could significantly negatively impact thermal performance as this boundary layer acts as a static thermal resistance.

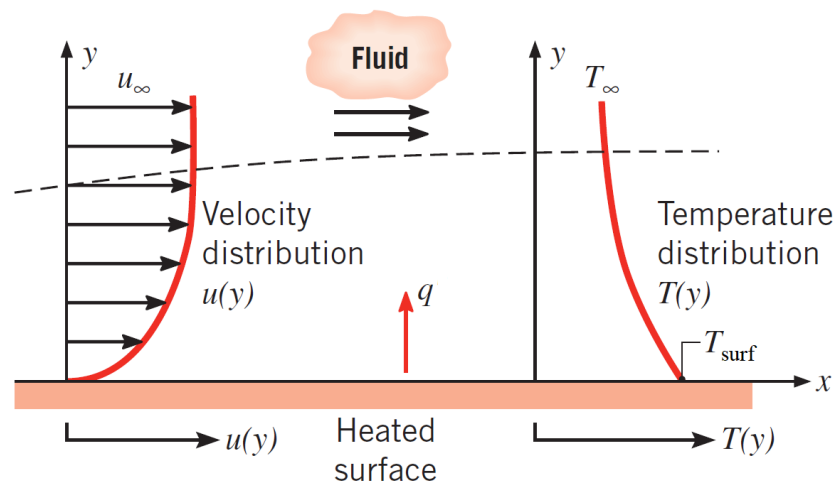


Figure 1.5: Boundary layer development of working fluid flowing along a heated surface. Taken from literature [26].

Computational fluid dynamics is typically used to design and validate microfluidics performance [27]. Platinum (Pt) resistance temperature detectors (RTDs) are often used to

probe the temperature of microdevices [28]. FDTR could potentially be a reliable way to experimentally inform the effective heat transfer coefficient of an embedded microchannel with steady fluid flow.

### 1.2.2 Thin film thermoelectrics

Similar to electronic devices such as CPUs, miniaturisation of optoelectronic and photonic devices also calls for higher thermal performance and tighter thermal controls solutions to handle high heat fluxes. The heat dissipation of these devices is typically handled by a macroscale thermoelectric cooler (TEC) as shown in Figure 1.6. It is worth noting that other heat dissipation methods such as forced air convection, and water-cooled convection can be used instead of natural air convection, or in conjunction with each other [29], [30]. Although macro TECs are relatively inefficient, with an efficiency of about 5 – 7% for most applications, TEC is an excellent option for systems that require temperature stability or/and sub-ambient conditions [31]. For efficient TEC operation the heat must be spread and dissipated on the side that the heat is pumped to.

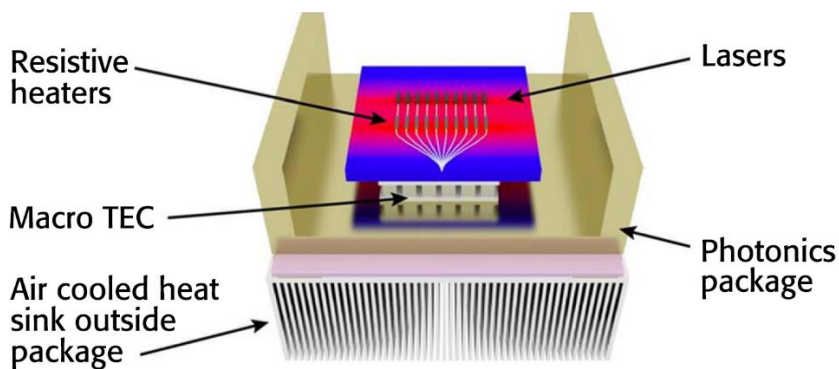


Figure 1.6: Schematic of a typical photonic device with last generation state-of-the-art thermal management solution. Taken from literature [32].

Figure 1.7 shows a typical thermoelectric module within a typical TEC. A temperature gradient is created when a DC electric current is applied. This is achieved by using two different semiconductor materials with different doping characteristics where one



material has higher electron energy changes for given thermal energy inputs. Generally, positively doped (p-type), and negatively doped (n-type) bismuth telluride ( $\text{Bi}_2\text{Te}_3$ ) are used as the thermoelectric elements, and ceramics are used for electrical isolation and rigidity of the overall TEC. When they are connected via an electrical interconnect (see Figure 1.7) and a voltage difference is applied to the ends, free electrons migrating to the p-type material with higher energy gaps result in smaller vibrations. This is possible when free electrons are migrating to a material with a higher minimum energy state, and without additionally provided energy, the energy level of electrons that successfully migrate would be capped by the highest energy level before migration, which unusually gives small vibrations at the p-n junction [33]. This means that the p-n junction is cold and can absorb heat, and this effect is known as the Peltier effect. However, this cooling effect is very small; therefore, several thermoelectric modules are connected electrically in series and thermally in parallel to form a typical TEC. The thermoelectric effect is well studied, and its theoretical background can be found elsewhere [34].

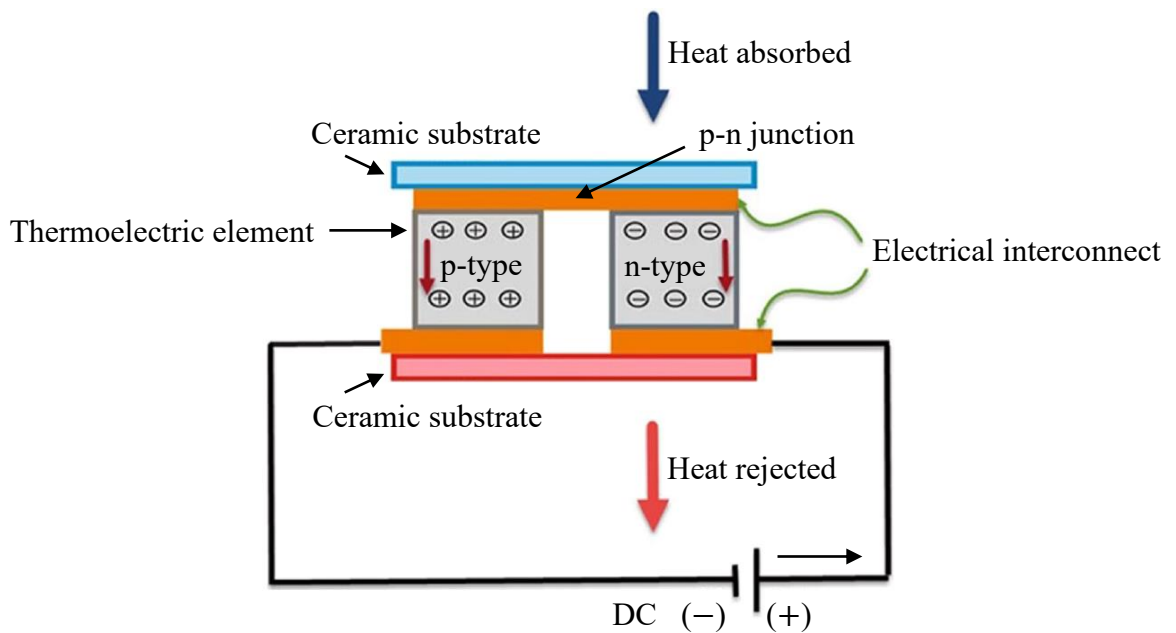


Figure 1.7: Schematic diagram of a single thermoelectric module. Adapted from literature [34].

Microscale TECs ( $\mu$ TECs) using thin film thermoelectrics have been proposed as a natural progression in handling higher heat flux. They are faster to respond than macroscale TECs. The response time scales with their critical dimension [35]. The ability for thin film thermoelectric materials to be fabricated using complementary metal oxide semiconductor compatible processes is ideal for targeting hot spots in state-of-the-art optoelectronic and photonic devices, which benefits from fast response time. Laird Technologies reported that thin film thermoelectric materials can handle much greater heat flux,  $q$ , than macroscale TECs, as shown in Figure 1.8 [36]. However, bulk thermoelectric materials can sustain a higher temperature difference,  $\Delta T$ . Therefore, a high heat dissipation solution is required on the hot side of thin film TECs, such as two-phase cooling.

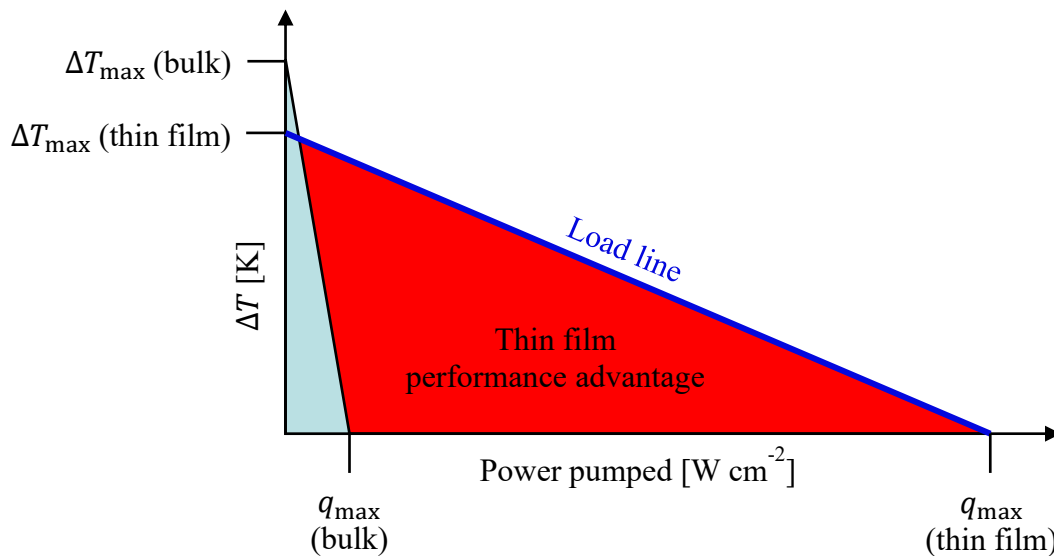


Figure 1.8: Bulk and thin film thermoelectric performance chart. Adapted from literature [36].

The performance characterisation is the same for thin film thermoelectrics as to bulk in principle by the thermoelectric figure of merit. Knowledge of electrical and thermal characteristics are required, however, accurately measurement of the thermal conductivity is significantly more difficult for thin films compared to bulk. This is because physical and thermal properties of thin films deviate from bulk, and the embedded nature of the

thermoelectric thin film layer in a  $\mu$ TEC device also makes it difficult to access for measurements. Still, the FDTR technique could potentially be a reliable way to experimentally study the thermal transport of embedded thin film thermoelectric materials.

### **1.2.3 Two-phase evaporators**

Passive and active two-phase cooling is commonly used to handle electronics with extremely high heat fluxes that exceed the capability in removing heat through the heat carrying capability of a working fluid without phase change [37]. Two-phase cooling typically removes twice as much heat compared to single-phase, and several times better than air cooling [38]. Figure 1.9 shows how a heat pipe uses passive two-phase cooling via latent heat of vaporisation to achieve an effective thermal conductivity higher than the bulk material thermal conductivity to carry heat away from a heat source. The effective thermal conductivity of a well-designed heat pipe can be as high as  $10 \text{ kW m}^{-1} \text{ K}^{-1}$  [37].

Active two-phase cooling in principle operates the same as the passive counterpart, but the vapor flow in the chamber is assisted by external pumping power to increase the flow rate. The low rate in a pumped two-phase cooler requires a less low rate, as it does not rely on the heat capacity of the working fluid to absorb the heat. This means that a lower pumping power consumption, and reduced erosion, compared to single-phase cooling.

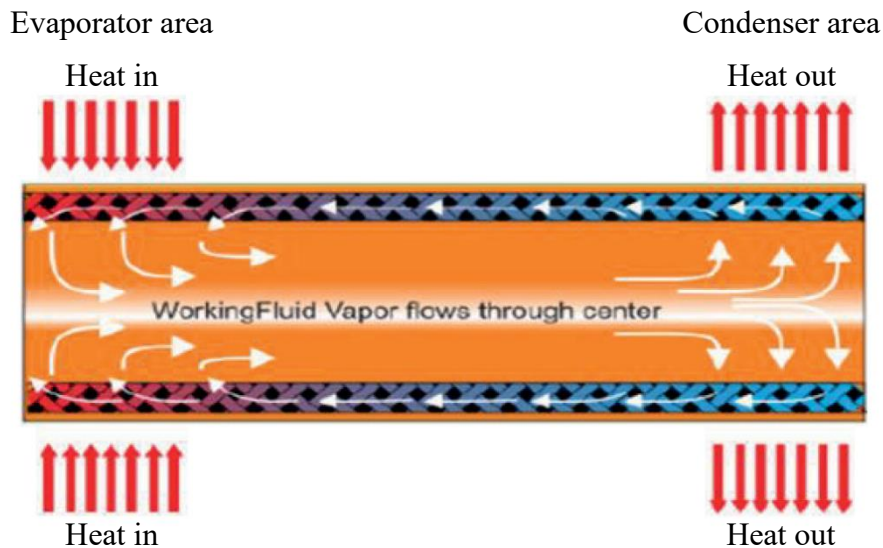


Figure 1.9: Illustration of a cross-sectional view of a typical heat pipe. Working fluid evaporates on the hot side, then the vapor travels to the cold side and condenses onto the cold surfaces. After the condensation process, working fluid are circulated back to the hot side via capillary action. Taken from literature [37].

Several designs and studies of two-phase cooling with microchannels are well documented in literature review [38]. One of the more interesting approaches is the nanoporous membrane two-phase microscale evaporator design (see Figure 1.10) as it has the potential to be fully integrated into an optoelectronic or photonic package [39] in conjunction with  $\mu$ TECs. More recently, the nanoporous evaporator design has been demonstrated removing heat fluxes of  $665 \pm 74 \text{ W cm}^{-2}$  using pentane [10], and has since been further investigated with lower surface tension liquids that can achieve several times higher evaporation efficacy [40]. Details of the evaporation figure of merit which is defined by the evaporation efficacy can be found elsewhere [41].

In terms of thermal performance characterisation, RTDs and traditional temperature probes are typically used to determine the local temperature inside the device and device surface temperature, respectively. Contact temperature measurements result in thermal bridging which can significantly disturb the local temperature distribution in these microscale devices. FDTR remains as one of the only non-contact experimental techniques

that could potential measure all the thermal properties of a nanoporous membrane microscale evaporator.

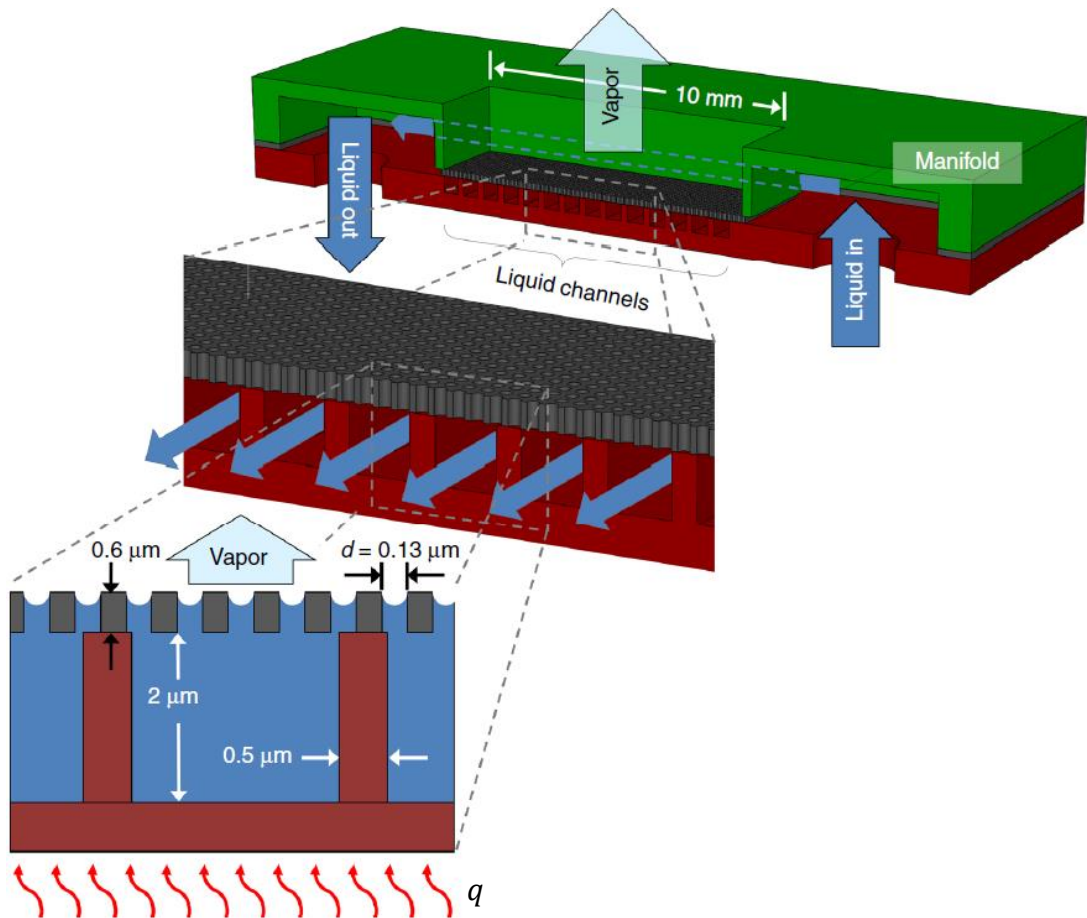


Figure 1.10: Schematic of a nanoporous membrane two-phase microscale evaporator design. Taken from literature [10].

### 1.3 Thesis outline

**Chapter 2** introduces the reader to the concepts and terminologies of heat transport relevant to this thesis. One portion provides basic details of phonons, phonon dispersion relations, and phonon density of states, along with approximation for the phonon density of states. The other portion provides an understanding of two prominent analytical models in understanding and predicting how phonons transport heat across solid-solid interfaces.

**Chapter 3** introduces all the key characterisation methods used in this thesis. Scanning electron microscopy, and atomic force microscopy are presented as methods to capture cross section and plan topographic details of samples, respectively. The four-point probe method is presented to measure top contact electrical conductivity, attain contact thermal conductivity and electrical contact resistance. Contact angle goniometry is presented to determine the wettability of a sample surface. It is then followed by a detailed description of the frequency-domain thermoreflectance (FDTR) technique. This includes details of the theory, instrumentation, optics, procedures, and basic mathematical derivation of the equations necessary to solve the heat diffusion equation and interpret measured FDTR data. Finally, details of FDTR sensitivity and uncertainty analysis are presented.

**Chapter 4** provides a study of an electrodeposited bismuth telluride thin film thermoelectric device. The impact of thermal properties on thermoelectric performance is investigated on this  $\mu$ TEC test device. Experimental methods described in Chapter 3 are used to experimentally characterise the thermal properties of this test device which is used to determine the overall thermoelectric performance. The size effect is also investigated using kinetic theory with measured values. Finally, we used a basic analytical model to better understand how operation temperatures would impact interfacial heat transport in the test device.

**Chapter 5** introduces the concept and use of self-assembled monolayers (SAMs) to manipulate surface wettability. This chapter also introduces a bidirectional heat transfer model which is then used to analyse the FDTR data of solid-liquid systems with SAMs studied in this work. A modified analytical model is also introduced to better understand and predict phonon transport across solid-liquid interfaces. The relationship between thermal boundary conductance across solid-liquid interface and surface wettability is investigated

using deionised water and ethanol, as they are commonly used in single-phase and two-phase cooling, respectively.

**Chapter 6** will show a study of the effect on effective thermal boundary transport across Au-H<sub>2</sub>O with a known physisorbed species on an Au surface. The effect of a controlled physisorption process on interfacial thermal transport will be quantified using the FDTR technique. Additionally, I have developed an analytical model to predict the effective thermal boundary conductance to better understand phonon transmission probabilities in solid-liquid systems with a van der Waals type bonding interlayer.

**Chapter 7** concludes the work presented in this thesis and provides a summary of the result chapters and outlook for future experiments.

## Chapter 2.

# Theories and concepts of heat transport

## 2.1 Introduction

In this chapter, the fundamentals of thermal transport physics will be briefly reviewed to form the basis required for subsequent chapters. Since the focus of this thesis mainly concerns systems that are partially liquid, we will omit the theory of thermal conductivity as the general theory of energy and heat capacity of liquids is still incomplete [42]. This is the case as both the viscosity and thermal conductivity of a liquid cannot yet be reliably evaluated from first principles [43]. For introductory purposes, the fundamental theories will be presented for solids. In later chapters, we will introduce modifications of these theories for liquids, which inform the thermal conductivity and heat capacity of bulk and thin films for both solids and liquids experimentally.

## 2.2 Heat carriers

Thermal energy can be propagated in solids as heat by electrical carriers, lattice waves, electromagnetic waves, spin waves, or other excitations [44]. In metals, electrical carriers such as electrons carry the majority of the heat, while the heat is predominantly carried by lattice waves such as phonons in semiconductors and dielectrics. In this thesis, we focus the attention to lattice vibrations as the dominant heat transport mechanism in the systems we are interested in.

Figure 2.1(a) shows a simple monatomic chain of a simple ball-spring representation of a one-dimensional (1D) crystal with lattice constant,  $a$ , and  $N$ -atoms vibrating and



propagating a lattice wave. If  $N \rightarrow \infty$ , a lattice wave can be expressed as a combination of plane waves in the form of:

$$\psi(x, t) = Ae^{i(kx - \omega t)}, \quad (2.1)$$

where  $A$  is the wave amplitude,  $x = Na$  and is the position coordinate,  $t$  is time;  $k = 2\pi/\lambda$  and is the angular wavenumber or magnitude of the wavevector, where  $\lambda$  is the wavelength;  $\omega = 2\pi f$  and is the angular frequency, where  $f$  is the ordinary frequency. It is worth noting that several wavevectors are possible if the number of total atoms,  $N_{\text{tot}}$ , is large. A visualization of a simple plane wave is plotted using Eq. (2.1) with constant  $t$  and  $A = 1$  in Figure 2.1(b). A superposition of different plane waves creates a wave packet, or a wave group as shown in Figure 2.1(c). The vibrational energy that arises from a wave packet is treated as a propagating particle, or a “phonon.” Phonons can also be described as a gas of particles (see Figure 2.1(d)).

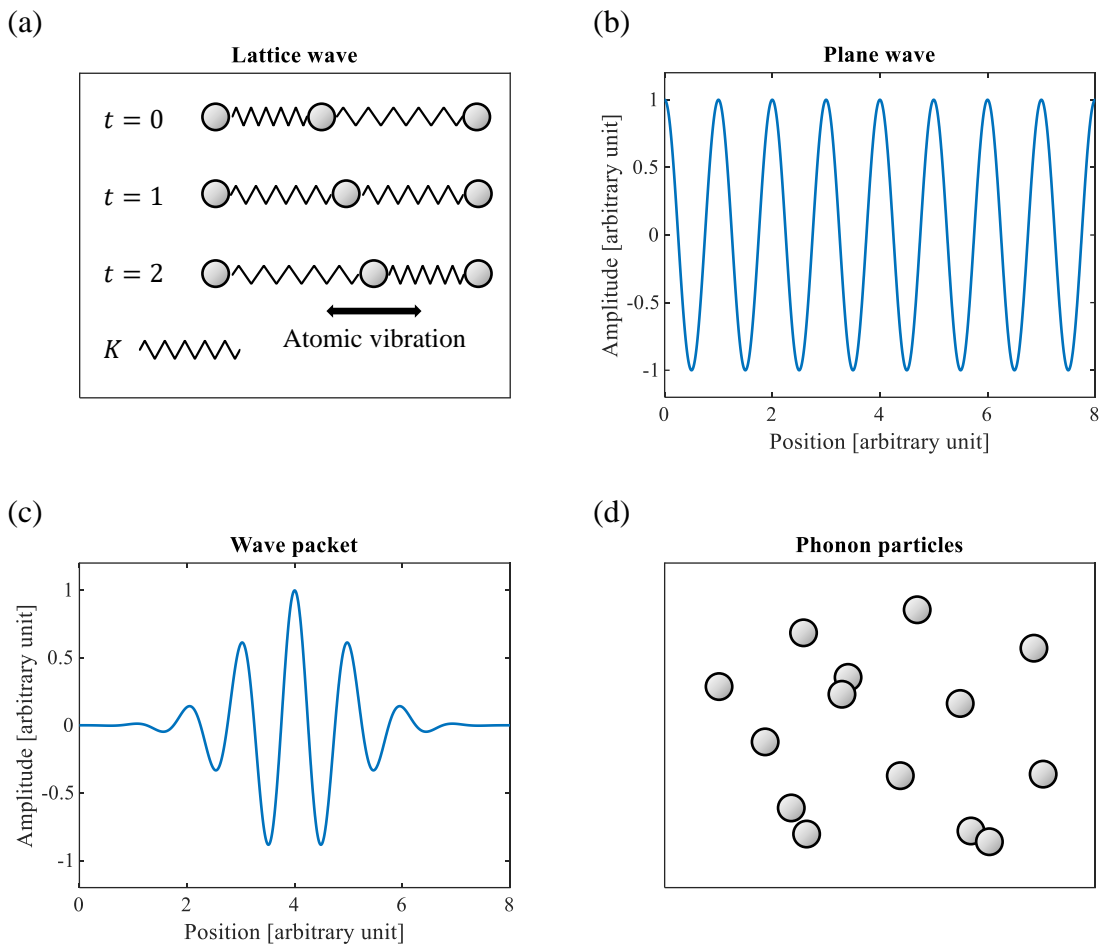


Figure 2.1: (a) A simple schematic of an oscillatory motion of atoms along a short monatomic lattice with spring constant,  $K$ , for a longitudinal acoustic wave. (b) A truncated plane wave using Eq. (2.1). (c) A representation of a wave group. (d) A representation of a gas of phonon particles.

### 2.2.1 Phonons, phonon dispersion relations, and phonon density of states

Phonons are not actually physical particles, but a phonon can be treated as a particle or a wave depending on the characteristic length of the phonon wave packet relative to the crystal lattice. Phonons are better treated as particles when they are significantly smaller than the crystal. The size of a phonon is typically within  $1 - 10 \text{ \AA}$  [45]. However, the particle model fails when the characteristic length of the crystal lattice is close to the phonon particle size, and then it is then more appropriate to consider a phonon to exhibit wave-like behaviour

[46]. Nevertheless, the spectral behaviour, absorption, scattering characteristics (elastic or inelastic) can be explained with the particle concept [47].

A phonon is a quasi-particle or a quantum of crystal vibrational energy, and is quantum mechanically described for studying thermal energy transport. Therefore, a phonon has discrete levels of energy,  $E = \hbar\omega$ , and momentum,  $p = \hbar k$ , where  $\hbar = h/2\pi$  and is the reduced Planck constant, and  $k$  is the phonon wavevector if we define the wavelength as  $\lambda_i = N_{\text{tot}}a/i$ , where  $i$  is an indexing integer. It may be worth noting that a phonon wavelength is limited by the lattice constant, such that  $2a \leq \lambda < \infty$ . The theoretical lattice chain is unable to take  $2a \leq \lambda$  as there will not be enough lattice points to sustain such wavelengths. This means that the maximum unique wavevector is  $|k_{\text{max,unique}}| = \frac{\pi}{a}$ .

The dispersion relation, which connects the phonon frequency and its wavevector, contains information regarding material characteristics, from elastic constants to crude approximations for the scattering rates of phonons [48]. Solving the equation of motion derived from the monatomic chain of atoms with finite mass,  $m$ , presented in Figure 2.1(a), yields:

$$\omega(k) = 2 \sqrt{\frac{K}{m}} \left| \sin\left(\frac{ka}{2}\right) \right|. \quad (2.2)$$

The systems of equations can also be solved for a diatomic chain with two different masses,  $m_1$  and  $m_2$ , where  $m_2 = 2m_1$ , in an alternating configuration, and is well documented in [48], which results in the form of:

$$\omega(k)^2 = K \left( \frac{1}{m_1} + \frac{1}{m_2} \right) \pm K \sqrt{\left( \frac{1}{m_1} + \frac{1}{m_2} \right)^2 - \frac{4}{m_1 m_2} \sin^2 \left( \frac{ka}{2} \right)}. \quad (2.3)$$

Figure 2.2(a) and Figure 2.2(b) shows a normalized dispersion relation plot using Eq. (2.2) and Eq. (2.3), respectively. Since the solutions for Eq. (2.2) and Eq. (2.3) are periodic, we can present the dispersion curves within a uniquely defined primitive cell without loss of information. The uniquely defined primitive cell mentioned is in reciprocal space, and is known as the first Brillouin zone. We refer, for the concepts of reciprocal space and Brillouin zones, to textbooks as they are extensively covered in solid-state physics courses [49]. From Figure 2.2(b), we can see that there exist two dispersion curves for the diatomic chain example. The lower branch and upper branch correspond to the minus and plus sign solution of Eq. (2.3), respectively, and they are known as the acoustic branch and optical branch, respectively. Two important quantities we can obtain from the dispersion relation are phase velocity,  $v_p$ , and group velocity,  $v_g$ :

$$v_p = \frac{\omega}{k}, \quad (2.4)$$

$$v_g = \frac{\partial \omega}{\partial k}. \quad (2.5)$$

While the phase velocity tracks the speed of each individual wave of a wave packet, the group velocity refers to the speed of the resultant wave packet. So, knowledge of the system specific group velocity is especially important as it determines the rate of energy transport. For long-wave limit ( $k \rightarrow 0$ ), the slope is steeper, which means faster energy transport. Notice that the optical branch is relatively flat compared to the acoustic branch. This quality is generally true, also  $v_g \rightarrow 0$  as  $k \rightarrow 0$  in the optical branch, which indicates that the group

velocity from the optical branch is relatively small. In many cases, the optical phonons are often omitted in calculations for phonon energy transport.

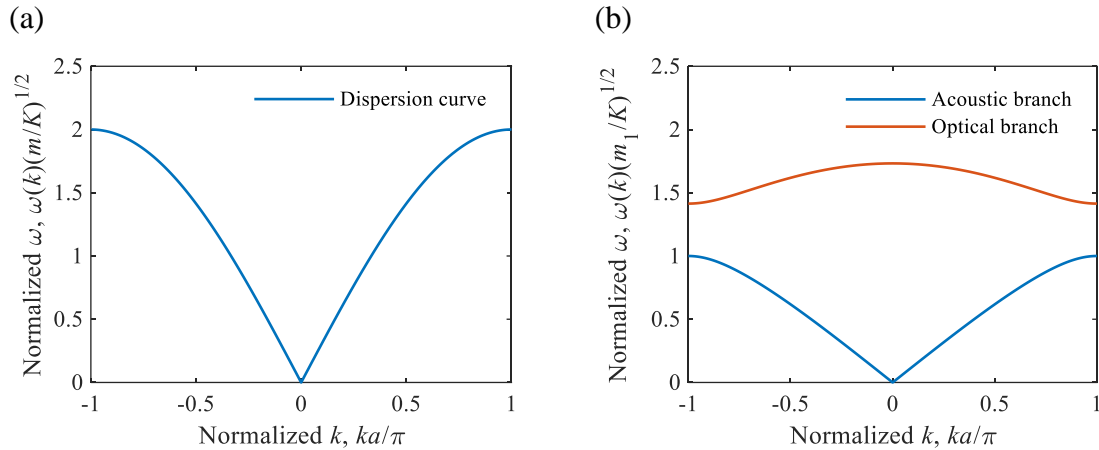


Figure 2.2: Dispersion relation for spring-mass array of: (a) a monatomic chain; (b) a diatomic chain.

Expanding on the 1D system, a three-dimensional (3D) material such as bulk Au possess two additional phonon branches, resulting in three polarizations: one longitudinal acoustic (LA) and two transverse acoustic (TA) branches. Some materials possess several optical branches,  $(3N_{uc} - 3)$  optical branches, where  $N_{uc}$  is the number of atoms in a unit cell. Au has a face-centred cubic (FCC) structure, one of the most common crystal structures. Figure 2.3 (a) shows the first Brillouin zone of an FCC in three-dimensional  $\mathbf{k}$ -space. The phonon dispersion curves for Au in the direction of high symmetry points are shown in Figure 2.3(b). The phonon density of states (DOS) shown in Figure 2.3(b) contains information of how much energy can be transferred at a given phonon frequency and the frequency range that can exist in a given crystal.

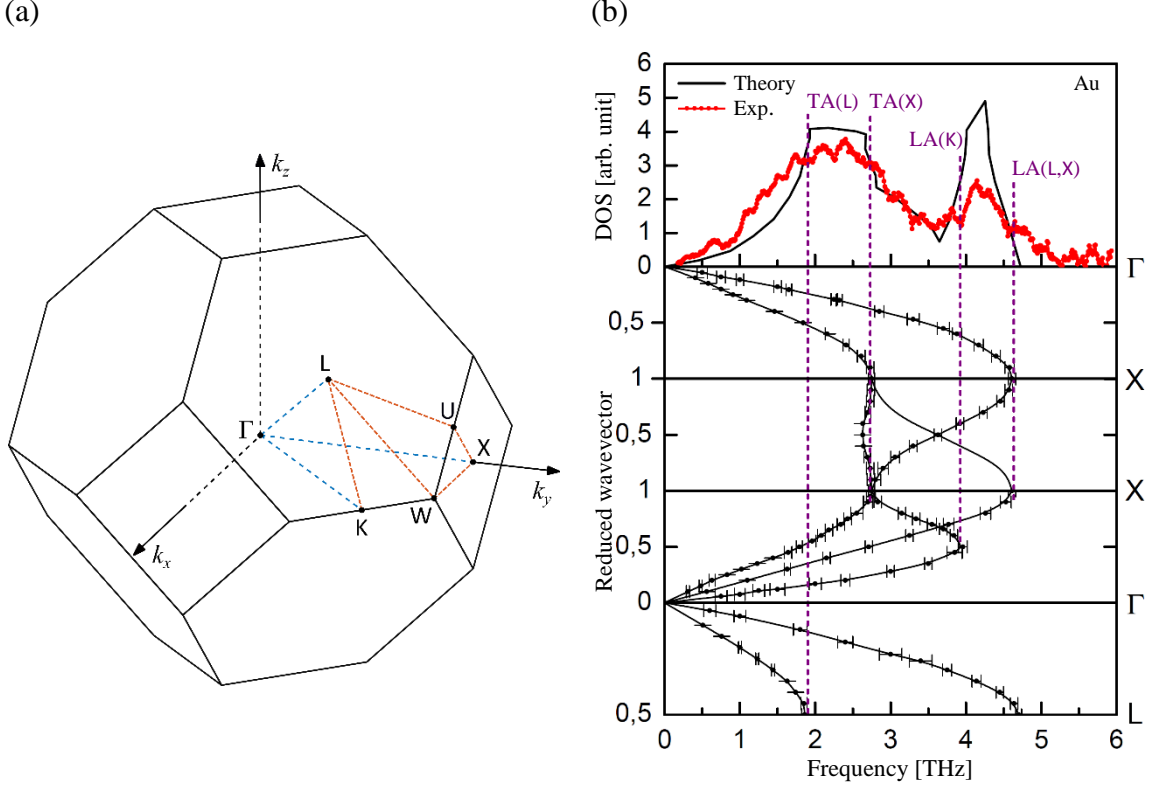


Figure 2.3: (a) First Brillouin zone and high symmetry points for FCC structure. (b) Phonon dispersion curves for bulk Au along with the associated phonon DOS, where the plot is taken from literature [50]. The theoretical estimations of the phonon DOS were calculated using a fourth-neighbour general force constants model [51] and the experimental data were measured using the plasmon resonant Raman scattering method [50].

Phonon DOS,  $\mathcal{D}$ , is defined as the number of modes per unit wavevector per unit volume of real space; a 3D DOS can be expressed as:

$$\mathcal{D}_{3D}(\mathbf{k}) = \frac{1}{a^3} \frac{d\mathcal{N}_{3D}}{d\mathbf{k}} = \frac{\mathbf{k}^2}{2\pi^2}. \quad (2.6)$$

Here,  $\mathcal{N}_{3D}$  is the 3D number of states, which is calculated by forming the ratio of a spherical  $\mathbf{k}$ -space volume to that of an individual state. Considering the temperature range of the systems studied in this work, we assume that  $\mathbf{k}$  is relatively small and is in a linear regime around  $\Gamma$  therefore we use an approximation of  $\mathcal{N}_{3D}$  given by:

$$\mathcal{N}_{3D}(\mathbf{k}) = \frac{4\pi\mathbf{k}^3/3}{(2\pi/a)^3}, \quad (2.7)$$

where  $d\mathbf{k} = dk_x dk_y dk_z$ ,  $a = N_{\text{tot}}a$ , and  $2\pi/a$  is the separation distance of each allowable state in  $\mathbf{k}$ -space [48]. The phonon DOS is also commonly used with respect to frequency. The transformation from  $\mathbf{k}$ -space to frequency space can be achieved by using the chain rule and the definition of group velocity:

$$\mathcal{D}_{3D}(\omega) = \frac{1}{a^3} \frac{d\mathcal{N}_{3D}}{d\omega} = \frac{1}{a^3} \frac{d\mathcal{N}_{3D}}{d\mathbf{k}} \frac{d\mathbf{k}}{d\omega} = \frac{\mathbf{k}(\omega)^2}{2\pi^2 v_g(\omega)}. \quad (2.8)$$

Obtaining and implementing an accurate phonon dispersion for thermal transport calculations is often possible but can be complicated. Phonon dispersion is often simplified through the Debye approximation for calculating phonon transport across interfaces. Such simplification assumes a linear dispersion  $\omega = v_{g,\text{ave}}\mathbf{k}$  with upper frequency limit  $\omega_{\text{max,D}}$  which matches the total number of possible phonon states. The Debye approximation of the phonon DOS is given by:

$$\mathcal{D}_{3D,D}(\omega) = \begin{cases} \frac{\omega^2}{2\pi^2 v_{g,\text{ave}}^3}, & \omega < \omega_{\text{max,D}}, \\ 0, & \omega \geq \omega_{\text{max,D}} \end{cases}, \quad (2.9)$$

with:

$$\omega_{\text{max,D}} = v_{g,\text{ave}}(6\pi^2 \rho_N)^{1/3}, \quad (2.10)$$

where  $v_{g,\text{ave}}$  is the average group velocity of the acoustic branches, and  $\rho_N$  is the number density. Figure 2.4(a) shows a comparison between the Debye approximation of the phonon dispersion of a monatomic chain and the phonon dispersion calculated by solving Eq. (2.2) mentioned in Section 2.2.1. The Debye approximation is generally sufficient for when  $\mathbf{k}$  is

not very large but it gets progressively worse in representing the real acoustic phonon dispersions when approaching the boundary of the Brillouin zone. For more recent use of the Debye approximation in interfacial transport calculations, the phonon DOS is decomposed to its respective polarizations:

$$\mathcal{D}_j(\omega) = \begin{cases} \frac{\omega^2}{2\pi^2 v_j^3}, & \omega < \omega_{\max,j}, \\ 0, & \omega \geq \omega_{\max,j} \end{cases}, \quad (2.11)$$

with:

$$\omega_{\max,j} = v_j (6\pi^2 \rho_N)^{1/3}, \quad (2.12)$$

where  $v$  is the acoustic velocity, and subscript  $j$  refers to the acoustic polarisation (i.e., longitudinal, L, or transverse, T). Figure 2.4(b) shows longitudinal and transverse DOS using Eq. (2.11), and DOS obtained from theory and experiment [50], [51].

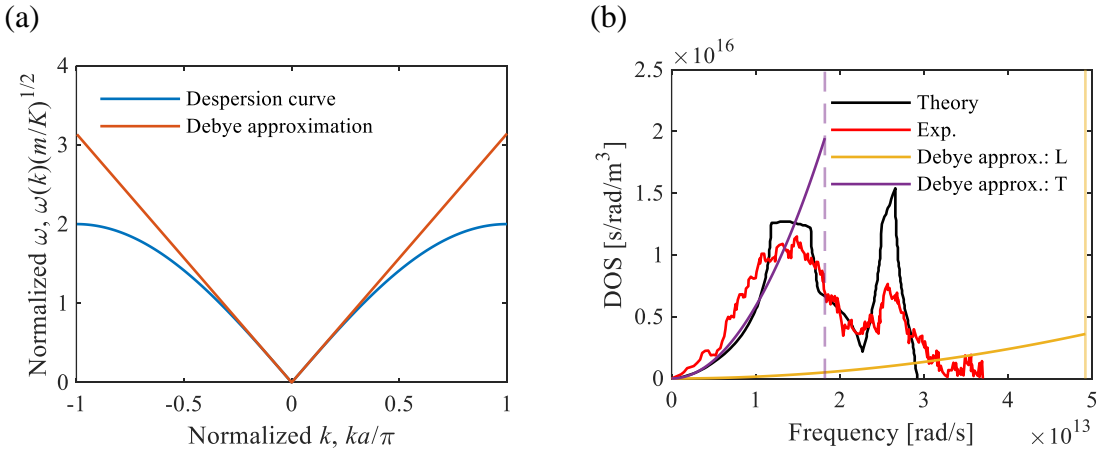


Figure 2.4: (a) A comparison between dispersion relation for a monatomic chain with and without Debye approximation (b) A comparison between the phonon DOS of Au from theory, experiment, and Debye approximation, where the results from theory and experiment are taken from literature [50], [51]. The dash and solid vertical lines represent the transverse and longitudinal cutoff frequency, respectively.



## 2.3 Interfacial heat transport

As feature size continues to miniaturize in the foreseeable semiconductor technology roadmaps for (opto)electronics devices, the resulting smaller form factor with higher power density leads to increased heat dissipation issues, which limits device performance and longevity. However, interfacial effects are typically ignored when dealing with devices at the macroscale, as the ratio of volume to surface area is relatively large. However, as characteristic lengths approach to microns and nanoscales, the ratio of surface area to volume to surface area shrinks and interfacial thermal transport becomes a concerning factor. So, understanding of thermal transport across interfaces of dissimilar materials has become an integral part of device designing process. Interfacial heat transport is commonly characterized by the TBC,  $G$ , or thermal boundary resistance (TBR), where TBR is the reciprocal of TBC. The first intensive work on TBC was reported by Peter Kapitza in 1941 [52]. Kapitza observed a temperature difference,  $\Delta T$ , on a contact surface when some heat flux,  $q$ , passes through the interface from a solid into He II. The quantity  $G$  is related to  $q$  and  $\Delta T$  by [53]

$$q = G\Delta T. \quad (2.13)$$

The work of Kapitza has piqued many researchers in developing mathematical models and experimental techniques to predict and measure TBC between dissimilar materials, respectively [14], [54].

A mathematical representation of flux across an interface is used to form the fundamental framework of any predictive model that is concerned with interfacial transport. Following [55], we consider some flux,  $q_b$ , travelling across interface from side 1 to side 2,

the composition of the flux,  $b = b_j(k_x, k_y, k_z)$ , can be mass, charge, energy, or momentum.

The flux along the  $z$  direction across side 1 to side 2 can be mathematically represented as:

$$q_b = \frac{1}{(2\pi)^3} \sum_j \int_0^{\pi/2} \int_0^{2\pi} \int_{k_{1,x}} \int_{k_{1,y}} \int_{k_{1,z}>0} b v_{1,j} \mathcal{T} f_1^0 \cos \theta \sin \theta dk_{1,z} dk_{1,y} dk_{1,x} d\theta d\varphi, \quad (2.14)$$

where  $f^0$  is the equilibrium carrier distribution function,  $\theta$  and  $\varphi$  are the incident azimuth and elevation angles approaching the interface from side 1, respectively, and  $\mathcal{T}$  is the phonon transmission probability. Using the Landauer formalism, the heat flux across interface from material of side 1 ( $i = 1$ ) to material of side 2 ( $i = 2$ ) can be expressed in frequency space as:

$$q = \frac{1}{2} \sum_j \int_0^{\omega_{\max,1,j}} \int_0^{\theta_{c,1,j}} \mathcal{T} v_{1,j}(\omega) \mathcal{D}_{1,j}(\omega) \hbar \omega f_{\text{BE}}^0(\omega, T) \cos \theta \sin \theta d\theta d\omega, \quad (2.15)$$

where  $\omega_{\max}$  is the cut-off frequency,  $\theta_c$  is the critical angle,  $f_{\text{BE}}^0(\omega, T) = 1/(e^{\hbar\omega/k_{\text{B}}T} - 1)$  is the Bose-Einstein equilibrium phonon distribution,  $k_{\text{B}}$  is the Boltzmann constant, and  $T$  is the local temperature. Rewriting Eq. (2.13) and substituting Eq. (2.15) into (2.13) yields:

$$G = \frac{1}{2} \sum_j \int_0^{\omega_{\max,1,j}} \int_0^{\theta_{c,1,j}} \mathcal{T} \mathcal{M}(\omega) c(\omega) \cos \theta \sin \theta d\theta d\omega, \quad (2.16)$$

with:

$$\mathcal{M}(\omega) = v_{1,j}(\omega) \mathcal{D}_{1,j}(\omega), \quad (2.17)$$

$$c(\omega) = \hbar \omega \frac{\partial f_{\text{BE}}^0(\omega, T)}{\partial T}, \quad (2.18)$$

where  $\mathcal{M}(\omega)$  and  $c(\omega)$  are the frequency dependent number of allowable phonon modes and heat capacity, respectively. The transmission probability is arguably the most difficult term to accurately determine, as any fundamental assumption invoked will have substantial implications on the formation of  $\mathcal{T}$  and thus the overall predictability of  $G$ . We will discuss two key fundamental assumptions which leads to their respective model in Section 2.3.1 and 2.3.2. The two models ultimately form the frameworks of many recent analytical models that better predict interfacial heat transport under selective configurations and conditions, as we now go on to detail of the two models in the following two sections.

### 2.3.1 Acoustic mismatch model (AMM)

Motivated by Kapitza's work, Little's investigation in acoustic mismatch theory led to the publication of the acoustic mismatch model (AMM) in 1959 [56]. The main assumption in AMM is that the interface is perfectly flat, therefore the model considers purely specular scattering of phonons at the interface. This model is typically used alongside with Debye approximation such that linear phonon dispersion is assumed for simplicity. The model calculates the TBC based on the ratio of acoustic impedances of material 1 and material 2 by solving the continuum elasticity equations for the acoustic transmission and reflection between the two materials. The phonon transmission probability across the interface from material 1 to material 2 with incident angle  $\theta_1$  in medium 1 is expressed as:

$$\mathcal{T}_j(\theta) = \frac{4 \frac{\rho_2 v_{2,j} \cos \theta_2}{\rho_1 v_{1,j} \cos \theta_1}}{\left( \frac{\rho_2 v_{2,j}}{\rho_1 v_{1,j}} + \frac{\cos \theta_2}{\cos \theta_1} \right)^2}, \quad (2.19)$$

where  $\rho$  is the density, and  $\theta_2$  is the transmitted angle and is related to the incident angle through and equivalent of Snell's law,  $\sin \theta_1 / v_1 = \sin \theta_2 / v_2$ , with critical angle  $\theta_{c,1} =$

$\sin^{-1}(v_1/v_2)$  assuming  $v_2 > v_1$ . The transmission probability can be rewritten and is typically used in the form of:

$$\mathcal{T}_j(\theta) = \frac{4Z_{1,j}Z_{2,j} \cos \theta_1 \cos \theta_2}{(Z_{1,j} \cos \theta_1 + Z_{2,j} \cos \theta_2)^2}, \quad (2.20)$$

where  $Z_{i,j} = \rho_i v_{i,j}$  and is the acoustic impedance for material  $i$  with polarisation  $j$ . The model Little proposed has proven successful at predicting  $G$  for  $T < 30$  K [14]. Although thermal roughness cannot be eliminated, predictions can be relevant for certain systems with extremely flat interfaces which minimizes the number of shorter wavelengths experiencing roughness at the interface. The prominent extensions to the AMM include the effect of phonon scattering in the medium near the interface [57], varying weak interfacial bond strength at the interface [58] and when an interface is under static pressure [59]. Unfortunately, when the Debye approximation is applied, these modifications still result in predicting TBC below experimental results at room temperature [60], [61]. In Chapter 5, we will show how AMM can be adjusted to make predictions closer to experimental results.

### 2.3.2 Diffuse mismatch model (DMM)

In 1989, Swartz and Pohl [29] published work on the diffuse mismatch model (DMM) in attempt to better predict TBC with higher system temperatures and roughness at the interfaces. The model assumes complete diffuse and elastic scattering. The completely diffused assumption means that phonons are assumed to scatter evenly in all direction, so integrating over all angles yields  $1/2$ , and Eq. (2.16) is then reduced to:

$$G = \frac{1}{4} \sum_j \int_0^{\omega_{\max,1,j}} \mathcal{T}\mathcal{M}(\omega) c(\omega) d\omega. \quad (2.21)$$

In DMM, phonons are assumed to lose the memory of their direction and polarisation, but not their frequency. The transmission probability with a completely elastic treatment is derived by on the assumption of detailed balance. This transmission probability is polarization-independent, wavevector-dependent, and is given by

$$\mathcal{T}(\omega) = \frac{\sum_j \int_0^{\omega_{\max,2,j}} \mathcal{M}_{2,j}(\omega) \hbar \omega f_{\text{BE}}^0(\omega, T) d\omega}{\sum_j \int_0^{\omega_{\max,1,j}} \mathcal{M}_{1,j}(\omega) \hbar \omega f_{\text{BE}}^0(\omega, T) d\omega + \sum_j \int_0^{\omega_{\max,2,j}} \mathcal{M}_{2,j}(\omega) \hbar \omega f_{\text{BE}}^0(\omega, T) d\omega}. \quad (2.22)$$

For interfaces between isotropic materials, the Debye approximation is often assumed for simplicity. Evaluating the integrals in Eq. (2.22) with the assumption of a linear relationship between their respective group velocity and wavevector reduces the expression into a more familiar form:

$$\mathcal{T}(\omega) = \frac{\sum_j \mathcal{M}_{2,j}(\omega)}{\sum_j \mathcal{M}_{1,j}(\omega) + \sum_j \mathcal{M}_{2,j}(\omega)}. \quad (2.23)$$

Similar to the AMM, when the Debye approximation is applied, the DMM often predicting TBC below experimental results [61], [62]. However, many extensions have been developed to account for full phonon dispersions [63], disordered interfaces [64], surface roughness [65], and inelastic scattering [55]. Although these modifications helped the DMM to predict results with better agreement to experimental data, a more fundamental approach in understanding phonon transport across solid-solid interfaces though first-principles using mode-resolved atomistic Green's function simulation showed that a single disordered interface cannot make a phonon lose its memory, making DMM inherently limited in predicting TBC [66].

## **2.4 Summary**

In this chapter, we described the basic theories and concepts of heat transport relevant to this thesis. Phonons, phonon dispersion relations, and phonon density of states were introduced, along with the Debye model for the phonon density of states. Two prominent analytical models in predicting thermal boundary conductance across solid-solid interfaces were discussed. In Chapter 3, we will describe the experimental technique used to inform us about thermal properties such as thermal conductivity, volumetric heat capacity, and thermal boundary conductance. In Chapter 5, we will describe how the two prominent analytical models can be used to predict the thermal boundary conductance across solid-liquid interfaces.

# **Chapter 3.**

## **Characterisation methods**

### **3.1 Introduction**

In this chapter, some of the key characterisation techniques to understand mechanical, electronic, and thermal properties of thin films and interfaces will be reviewed. While most of the systems mentioned in this chapter are commercially available, the frequency-domain thermoreflectance (FDTR) system which is described in detail in this chapter was custom built explicitly for this project.

### **3.2 Scanning electron microscopy (SEM)**

Scanning electron microscopy (SEM) is a microscopy technique to analyse surfaces and is used to produce surface images with magnification multiple orders greater than that of traditional optical microscopy [67]. The idea of SEM was inspired by the development of the electron microscope by Ernst Ruska and Max Knoll in 1931 [68]. Figure 3.1 shows a schematic with the key components of a typical SEM. An electron beam is formed by the positively charged anode plate, and the electron beam size is controlled by the condenser lenses. The scanning coils' function is to deflect the electron beam to raster scan the surface of a given sample. The surface topography and composition information can be obtained by analysing electrons and X-ray photons ejected from the sample due to the electron beam.

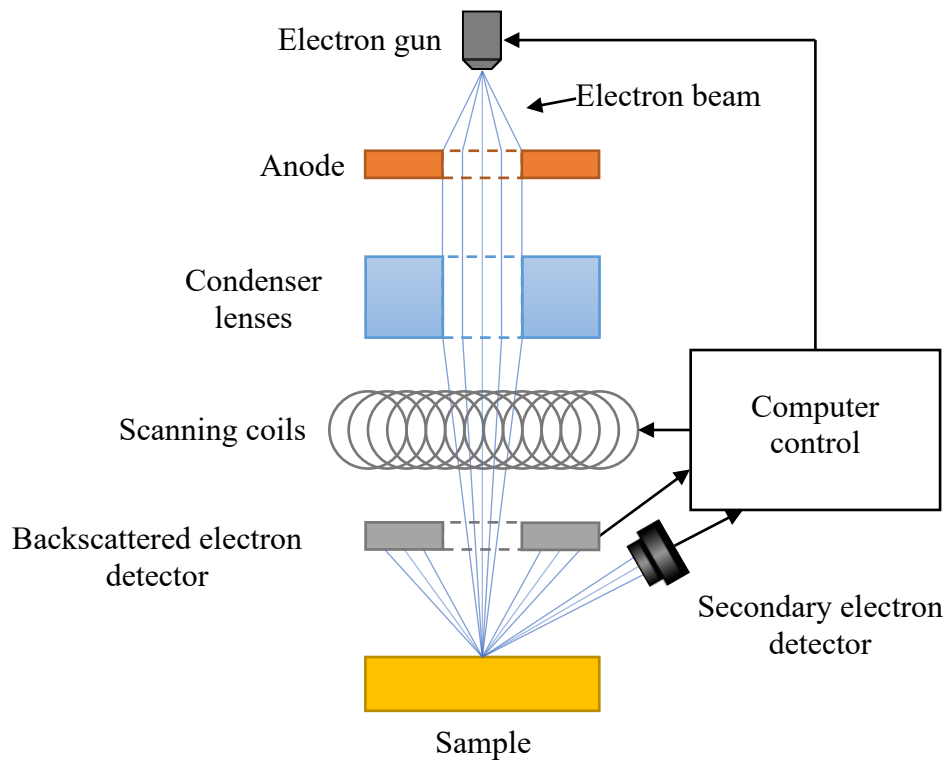


Figure 3.1: A schematic of a scanning electron microscope.

### 3.2.1 Emitted X-ray photons and ejected electrons

Figure 3.2 shows where X-ray photons emitted, and different types of electrons ejected in a sample when electron beam strikes a sample surface. The corresponding processes give information about the sample at different depths [69]. Emitted X-ray photons cover the entire electron-matter interaction volume and gives information about the energy spectrum and chemical composition of materials. Ejected backscattered electrons originate from elastic collisions during electron-matter interaction process from depths of 100 nm – 1  $\mu$ m, and are sensitive to the atomic number of the ejecting material, which gives information about the composition of materials [70]. Ejected secondary electrons originate from inelastic collisions during electron-matter interaction process from depths of few nanometres to 100 nm and give information about the topography of the surface of the material [71]. Ejected Auger electrons are from the top atomic layers and can also give information about the



topography of the surface of the material but it has very limited analysis depth of a few nanometres at maximum [69].

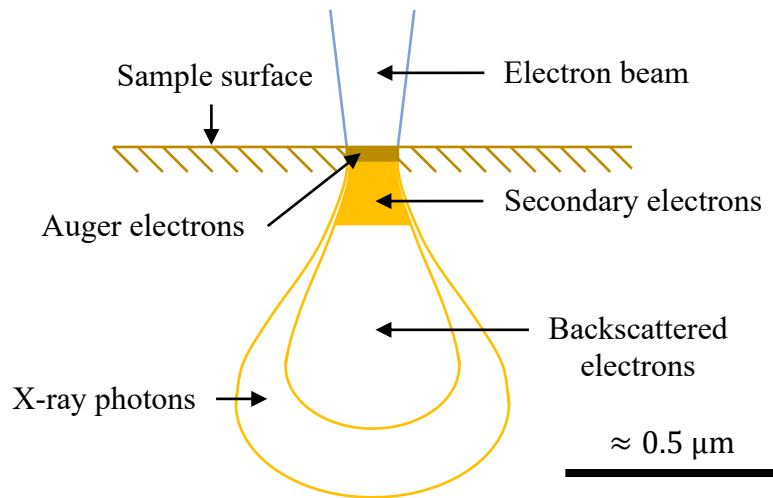


Figure 3.2: A simple schematic illustration of electron-matter interaction volume when an electron beam strikes a sample surface. Adapted from literature [69].

In this thesis, we used a Carl Zeiss AG SUPRA 40 field emission SEM (FESEM) to obtain cross sectional details of the samples. The only major difference between SEM and FESEM is the electron generation system. A field emission gun is generally preferred as it can provide better focused electron beams, and thus higher spatial resolution. All SEM images in this thesis were produced using the secondary electron detector of the FESEM with an electron beam voltage at  $\sim 10$  kV and varying magnification combinations.

### 3.3 Atomic force microscopy (AFM)

In 1986, Gerd Binnig, Calvin Quate, and Christopher Gerber developed the atomic force microscope (AFM) [72]. An AFM has the capabilities of performing force measurement, topographic imaging, and manipulation on conductive and non-conductive surfaces beyond the diffraction limit with nanoscale resolution [73]. Several improvements have been made to the AFM technique since the first modification of the technique to image in liquid [74] to more recent modification of the technique to perform high-speed AFM [75].

### 3.3.1 Operation modes

AFM operates under three typical modes, where the mode type, working principle, advantages and disadvantages are contained in Table 3.1. Figure 3.3 shows a schematic of an AFM, operating in tapping mode where the tip oscillates up and down relative to a sample surface. The mode determines the action of the cantilever during operation. However, the detection principle is the same for all three modes. The location of the reflected laser is recorded by a position sensitive photodetector and analysed to produce an image of the sample surface.

Table 3.1. Summary of AFM operation modes [76].

Operation mode	Working principle	Advantages	Disadvantages
Contact mode	Physical contact between tip and sample surface	<ul style="list-style-type: none"> <li>• High scan speed</li> <li>• High resolution</li> </ul>	<ul style="list-style-type: none"> <li>• Damage to soft sample</li> <li>• Lateral forces may produce image artifacts</li> </ul>
Non-contact mode	No contact between tip and sample surface	<ul style="list-style-type: none"> <li>• No damage to sample</li> </ul>	<ul style="list-style-type: none"> <li>• Low resolution</li> <li>• Slower scan speed compared to contact and tapping mode</li> </ul>
Tapping mode	Intermittent and short contact tip and sample surface	<ul style="list-style-type: none"> <li>• High resolution</li> <li>• Minimal damage to sample</li> </ul>	<ul style="list-style-type: none"> <li>• Slower scan speed compared to contact mode</li> </ul>

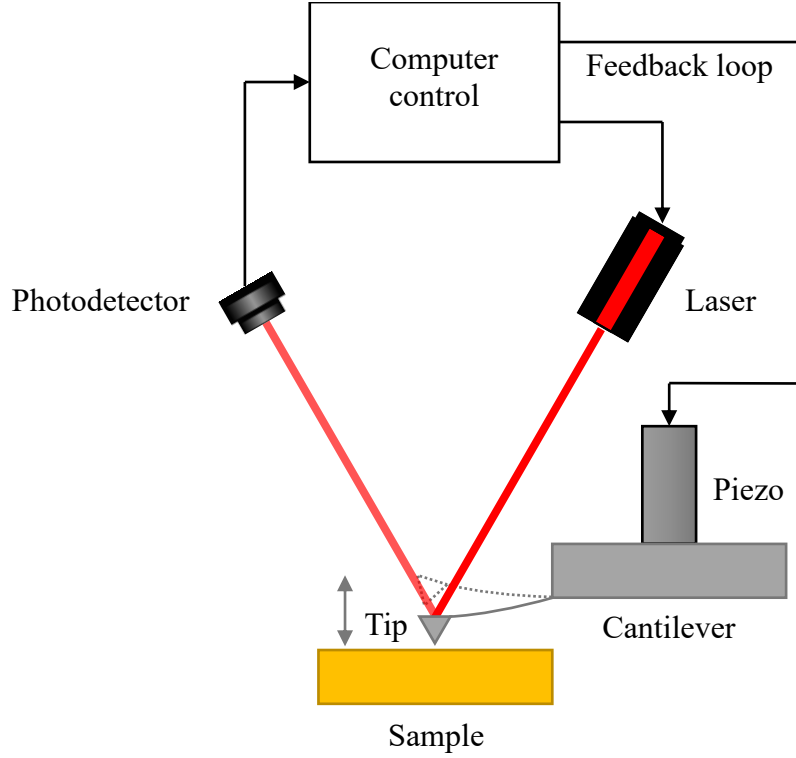


Figure 3.3: A schematic of an atomic force microscope, where the reflected beam picked up by the photodetector is used for analysis and to simultaneously provide a feedback signal to finely adjust the cantilever height or vibrate via a piezoelectric device.

The forces acting on the AFM tip can be approximated by the Lennard-Jones (LJ) potential,  $U_{LJ}$ , which describes the intermolecular interaction between a pair of atoms, and is given by [77]

$$U_{LJ}(r) = 4\varepsilon \left( \left( \frac{\sigma}{r} \right)^{12} - \left( \frac{\sigma}{r} \right)^6 \right), \quad (3.1)$$

where  $\varepsilon$  is the depth of the potential well of the LJ potential,  $r$  is the distance between the centre of the particles, and  $\sigma$  is the distance at  $U_{LJ}(r) = 0$ . Figure 3.4 shows the dimensionless Lennard-Jones potential as a function of interparticle distance,  $r/\sigma$ . The force,  $F$ , is given by the negative of the derivative of the potential energy

$$F(r) = \frac{-\partial U(r)}{\partial r}. \quad (3.2)$$

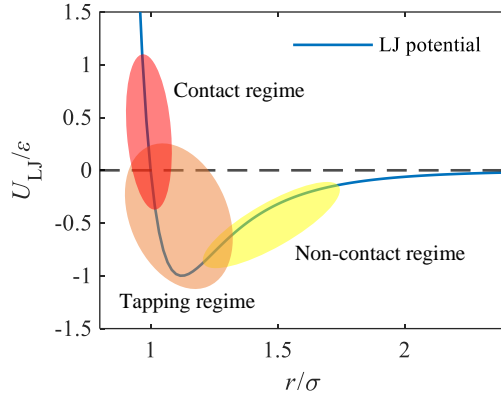


Figure 3.4: Dimensionless Lennard-Jones potential as a function of interparticle distance. The highlighted regions indicate the respective LJ potential regime for each AFM operation mode.

In this thesis, we used a Park XE7 AFM to characterise surface roughness of Au films, its thickness, and modified surfaces with  $\sim 7$  nm radius PointProbe® Plus Non-Contact/Tapping Mode – High Resonance Frequency – Reflex Coating (PPP-NCHR) AFM tip. Unless otherwise specified, measurements were done using non-contact or tapping mode cantilever with a force constant of  $\sim 42 \text{ N m}^{-1}$  and a resonant frequency of  $\sim 300 \text{ kHz}$ .

### 3.4 Four-point probe (4PP)

In 1915, Frank Wenner developed the four-point probe (4PP) [78]. Wenner originally developed the 4PP technique to measure earth electrical resistivity. In 1954, Leopoldo Valdes applied the 4PP technique to measure semiconductor wafer electrical resistivity [79]. Figure 3.5 shows the 4PP setup in a common array configuration with spacing  $d_{s,1}$ ,  $d_{s,2}$ , and  $d_{s,3}$ . For equal probe spacing  $d_s = d_{s,1} = d_{s,2} = d_{s,3}$ , the in-plane electrical resistivity,  $\rho_{r,\perp}$ , is given by

$$\rho_{r,\perp} = C \frac{\pi}{\ln(2)} d_t \frac{V}{I}, \quad (3.3)$$

where  $d_t$  is the thickness,  $I$  is the current,  $V$  is the voltage, and  $C$  is the correction factor [80]. In the case of an isotropic material, the in-plane electrical resistivity is equal to the cross-plane electrical resistivity,  $\rho_{r,\parallel}$ , such that  $\rho_r = \rho_{r,\perp} = \rho_{r,\parallel}$ .

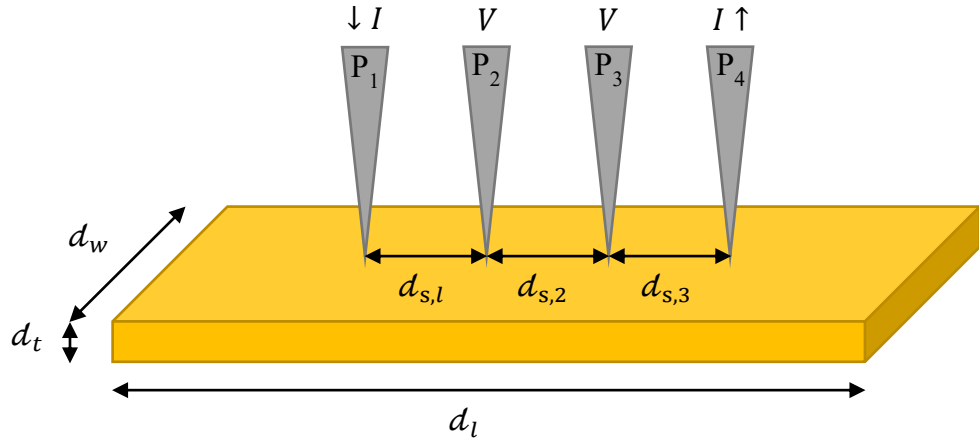


Figure 3.5: Schematic of an 4PP array configuration, where  $d_l$  and  $d_w$  are the length and width of the rectangular material,  $d_t$  is thickness and  $d_s$  is the spacing between probe needles. A current  $I$  is sourced between the outer electronics and the potential drop across the inner electronics is measured.

Electrical conductivity,  $\sigma_c$ , is just the reciprocal of electrical resistivity,  $\sigma_c = 1/\rho_r$ .

An approximate conversion from electrical conductivity to thermal conductivity,  $\kappa$ , can be calculated for highly conductive materials by using the Wiedemann-Franz law

$$\frac{\kappa}{\sigma_c} = LT, \quad (3.4)$$

with:

$$L = \frac{\pi^2}{3} \left( \frac{k_B}{e} \right)^2, \quad (3.5)$$

where  $L$  is the Lorenz number, and  $e$  is the electronic charge. Note that the Lorenz number is roughly a constant, but it is not a constant [81]. The value can vary significantly and can be very dependent on temperature [82]. However, a constant is sufficient for this thesis, as we will only be using this conversion method to inform the thermal conductivity of Au thin films.

### 3.4.1 Geometric correction

A geometric correction factor is considered when sample dimensions are comparable to the probe spacing. Details regarding measurements of anisotropic materials is well documented in literature [83]. The 4PP technique is advantageous as it eliminates any uncertainty due to the length and resistance of the cables. When measuring the centre of a circular sample with diameter,  $d_d$ , approaching to the probe the spacing size, a correction factor is necessary and is given by [84]

$$C = \frac{\ln(2)}{\ln(2) + \ln\left(\frac{d_d^2}{d_s^2} + 3\right) - \ln\left(\frac{d_d^2}{d_s^2} - 3\right)}. \quad (3.6)$$

For  $d_d \gg d_s$ ,  $C \rightarrow 1$ , therefore a correction factor becomes unity.

When measuring the centre of a rectangular sample an empirically determined correction factor is used instead. A correction factor is chosen depending on the combination of the length to width and width to spacing ratios according to tables documented in literature [84]. For other shapes and probe positions, alternative correction factors are required and can be found in literature [84], [85].

### 3.4.1 Cox-Strack method

The Cox-Strack method (CSM) [86] can be used to extract the electrical contact resistance,  $\mathcal{R}_c$ , by measuring the total electrical resistance  $\mathcal{R}_{\text{tot}}$  of a device with the structure as shown in Figure 3.6. The extraction of the parameters is done by applying a multiparameter least squares fitting to the Cox-Strack equation [86]

$$\mathcal{R}_{\text{tot}} = \left(\frac{4\mathcal{R}_c}{\pi}\right) \frac{1}{d_d^2} + \frac{\rho_{r,\parallel}}{\pi} \tan^{-1}\left(\frac{4}{d_d/d_t}\right) \frac{1}{d_d} + \mathcal{R}_0, \quad (3.7)$$

where  $\mathcal{R}_c$  is the top contact resistance,  $\rho_{r,\parallel}$  is the cross-plane electrical resistivity of the layer of interest, and  $\mathcal{R}_0$  is the residual resistance. The first term shows that top contact resistance has an inverse relationship with the area of the contact region. The second term shows the contribution of the cross-plane electrical resistivity of the layer of interest which accounts for the current spreading by the arctangent term. Finally, the residual resistance term account for any substrate contact or backside contact to the ground probe that is invariant with the device diameter.

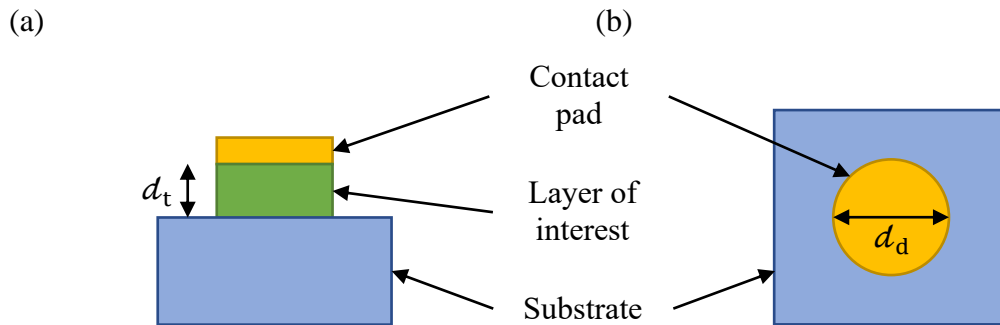


Figure 3.6: (a) Schematic cross-sectional view of a typical multilayer test device with test layer thickness  $d_t$ . (b) A plan view of the same test device in (a) with circular contact pad diameter  $d_d$ . Probe needles  $P_1$  and  $P_2$  are positioned in contact with the top contact pad, while  $P_3$  and  $P_4$  are in contact with the substrate or backside of the layer of interest if possible.

### 3.5 Contact angle goniometry (CAG)

The modern contact angle goniometer (CAG) was developed by William Zisman in the early 1960's while he was working at the Naval Research Laboratory in USA and the was first built by Ramé-Hart also in the USA [87]. Figure 3.7 shows a schematic of a common CAG with a syringe type liquid dispenser. A CAG is typically used to measure the contact angle of a droplet on a given surface and to determine the solid's surface energy. It is also used to determine the surface tension of a given liquid. It may be worth noting that the limitations of the CAG were investigated not long after it was development by Zisman and his colleague, Elaine Shafrin [88]. Typically, the error of a measured contact angle using a modern CAG is up to approximately  $\pm 1^\circ$ . More recently, a study observed that in the superhydrophobic regime, errors could be up to  $\pm 8^\circ$  [89]. The geometry of the droplet is usually described by the Young-Laplace equation and the contact angle can be calculated this way [90]–[93]. A modern CAG uses a charge-coupled device (CCD) camera to capture the shape of the droplet and uses software to detect the edge of the droplet, which passes through a fitting algorithm to calculate the contact angle. Measuring the solid's surface energy using the sessile drop technique gives information about the wettability of a surface [46], [47]. The information of a solid's wettability is commonly used in surface and interface science [94].



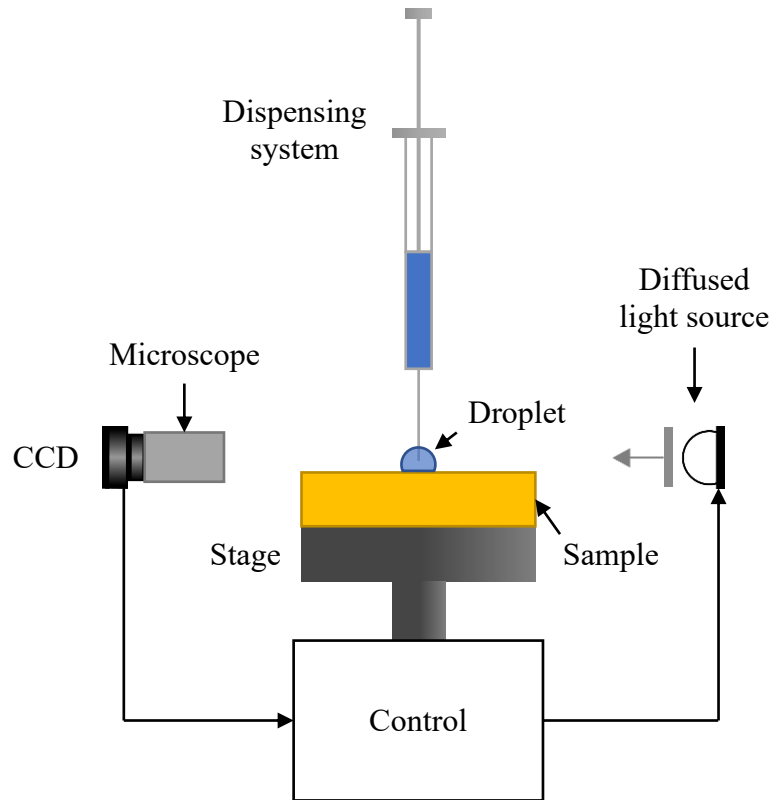


Figure 3.7: A schematic of a contact angle goniometer, with manual focusing microscope.

In this thesis, we used a Ossila L2004A1 CAG to determine the work required to separate solid,  $s$ , and liquid,  $l$ , phase from each other, the work more generally for any different phase known as work of adhesion. The Ossila L2004A1 can measure contact angle in the range of  $5^\circ - 180^\circ$  with maximum measurement accuracy of  $\pm 1^\circ$ . Using the provided software, the whole process of dispensing each droplet can be recorded and then extracted each contact angle using a single frame of the recorded videos.

### 3.5.1 Thermodynamic work of adhesion

There is some finite interfacial energy,  $\gamma$ , when the two phases are in contact with each other. If these two phases are separated completely such that both phases are in contact with air instead, the work of adhesion is equal to the change in energy. The work of adhesion,  $\Delta\gamma_{12}$ , is described by Dupré as [94]

$$\Delta\gamma_{12} = \gamma_1 + \gamma_2 - \gamma_{12}. \quad (3.8)$$

If we consider a solid-liquid system, we can rewrite Eq. (3.8) as

$$\Delta\gamma_{sl} = \gamma_s + \gamma_l - \gamma_{sl}, \quad (3.9)$$

where  $\gamma_s$  is the surface free energy of the solid,  $\gamma_l$  is the surface tension of a liquid, and  $\gamma_{sl}$  is the interfacial tension between the two materials. The contact angle,  $\theta_{ca}$ , comes into play here as measuring  $\gamma_s$  and  $\gamma_{sl}$  is non-trivial. The work of adhesion can be made easier to determine by relating  $\Delta\gamma_{sl}$  with the relatively easily measurable quantity of  $\theta_{ca}$  using the Young equation given by [94]

$$\gamma_s = \gamma_{sl} + \gamma_l \cos \theta_{ca}. \quad (3.10)$$

Combining Eq. (3.8) and (3.9) gives the Young-Dupré equation [94]

$$\Delta\gamma_{sl} = \gamma_l(1 + \cos \theta_{ca}). \quad (3.11)$$

We will use this definition in later chapters when dealing with solid-liquid systems.

### **3.6 Frequency-domain thermorefectance (FDTR)**

In 2009, Aaron Schmidt, Ramez Cheaito, and Matteo Chiesa presented a frequency-domain thermorefectance (FDTR) technique to explore thermal properties of homogeneous materials and thin films [95]. The FDTR technique is a variation of the time-domain thermorefectance (TDTR) technique. The details of other variations of the TDTR technique is well documented in the literature [96]. The FDTR technique is a non-contact optical metrology technique and is commonly used to measure thermal conductivity, and volumetric heat capacity,  $C_V$ , of thin films, where volumetric heat capacity is a product of material density,  $\rho$ , and specific heat capacity,  $c_p$ , as well as thermal boundary conductance across

interfaces of dissimilar materials. Schmidt *et al.* presented two FDTR configurations; one retains the use of pulsed laser and a mechanical time delay stage from the TDTR technique, while the other uses two continuous wave (CW) lasers and does not require a mechanical time delay stage. Due to the capabilities and high spatial resolution of the FDTR technique, it has gained popularity very quickly upon its development [18], [97]–[99]. The use of CW lasers considerably reduces the cost and operational complexity of the technique.

FDTR and other thermoreflectance techniques such as TDTR and charge-coupled device based thermoreflectance (CCD-TR) relies on thermoreflectance effect, where there is a change in reflectivity,  $\Delta R$ , of a material due to a change in temperature [54], [100]. The thermoreflectance phenomenon and its effect on various materials has been investigated qualitatively prior to the early 1980's [101]–[104]. It was found that the change in reflectivity can be explained by the change in the band gap of the material and is the result of two phenomena: one being the change in lattice constant due to thermal expansion or contraction; the other being a broadening or narrowing due to a change in the number of electron-phonon interactions.

The thermoreflectance coefficient,  $\kappa_{TR}$ , is used to quantify the change in reflectivity per unit temperature, and its relationship with  $R$  and  $T$  is given by

$$\frac{\Delta R}{R} = \left( \frac{1}{R} \frac{\partial R}{\partial T} \right) \Delta T = \kappa_{TR} \Delta T, \quad (3.12)$$

with:

$$R = \frac{(n - 1)^2 + k_{\epsilon}^2}{(n + 1)^2 + k_{\epsilon}^2} \quad (3.13)$$

where  $n$  is the refractive index, and  $k_{\epsilon}$  is the extinction coefficient of the material. A layer of thin metal film acts as a thermorefectance transducer, and we use this to investigate thermal properties of various thin films and interfaces in the diffusion regime. More recently, quantitative investigations led to better understanding in selecting more appropriate metal as thermorefectance transducer for certain laser wavelengths and vice versa [105]. Figure 3.8(a) and (b) shows the absorbance and thermorefectance spectrum of several candidate materials as thermorefectance transducer over a range of wavelengths, respectively.

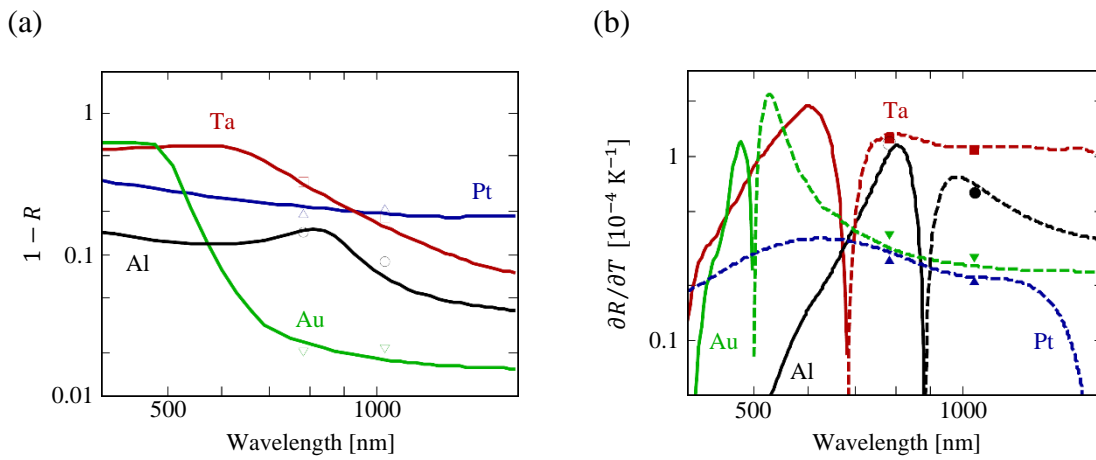


Figure 3.8: (a) Absorbance, and (b) thermorefectance spectrum over a range of wavelengths, where the dashed lines indicate negative values. Taken from literature [105].

### 3.6.1 Instrumentation and Optics

In this work, the implementation of FDTR is based on the free space CW lasers configuration of the thermorefectance method. Figure 3.9(a) shows a schematic containing the essential features of the FDTR system built in specifically for this project, while Figure 3.9(b) shows a picture of the optical setup. The system is built around two single mode CW diode lasers (Toptica Photonics iBEAM SMART 405, and 515) with maximum output power of 120 mW for each laser. One laser is to provide the necessary heat source with a wavelength of 403 nm, and the other laser is to measure the temperature change with a wavelength of 511 nm. With the chosen laser wavelengths, Au is used as transducer as it has high optical absorption

for local heating with significant sensitivity, as well as it being resistant to oxidation and not reacting with any common working fluids for thermal management applications.

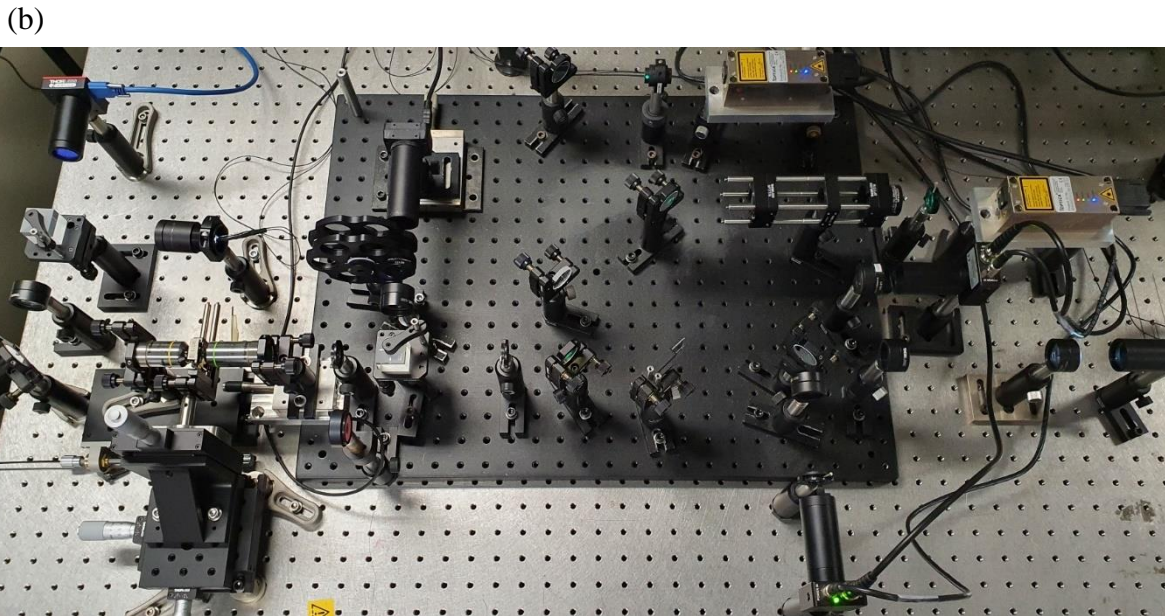
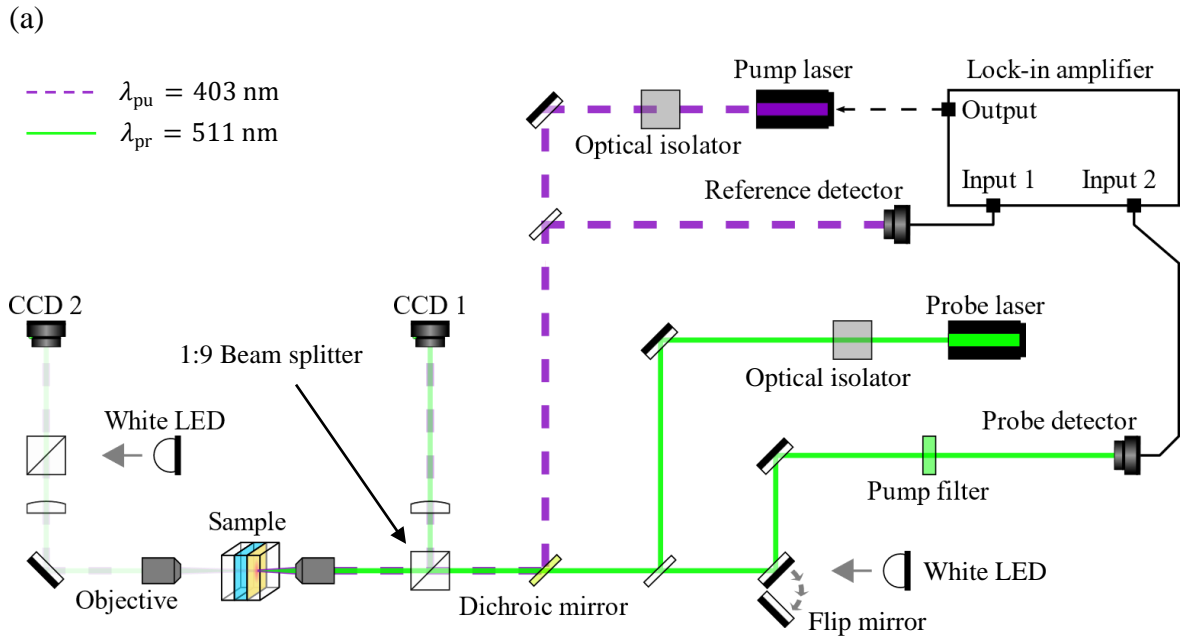


Figure 3.9: (a) A schematic of the FDTR setup used in this work. A charge-coupled device (CCD) camera is used check that the pump and probe beams are coaxially aligned and Gaussian-shaped. Optical isolators (OI) are used to prevent unwanted feedback into the respective laser cavity. Matching detectors, cables, and optical paths for the pump and probe beams are used and practiced, respectively, to minimize additional phase difference to the measured phase response. (b) Picture of the FDTR setup that was built in the Nanothermal Research Group optical characterisation lab.

The pump beam passes through a Thorlabs optical isolator (OI) that prevents back reflections from destabilising the laser. The pump beam passes through the OI and is then collimated using a lens, however, it is worth noting that a perfectly collimated beam with  $1/e^2$  radius,  $w_0$ , will diverge as a function of propagation distance,  $z$ , by [106]

$$w = w_0 \sqrt{1 + \left(\frac{\lambda z}{\pi w_0^2}\right)^2}, \quad (3.14)$$

where  $w$  is the resulting  $1/e^2$  beam radius. From Eq. (3.14),  $\sim 0.02\%$  beam expansion should be expected from OI to the microscope objective. For TDTR,  $z$  varies under operation due to the change in optical path length by a mechanical stage. For FDTR,  $z$  is instead fixed under operation, and this means that the optical path should not be a contributing factor to any changes in the spot shape and size. The ability to maintain a more constant spot size and shape is advantageous as heat flux is proportional to the heated surface area.

After the pump beam passes through the OI, the beam is then guided by reflective mirrors and is reflected towards where the sample is positioned by a dichroic mirror. Similarly, the probe beam is also guided by reflective mirrors, but the beam then passes through the dichroic mirror. Both beams are coaxially aligned and focused onto the sample with a microscope objective. A 1:9 ratio cube beam splitter is used to feed a small fraction of the light to the first camera (CCD 1). The first camera serves multiple purposes, from beam alignment to monitoring sample surface conditions. It is also used for spot size characterisation which will be discussed in Section 3.5.3.

Two matching photodetectors (Thorlabs PDA10A-EC 200-1100 nm Si amplified detectors) are used to capture the reflected pump and probe beams. The photodetectors convert light signals into electronic signals. The converted electrical signal is then processed

by the lock-in amplifier. A lock-in amplifier (Zurich Instruments HF2LI) is used to measure the in-phase, and out-of-phase, signals at a given frequency. The signal and signal analysis will be discussed in Section 3.5.4. The lock-in amplifier also serves as a function generator to provide the necessary pump laser signal for modulated heating. The modulated frequency sweep we used for the FDTR measurements is in the range of 10 kHz – 20 MHz.

### 3.6.2 Spot size characterisation

The Toptica Photonics single mode CW diode lasers in this FDTR setup produces lowest order transverse electromagnetic or TEM<sub>00</sub> beam with an approximately Gaussian intensity profile,  $I_V(d_r)$ , that is related to  $1/e^2$  radius  $w_0$  by [107]

$$I_V(d_r) = \frac{2P}{\pi w_0^2} e^{-\frac{2d_r^2}{w_0^2}}, \quad (3.15)$$

where  $P$  is the beam power and  $d_r$  is the distance from the centre of the beam.

The knife-edge technique is a common method in measuring Gaussian beam waist [108]. Since it is our intention for this setup to be compatible with a custom-built pressure-controlled environmental chamber, we favoured using the CCD imaging technique as the imaging components can be at some distance away and not interfering with the sample stage. Using an ultra-precision micro-pillar matrix sample as shown in Figure 3.10(a), the visual length,  $d_{px}$ , of each square pixel of the first CCD camera is

$$d_{px} \simeq \frac{6 \mu\text{m}}{M \left( \frac{20 \text{ cm}}{16.8 \text{ cm}} \right)} = \frac{5.04}{M} \mu\text{m}, \quad (3.16)$$

where  $d_{px}$ , calculated based on the  $6 \mu\text{m} \times 6 \mu\text{m}$  pixel of the first CCD camera, is the distance ratio of the optical path between the objective and the 20 cm camera focus lens and

the camera to the same focus lens, and  $M$  is the magnification of the microscope objective. Magnification at  $10\times$  and  $20\times$  are commonly used for FDTR measurement. Unless otherwise specified, all measurements presented in this thesis were taken using the Olympus PLN  $20\times$  infinity-corrected objective, therefore we usually have  $d_{px} \simeq 2.52\ \mu\text{m}$ . With this information, the full beam width definition at  $1/e^2$  was used, namely

$$2w = \frac{\sqrt{2}\text{FWHM}}{\sqrt{\ln 2}}, \quad (3.17)$$

where FWHM is the full width at half maximum of the point spread function (PSF). This is related to the standard deviation,  $\sigma_{sd}$ , of a Gaussian function by

$$\text{FWHM} = 2\sqrt{2\ln 2}\sigma_{sd}. \quad (3.18)$$

Figure 3.10(b) shows the unsaturated mean spot images on the transducer surface using the first CCD camera and their respective PSF. We use the `ezfit` Matlab function developed by Frederic Moisy to fit the cross section profile of the spots and determine  $\sigma_{sd}$  [109]. Typically, we take an average of ten spot images for the pump and probe, respectively, before and after each FDTR measurements for more accurate representation of the spots and to observe for spot drifting which could nullify FDTR measurements. We calibrated the setup to achieve uncertainty of spot size measurement within 5%, comparable to that of the knife's edge method.



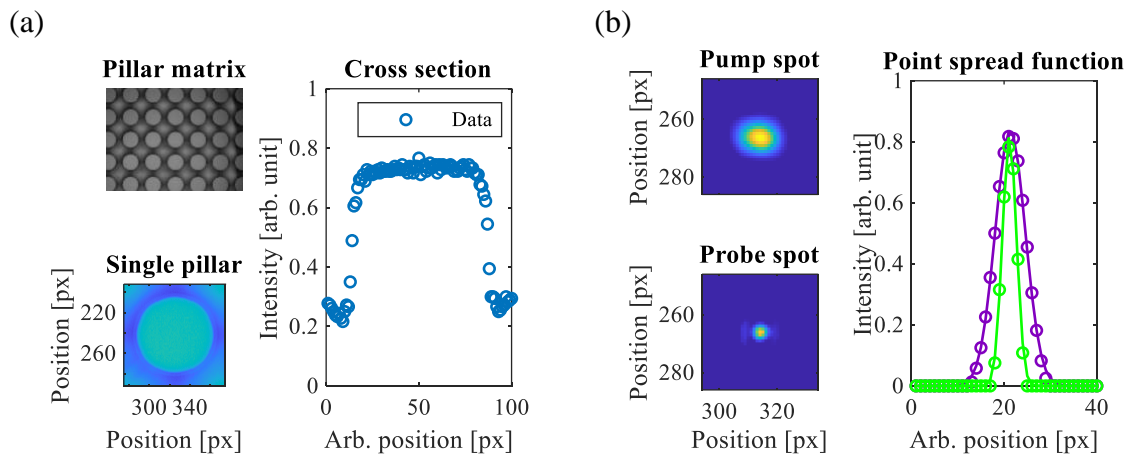


Figure 3.10: (a) A 10  $\mu\text{m}$  radius pillar from an ultra-high precision micro-pillar matrix sample fabricated by Ryan Enright was used to calibrate the first CCD camera for spot size measurements. (b) An example of the pump and probe spot size imaged using the calibrated CCD camera and their respective cross section, where the circle markers and solid lines represent data and fit (using `ezfit` Matlab function [109]), respectively.

### 3.6.3 Fabrication and characterisation of thermoreflectance transducer

As discussed in earlier sections, Au is the metal of choice for this setup. The optical characteristics and thickness of the transducer are key contributors to the accuracy of FDTR measurements. A typical metal thermoreflectance transducer thickness is within the range of 50 nm – 100 nm [110]. If the transducer is too thin, light could reach to the next layer and its reflection could interfere with the measurements. On the other hand, if the layer is too thick, the diffusivity of excited electrons in the transducer also interfere with the measurements [111].

Metal transducers for TDTR and FDTR are usually fabricated using physical vapor deposition, either through sputtering or evaporation. Depending on the deposition method and tool, characteristics of fabricated thin films could vary. It is common to fabricate metal transducers on the thicker end of the spectrum to minimise optical transmission to the next layer; however, this may depend on the application. An important characteristic of a metal transducer is the surface roughness, as the surface morphology also influences the results of

the measurements. From an optical perspective, the transducer should have a root mean square (RMS) surface roughness  $< 15$  nm [112].

In this thesis, we used a Ferrotec Temescal FC-2000 electron beam evaporation system to fabricate 80 – 100 nm thick Au transducers for the FDTR measurements. On the thicker side of the spectrum, ballistic electrons will traverse the film in 100 fs, assuming electron velocities are close to the Fermi velocity at  $\sim 10^6$  ms<sup>-1</sup> [113]. Therefore, we neglect any ballistic effects. The film thickness is mainly determined by the electron-beam power, deposition time, and deposition rate, where the deposition rate is monitored by a quartz crystal microbalance. The thickness was verified using contact stylus profilometry [114]. Figure 3.11 shows the RMS roughness of a typical Au transducer used is  $< 15$  nm.

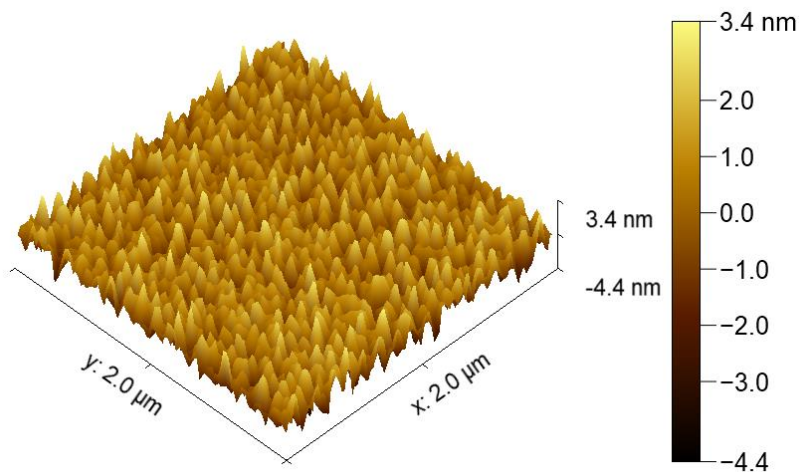


Figure 3.11: A 3D AFM image of a typical Au transducer surface fabricated using the Ferrotec Temescal FC-2000 electron beam evaporation system.

### 3.6.4 Heat transfer and signal analysis

The frequency response of the sample surface temperature as shown in Figure 3.12, measured by a lock-in amplifier, can be described by the multilayer heat diffusion which is well documented in literature [95], [115]. Thermal properties of the layer of interest are

usually extracted by considering the inverse problem as we go on to discuss. Several adaptations have been made since FDTR was introduced to account for anisotropic materials using beam-offset FDTR [116], bi-directional conduction model to deal with bi-directional heat flows [117], and others [118], [119]. Without reproducing all of the aforementioned theories, this section will present the only the equations and transforms needed to ultimately solve the heat diffusion equation of a multilayer structure.

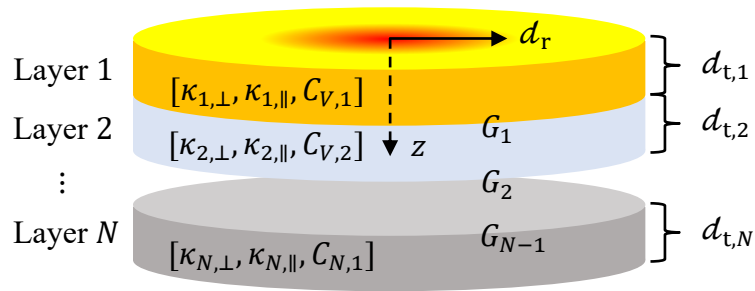


Figure 3.12: A schematic of a multi-layered stacked structure with parameters for each layer in the heat diffusion model. The red region on top of layer  $i = 1$  represents a Gaussian heat source applied on the surface by the pump and probe beams. Quantities with subscript  $\perp$  or  $\parallel$  are the in-plane or cross-plane, and are perpendicular or parallel relative to the pump beam, respectively. For isotropic materials, in-plane thermal conductivity and cross-plane thermal conductivity are equal. The TBC in the model is the TBC between the layer of interest and the next layer.

A thermal wave is generated when a modulated heat source is applied onto the transducer layer. A multilayer heat diffusion model may be used to relate the surface temperature amplitude, and phase, to the heat source [120]. With this established, we will discuss how the heat diffusion model is connected to in-phase and out-of-phase signals by following the exposition from [115].

The ideal lock-in amplifier precisely measures the amplitude and phase,  $\phi$ , of the harmonic component of the reflected signals at frequency  $\omega$ . For a reference wave  $e^{i\omega t}$ , the solution can be mathematically expressed as a complex number such that

$$Ae^{i(\omega t - \phi)} = \mathcal{Z}(\omega)e^{i\omega t}, \quad (3.19)$$

where  $t$  is time, and  $\mathcal{Z}(\omega)$  is a transfer function which contains thermal properties of the system in question. Since the chosen FDTR configuration uses CW lasers, the transfer function is given by [95]

$$\mathcal{Z}(\omega) = A_{\text{li}}H(\omega), \quad (3.20)$$

with:

$$A_{\text{li}} = \frac{1}{2}P_{\text{pu}}P_{\text{pr}}(1 - R_{\lambda_{\text{pr}}})\left(\frac{\partial R}{\partial T_{\lambda_{\text{pr}}}}\right)\alpha_{\text{gr}\lambda_{\text{pr}}}, \quad (3.21)$$

where  $A_{\text{li}}$  is the voltage amplitude detected by the lock-in amplifier,  $H(\omega)$  is the frequency response, and  $\alpha_{\text{gr}}$  is the product of the gain and responsivity of the photodetector and photodiode, respectively, at probe laser wavelength, and subscripts pu and pr represent pump and probe, respectively. If the thermal properties of the system can be considered constant under induced heating, the frequency response can be used to determine the thermal properties and not be affected by voltage amplitude.

We reproduce the derivation of an explicit expression of  $H(\omega)$  for the multilayer structure as shown Figure 3.12 [115]. This is a multilayer heat transfer problem in cylindrical coordinates. Heat transfer problems may usually be described by the classical diffusion model developed by Joseph Fourier [121]. The heat conduction equation for each layer in the stack structure is given by [122]

$$\frac{\kappa_{\perp}}{d_r} \frac{\partial}{\partial d_r} \left( d_r \frac{\partial T}{\partial d_r} \right) + \kappa_{\parallel} \frac{\partial^2 T}{\partial z^2} = C_V \frac{\partial T}{\partial t}. \quad (3.22)$$

The solution of Eq. (3.22) is obtained using the conduction heat transfer theory developed by Horatio Carslaw and John Jaeger [120] with boundary conditions:

$$T(z = 0, d_r, t \neq 0) = T_{\text{top}}, \quad \left. \frac{\partial T(z, d_r, t \neq 0)}{\partial z} \right|_{z=0} = \frac{-q_{\text{top}}}{\kappa_{\parallel}}; \quad (3.23)$$

$$T(z = d_t, d_r, t \neq 0) = T_{\text{bottom}}, \quad \left. \frac{\partial T(z, d_r, t \neq 0)}{\partial z} \right|_{z=t} = \frac{-q_{\text{bottom}}}{\kappa_{\parallel}}; \quad (3.24)$$

$$T(z, d_r, t = 0) = 0; \quad (3.25)$$

where the subscripts top and bottom refers to the top and bottom of the surface, respectively. We let Eq. (3.25) equal to zero as we are only interested in the relative change of the surface temperature.

The Hankel transform is used to handle this cylindrical symmetrical problem. A Hankel transform followed by a Fourier transform is applied to get

$$\frac{\partial^2 T(z, \ell_H, \omega)}{\partial z^2} = \frac{\kappa_{\perp} \ell_H^2 + i\omega C_V}{\kappa_{\parallel}} T(z, \ell_H, \omega), \quad (3.26)$$

where  $\ell_H$  is the Hankel transform variable. This is done to simplify the solution and transform from time-domain to frequency-domain. We refer the reader, for concepts of Fourier and Hankel transforms, to textbooks as they are extensively covered in heat transfer courses [26]. In-depth details of the solution can be found in literature [123]. To simplify Eq. (3.26), we let

$$\Lambda^2 = \frac{\kappa_{\perp} \ell_H^2 + i\omega C_V}{\kappa_{\parallel}}. \quad (3.27)$$

Using this simplification, we can rewrite Eq. (3.26) as

$$\frac{\partial^2 T(z, \ell_H, \omega)}{\partial z^2} - \Lambda^2 T(z, \ell_H, \omega) = 0, \quad (3.28)$$

Following [115], we take the hyperbolic functions and get a solution in the form:

$$T(z, \ell_H, \omega) = A \cosh(\Lambda z) + B \sinh(\Lambda z), \quad (3.29)$$

where  $A$  and  $B$  are constants and is found by applying Eq. (3.23) - (3.25), but with  $\ell_H$  and  $\omega$  instead of  $d_r$  and  $t$  for the Hankel and Fourier transforms. With the new boundary conditions, we get the temperature and heat flux solution in  $\ell_H$ -space with the form:

$$T(z, \ell_H, \omega) = T_{\text{top}} \cosh(\Lambda z) - \frac{q_{\text{top}}}{\kappa_{\parallel} \Lambda} \sinh(\Lambda z) \quad (3.30)$$

$$q(z, \ell_H, \omega) = T_{\text{top}} \Lambda \sinh(\Lambda z) - q_{\text{top}} \cosh(\Lambda z) \quad (3.31)$$

Referring to the multilayer stack structure, at layer  $i$ , the temperature and heat flux on top of the surface is related to the bottom can be written as a matrix form

$$\begin{bmatrix} T_{\text{bottom},i} \\ q_{\text{bottom},i} \end{bmatrix} = \mathbf{M}_i \begin{bmatrix} T_{\text{top},i} \\ q_{\text{top},i} \end{bmatrix}, \quad \mathbf{M}_i = \begin{bmatrix} \cosh(\Lambda_i d_{t,i}) & \frac{-\sinh(\Lambda_i d_{t,i})}{\kappa_{\parallel,i} \Lambda_i} \\ -\kappa_{\parallel,i} \Lambda_i \sinh(\Lambda_i d_{t,i}) & \cosh(\Lambda_i d_{t,i}) \end{bmatrix}. \quad (3.32)$$

The TBC between layer  $i$  and  $i + 1$  can be extracted by taking the limit as the heat capacity of the  $i^{\text{th}}$  layer approaches to zero and by letting  $G_i = \kappa_{\parallel,i} / d_{t,i}$ , the relationship between TBC, and heat flux and temperature on both sides can also be written in matrix form

$$\begin{bmatrix} T_{\text{top},i+1} \\ q_{\text{top},i+1} \end{bmatrix} = \begin{bmatrix} 1 & -G_i^{-1} \\ 0 & 1 \end{bmatrix} \begin{bmatrix} T_{\text{bottom},i} \\ q_{\text{bot,tom}i} \end{bmatrix}. \quad (3.33)$$

Combining Eq. (3.32) and (3.33), the heat propagation across  $N$ -layers can be generalized through matrix multiplication [120]

$$\begin{bmatrix} T_{\text{bottom}} \\ q_{\text{bottom}} \end{bmatrix} = \mathbf{M}_N \mathbf{M}_{N-1} \cdots \mathbf{M}_2 \mathbf{M}_1 \begin{bmatrix} T_{\text{top}} \\ q_{\text{top}} \end{bmatrix} = \prod_{i=N}^1 \mathbf{M}_i \begin{bmatrix} T_{\text{top}} \\ q_{\text{top}} \end{bmatrix} = \begin{bmatrix} A & B \\ C & D \end{bmatrix} \begin{bmatrix} T_{\text{top}} \\ q_{\text{top}} \end{bmatrix}. \quad (3.34)$$

On the  $N^{\text{th}}$  layer, if we assume that there is no heat flux exiting the sample, then Eq. (3.34) can be reduced to  $CT_{\text{top}} + Dq_{\text{top}} = 0$  and therefore

$$T_{\text{top}} = \mathcal{G}(\kappa_H, \omega) q_{\text{top}} = \frac{-D}{C} q_{\text{top}}. \quad (3.35)$$

where  $\mathcal{G}$  is the detected temperature response which satisfies the conditions of the Green's function [54].

So far, we described the heat propagation in a multilayer structure due to a point heat source at the surface. However, the heat source in FDTR experiments is a focused laser beam of finite size. Recalling Eq. (3.15), the intensity distribution in the focal plane of the pump beam can be approximated by a Gaussian distribution:

$$I_V(d_r) = \frac{2P_{\text{pu,abs}}}{\pi w_{\text{pu}}^2} e^{-\frac{2d_r^2}{w_{\text{pu}}^2}}, \quad (3.36)$$

where  $P_{\text{pu,abs}}$  is the total absorbed pump power. We applied the same treatment as the heat conduction equation and take the Hankel transform of Eq. (3.36) and get

$$I_V(\kappa_H) = \frac{P_{\text{pu,abs}}}{2\pi} e^{-\frac{\kappa_H^2 w_{\text{pu}}^2}{8}}. \quad (3.37)$$

Combining Eq. (3.35) and (3.36) we get the surface temperature in  $k_H$ -space:

$$T_{\text{top}}(k_H) = \left(\frac{-D}{C}\right) \frac{P_{\text{pu,abs}}}{2\pi} e^{-\frac{k_H^2 w_{\text{pu}}^2}{8}}. \quad (3.38)$$

Now we take the inverse Hankel transform of Eq. (3.38) so that the surface temperature is in real space:

$$T_{\text{top}}(d_r) = \int_0^\infty J_0(k_H d_r) \left(\frac{-D}{C}\right) \frac{P_{\text{pu,abs}}}{2\pi} e^{-\frac{k_H^2 w_{\text{pu}}^2}{8}} d k_H, \quad (3.39)$$

where  $J_0(k_H d_r)$  is the zero-order Bessel function of the first kind. Since the pump and probe beams are coaxially aligned, we establish an equation similarly for the probe beam such that

$$q_{\text{top}} = \frac{2}{\pi d_r} e^{-\frac{2d_r^2}{w_{\text{pr}}^2}}. \quad (3.40)$$

Taking the product of the weighted average of Eq. (3.39) and the intensity distribution of the probe beam described by Eq. (3.40) we get the final frequency response as

$$H(\omega) = \int_0^\infty \frac{2}{\pi w_{\text{pr}}^2} e^{-\frac{2d_r^2}{w_{\text{pr}}^2}} 2\pi d_r d d_r \int_0^\infty J_0(k_H d_r) \left(\frac{-D}{C}\right) \frac{P_{\text{pu,abs}}}{2\pi} e^{-\frac{k_H^2 w_{\text{pu}}^2}{8}} k_H d k_H. \quad (3.41)$$

Using Eq. (3.36) and (3.37), Eq. (3.41) can be rearranged such that the final frequency response is reduced onto a single integral over only the transform variable which is solved using Matlab:

$$H(\omega) = \frac{P_{\text{pu,abs}}}{2\pi} \int_0^\infty \left(\frac{-D}{C}\right) e^{-\frac{k_H^2 (w_{\text{pu}}^2 + w_{\text{pr}}^2)}{8}} k_H d k_H. \quad (3.42)$$



The measured in-phase,  $V_{\text{in}}$ , and out-of-phase,  $V_{\text{out}}$ , components of the frequency response is given by the real and imaginary part of  $H(\omega)$ , respectively.

$$V_{\text{in}} = \text{Re}\{H(\omega)\} \quad (3.43)$$

$$V_{\text{out}} = \text{Im}\{H(\omega)\} \quad (3.44)$$

It is common to plot  $-V_{\text{in}}/V_{\text{out}}$  as a function of frequency to interpolate the thermal behaviour or extrapolate beyond the modulation frequency range, especially for data from optical techniques based on pulsed lasers. However, we opt to present the data with phase lag signal  $\phi_{\text{li}}$ , as  $\phi_{\text{li}}$  changes dramatically when compared to  $-V_{\text{in}}/V_{\text{out}}$  as a function frequency, and  $\phi_{\text{li}}$  is given by

$$\phi_{\text{li}} = \tan^{-1} \left( \frac{\text{Im}\{H(\omega)\}}{\text{Re}\{H(\omega)\}} \right) - \phi_{\text{ext}}. \quad (3.45)$$

Here,  $\phi_{\text{ext}}$  is the total external phase difference introduced by the optical paths and electronics, discussed in Section 3.5.1. Notice that constant  $A_{\text{li}}$  has been completely dropped off when taking the ratio of the in-phase and out-of-phase frequency response. Although  $A_{\text{li}}$  gives information about the power of the induced heating, surface reflectivity, thermorefectance coefficient, and detection gain, which can be extracted if the data of the pure in-phase amplitude is fitted. However, to reduce uncertainties, we focused on fitting for thermal properties instead. We fit the data of the frequency dependent phase response using the `lsqnonlin` Matlab function, which employs a trust-region-reflective least squares multiparameter fitting algorithm.

Figure 3.13 shows typical FDTR phase lag data and fit for a fused silica sample with a 90 nm thick Au transducer on top. Unless otherwise specified, each data point is a 1000 sample average and is the mean of three measurements at three different locations. The

fitting ability is largely dictated by the sample geometry, especially layer thicknesses as it is limited by the thermal penetration depth or thermal diffusion length,  $l_d$ , the latter is given by

$$l_d = \sqrt{\frac{2\alpha_d}{\omega}}, \quad (3.46)$$

where  $\alpha_d = \kappa/C_V$  is the thermal diffusivity. For frequency range 1 kHz – 50 MHz, the thermal diffusion length in SiO<sub>2</sub> varies from 16  $\mu\text{m}$  to 71 nm with  $\alpha_d = 8 \times 10^{-7} \text{ m}^2 \text{ s}^{-1}$ .

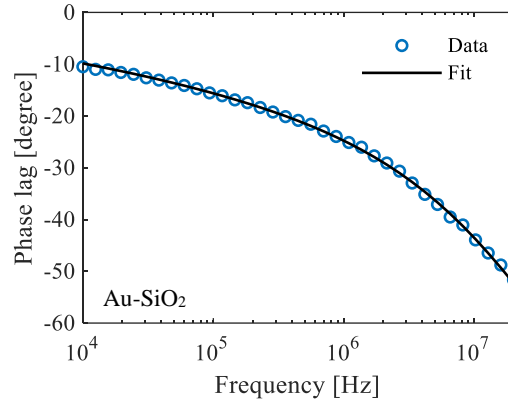


Figure 3.13: A typical FDTR phase lag data and fit for a fused silica sample with 90 nm thick Au transducer layer on top. The thermal conductivity of the SiO<sub>2</sub> was fitted to be  $\kappa = 1.38 \text{ W m}^{-1} \text{ K}^{-1}$  using Eq. (3.45).

### 3.6.5 Sensitivity analysis

The fitting function theoretically can fit for any, and even several, thermal parameters simultaneously for the layer of interest. However, thermal parameters can only be accurately extracted if there is enough sensitivity for the parameters to influence the phase lag. The experimental phase measurement typically has a  $0.1^\circ$  standard deviation in phase noise. To understand sensitivity to a particular parameter, we calculated the phase difference,  $\Delta\phi$ , by keeping all parameters constant except the parameter of interest to determine how finite

changes of the variable influence the phase lag profile. Figure 3.14(a) shows the calculated the phase difference if the SiO<sub>2</sub> thermal conductivity is shifted by  $\pm 10\%$ .

A more standardised way to represent the sensitivity of a thermal parameter,  $x$ , is given by [124]

$$\mathcal{S}_x(\omega) = \frac{d\phi(\omega)}{d \ln x}. \quad (3.47)$$

A logarithmic derivative is used here as it normalises the absolute magnitude of the parameter  $x$ . Figure 3.14(b) indicates unique sensitivity to the SiO<sub>2</sub> thermal conductivity and volumetric heat capacity, but the sensitivity to the thermal conductivity has a vanishing point at around 180 kHz. In the 1D limit, the sensitivity to the thermal conductivity and volumetric heat capacity become indistinguishable and is weighted as the thermal effusivity,  $\sqrt{\kappa C_V}$ . We also used Eq. (3.47) to identify appropriate frequency range to better fit for TBC as  $\phi$  is only sensitive to the TBC in a relatively narrow frequency range.

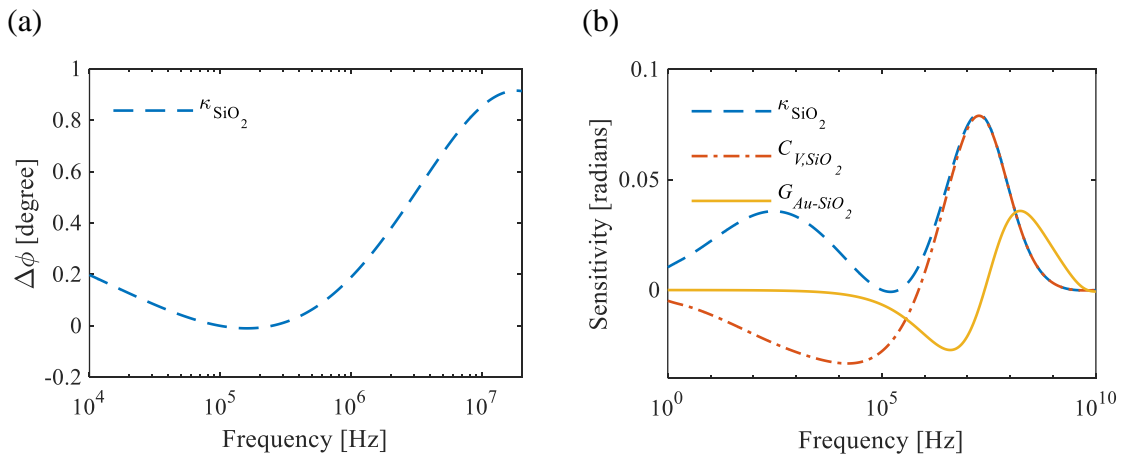


Figure 3.14: Using the measured values of the Au-SiO<sub>2</sub> sample: (a) A phase difference plot, where the phase difference is calculated by subtracting the phase lag with  $-10\%$  SiO<sub>2</sub> thermal conductivity to the phase lag with  $+10\%$  SiO<sub>2</sub> thermal conductivity. (b) Theoretical sensitivity to the SiO<sub>2</sub> thermal conductivity and volumetric heat capacity, and the TBC across Au-SiO<sub>2</sub> interface were calculated using Eq. (3.47).

### 3.6.6 Uncertainty analysis

Typically, several thermal parameters are extracted simultaneously when fitting FDTR data with the thermal model. There are four or five parameters for each layer depending on whether the cross-plane thermal conductivity is equal to the in-plane thermal conductivity,  $\kappa = \kappa_{\perp} = \kappa_{\parallel}$ , or not,  $\kappa_{\perp} \neq \kappa_{\parallel}$ . For the most basic two-layer structure, where both layers are isotropic and the test layer can be considered semi-infinite, there are nine thermal parameters. For structures with more layers and the potential for anisotropy, several more thermal parameters could be involved in the fitting process. This means that the fitted parameters could carry high degree of uncertainty. Including other fitting parameters such as pump and probe beam waists (i.e., beam radius minimum), and understanding how these propagation errors influence the final result is paramount for FDTR and almost every other experiment to produce reliable results [125].

We determine the confidence interval by using a conservative but robust Monte Carlo method. Figure 3.15 shows a flow chart of the Monte Carlo method being applied to FDTR data. Random values are selected for each relevant input parameter and the set of values chosen are used in the fitting process to produce fitted parameter(s). The random input parameters are bounded by their uncertainties, for example, the Au transducers were not fabricated with precise thickness and thermal parameters. We measured the transducers' thickness using AFM and contact stylus profilometry, and as a result, some uncertainty is associated to the measured thickness. We applied a Gaussian distribution about the thickness, bounded by the thickness uncertainty as one of the random input parameters. Similarly for the transducers' thermal conductivity, taking the bulk Au value is inappropriate since a significant portion of the heat carried by phonon, with phonon mean-free-paths longer than the transducer film itself [126]. We measured the electrical conductivity as described in Section 3.1 and converted the electrical conductivity into thermal conductivity

by using Wiedemann-Franz law as described in Section 3.1.1. We used a Gaussian distribution about the thermal conductivity, bounded by its uncertainty defined at 10%. We applied this random selection wherever it was appropriate and possible to fit the data. We also applied a uniform random multiplier between 0.1 and 10 to our best initial guess values to ensure that the best fit values correspond to a unique global minimum.

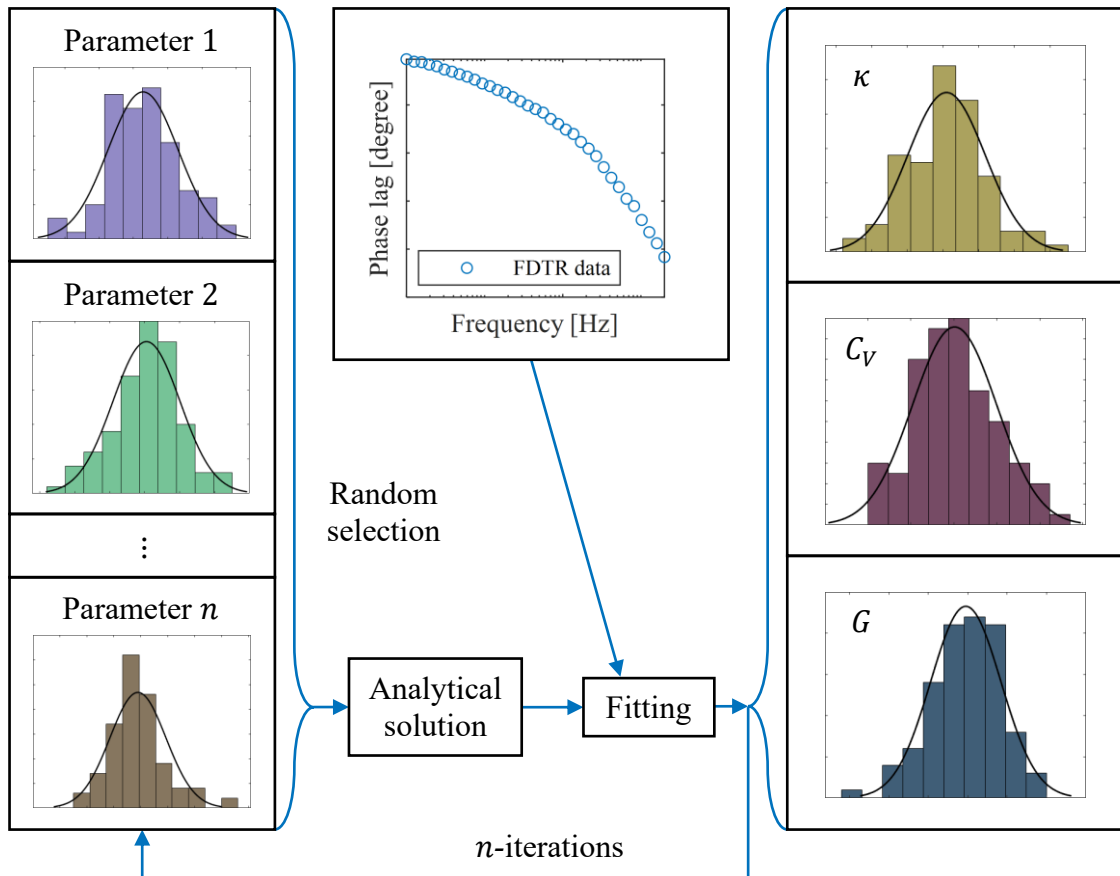


Figure 3.15: A flow chart of the Monte Carlo method being applied to FDTR data, where the missing vertical axis is the count scale, and the horizontal axis is the parameter value scale with their respective unit. Adapted from literature [127].

To extract confidence values, the histogram is fitted using a log-normal fit, where the probability density function,  $f_x$ , of a lognormal distribution is given by [128]

$$f_x\{x|\mu, \sigma_{sd}\} = \frac{1}{\sqrt{2\pi}\sigma_{sd}x} e^{-\frac{(\ln x - \mu)^2}{2\sigma_{sd}^2}}, \quad x \in \mathbb{N}_1, \quad (3.48)$$

where  $\mu$  is the mean of the distribution. For a log-normal distribution, the lower confidence interval  $CI_{lb}$  and upper interval  $CI_{ub}$  at 68.27%, 95.45% or 99.73% can be determined by using Eq. (3.49) and (3.50) with superscript  $j = 1, 2$  or  $3$ , respectively.

$$CI_{lb} = \frac{e^{\mu}}{e^{\sigma_{sd}^j}}, \quad (3.49)$$

$$CI_{ub} = e^{\mu} e^{\sigma_{sd}^j}. \quad (3.50)$$

Unless otherwise specified, the fitting routine was repeated 1000 times for all Monte Carlo analysis presented in this thesis. Using the resulting fitted parameter distribution, a 2-sigma standard deviation (i.e.,  $j = 2$ ) is typically applied to attain the 95% confidence intervals which defines the FDTR result uncertainty.

### 3.7 Summary

In this chapter, we introduced all the key characterisation methods used in this thesis. A method to attain cross section details using scanning electron microscopy was introduced. The operation modes of a typical atomic force microscope and how topographic details of a given sample is captured were discussed. A contact method of measuring electrical resistivity of thin films using the four-point probe was introduced. We also described how the Wiedemann-Franz law can be used to convert measured electrical conductivity to convert thermal conductivity and how the Cox-Strack method can be used to extract electrical contact resistance. However, this method is not suitable to determine thermal conductivity as the conversion process is limited by the applicability of the Wiedemann-Franz law. A method to measure the surface energy of a sample surface, and the concept of thermodynamic work of adhesion, were introduced. This will become important in later chapters when dealing with solid-liquid interfaces. Finally, a non-contact method for measuring thermal conductivity and volumetric heat capacity of embedded thin films, and

thermal boundary conductance across interfaces, were introduced. A second fluorescence microscope was setup opposite to the frequency-domain thermoreflectance optics for assisting the investigation of thermal transport involving fluids. Its significance will be discussed in Chapter 5. The key experimental results in subsequent chapters will rely on the methods discussed in this chapter.

## **Chapter 4.**

# **Impact of thermal properties on thermoelectric performance**

### **4.1 Introduction**

Thermoelectric materials are a class of materials that allow the conversion between thermal energy and electrical energy through charge and heat transport [129]. When an electric current is passed through a thermoelectric material it can act as a solid-state heat pump absorbing heat at one contact and depositing it at another. In this configuration it is known as a thermoelectric cooler (TEC). Conversely, thermoelectric materials can be used to generate electrical power when exposed to a temperature gradient, where they are known as thermoelectric generators (TEG). The thermoelectric effect may appear as a single effect but is in fact comprised of three unique phenomena; they are the Seebeck effect, the Peltier effect, and the Thomson effect. The Seebeck effect was the first of the three effects discovered by Alessandro Volta in 1794. The history of thermoelectricity is well documented in the literature [130].

Bulk thermoelectric coolers are commercially available and consist of many repeating pairs of n- and p-type semiconductors designed to be electrically in series and thermally in parallel. These scale of materials in these devices is usually at the millimetre to centimetre scale. Recently, there has been interest in miniaturising these thermoelectric heat pumps for use in integrated microelectronics and photonics. The current interest in thin film thermoelectric coolers has been spurred on partly by steady progress in improving thermoelectric material performance in recent years, and by the rapid growth in power densities and more integrated designs of modern photonic and electronic devices over the



past decade [32]. More recently, microscale TECs ( $\mu$ TECs) have gained traction for their fast time response and ability to handle high heat flux [35]. An additional benefit is that  $\mu$ TECs can be fabricated using complementary metal oxide semiconductor compatible processes [131].

Currently there is a huge emphasis in using low dimensional thermoelectric materials in handling hotspots for state-of-the-art photonic devices [132]. With  $\mu$ TEC's response time scaling with their critical dimension, it is important to accurately determine the performance of such devices. The thermoelectric performance of thermoelectric films is determined by a dimensionless number known as the thermoelectric figure of merit,  $ZT$ , which is given by [133]

$$ZT = \frac{S^2 \sigma_c}{\kappa} T, \quad (4.1)$$

where  $S$  is the Seebeck coefficient,  $\sigma_c$  is the electrical conductivity,  $\kappa$  is the thermal conductivity, and  $T$  is the local temperature. In recent years, magnetron sputtering [134], pulsed laser deposition [135], and metalorganic chemical vapour deposition [136] have all been used to produce thermoelectric films. Depending on thickness and deposition technique used, it is common that a film's electrical and thermal properties may vary significantly when comparing to bulk. This means that the  $ZT$  of thermoelectric films could vary wildly based of these factors. More importantly, a relatively small fraction of published works measured all the key parameters and determined  $ZT$  value for the electrodeposited thermoelectric material presented (see Table 4.1). Several used the definition of thermal diffusivity to calculate the lattice thermal conductivity via the volumetric heat capacity. Such a method of obtaining thermal conductivity typically reports lower than actual values, which inflates the  $ZT$  value as seen in literature [137], [138]. The sparsity of literature works

physically measuring thermal conductivities is concerning as Eq. (4.1) would suggest that  $\kappa$  has a significant implication to the thermoelectric material's performance. Further investigation into the literature mentioned in Table 4.1 revealed that little to no error analysis were performed when reporting measured electrodeposited thermoelectric thermal conductivity.

Table 4.1. Thermoelectric characterisation in *Electrochimica Acta* (2000-2020), where 36 data sets were collected by Corbett [139].

Thermoelectric parameter	$S$	$\sigma_c$	$\kappa$	$T$	$ZT$
% of papers measured	50	38	14.7	38	11.7

In this chapter, we present thermal measurements with two-sigma (95%) confidence intervals and thermal performance result of a prototype thermoelectric material fabricated by the Advanced Energy Materials group in the Tyndall Institute, University College Cork [140].

## 4.2 Materials

Figure 4.1(a) and (b) shows the cross section of the  $\text{Bi}_2\text{Te}_3$  based thermoelectric test device structure and the device itself, respectively. This is a Cox-Strack design [86] which is typically used for device characterisation purposes and is not a common design for a TEC device. The structure started with a 100 nm Au layer on a Si wafer with 1  $\mu\text{m}$   $\text{SiO}_2$ , which acted as working electrode for electrodeposition of the n-type  $\text{Bi}_2\text{Te}_3$ . The  $\text{Bi}_2\text{Te}_3$  film was synthesized using an electroplating technique. Complete details of the of the synthesis and reasoning for the n-type doping can be found elsewhere [140]. Within the circular cap region, a layer of tungsten (W), and titanium (Ti), is present, where the thin Ti layer acts as an

adhesion layer to better bond with the  $\text{Bi}_2\text{Te}_3$  layer. The purpose of the W layer is to act as a diffusion barrier layer to inhibit diffusion of Au atoms from the contact layer into the  $\text{Bi}_2\text{Te}_3$  layer. The top Au contact layer was deposited using the Ferrotec Temescal FC-2000 electron beam evaporation system. The top Au layer is 200 nm thick for better electrical probing, minimizing potential damaging of the active region of the device, and undesired heating from probe contact resistance and thermal bridging, which could all increase measurement errors. Figure 4.1(c) shows that the SiN layer does not maintain the 300 nm thickness as it approaches the cap layer. Therefore, the insulating effect around the W cap layer may be compromised to some degree. The thickness and its uncertainty from Figure 4.1(d) was used to perform FDTR fittings and uncertainty analysis. Note that cross sectioning was performed after all the measurements were completed.

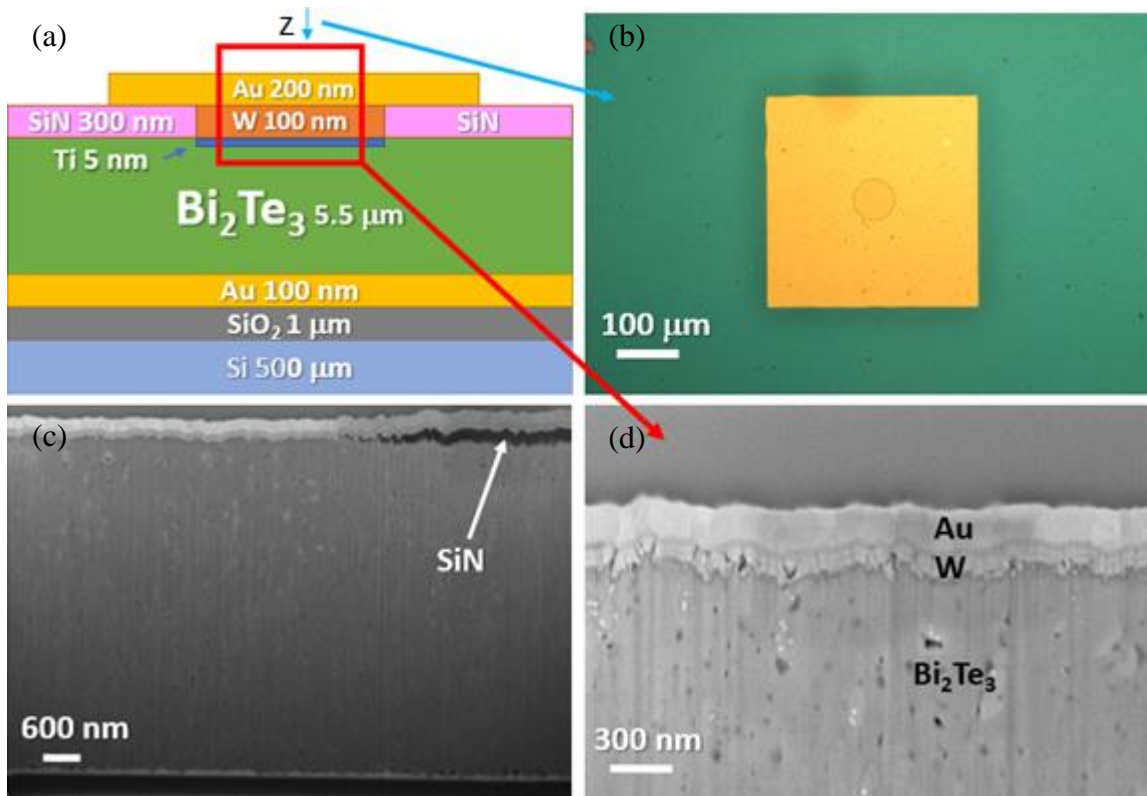


Figure 4.1: (a) Schematic cross section of single thermoelectric device structure. (b) Plan view image of a single 87  $\mu\text{m}$  square diameter pad. (c) A cross section SEM image about the 20  $\mu\text{m}$  circular pad. (d) A cross section SEM image about the centre of the 20  $\mu\text{m}$  circular pad with higher magnification compared to (c) a cross-section of the metal interfaces.

### 4.3 Results and discussion

The 200 nm Au transducer layer is significantly thicker than what is typically used in FDTR measurements. This makes a portion of the higher frequency range of the FDTR frequency sweep unusable and reduces the sensitivity to the parameters to the layer of interest due the thermal penetration depth as described in Section 3.6.4. Figure 4.2 shows the measured phase lag data and fit for the Bi<sub>2</sub>Te<sub>3</sub> based thermoelectric test device using the FDTR system and analysis methods as described in Section 3.6.1, and in Section 3.6.1 to 3.6.4, respectively. The noise in the higher frequency regime could be due to excessive heat spreading of the thick Au transducer. The Bi<sub>2</sub>Te<sub>3</sub> film cross-plane thermal conductivity and volumetric heat capacity, and the effective TBC between Bi<sub>2</sub>Te<sub>3</sub> and W were measured. The measured

effective TBC is described by considering the thermal resistance model where we allow the Ti layer to act as part of the effective thermal boundary resistance, such that we get

$$G_{\text{Bi}_2\text{Te}_3-\text{W}}^{-1} = G_{\text{Bi}_2\text{Te}_3-\text{Ti}}^{-1} + \frac{d_{\text{t,Ti}}}{\kappa_{\text{Ti}}} + G_{\text{Ti}-\text{W}}^{-1}. \quad (4.2)$$

where  $d_{\text{t}}/\kappa$  is the ratio of layer thickness to material thermal conductivity and it represents the thermal resistance of the layer per unit area.

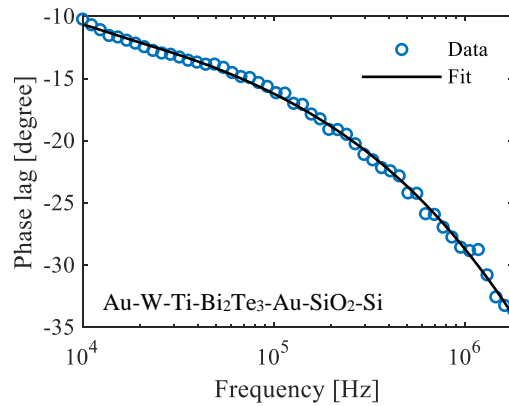


Figure 4.2: Measured phase lag data and fit using Eq. (3.45) for the  $\text{Bi}_2\text{Te}_3$  based thermoelectric test device with 200 nm thick Au transducer on top.

#### 4.3.1 Measurement of electrodeposited $\text{Bi}_2\text{Te}_3$ film thermal conductivity

Figure 4.3(a) shows a thermal conductivity distribution and fit of the  $\text{Bi}_2\text{Te}_3$  film by using a Monte Carlo method as described in Section 3.6.6 on the measured FDTR data. The measured thermal conductivity value of  $0.85 \pm 0.06 \text{ W m}^{-1} \text{ K}^{-1}$  agrees with literature values which range from  $0.7 \text{ W m}^{-1} \text{ K}^{-1}$  to  $1.48 \text{ W m}^{-1} \text{ K}^{-1}$  [131], [141]–[143].

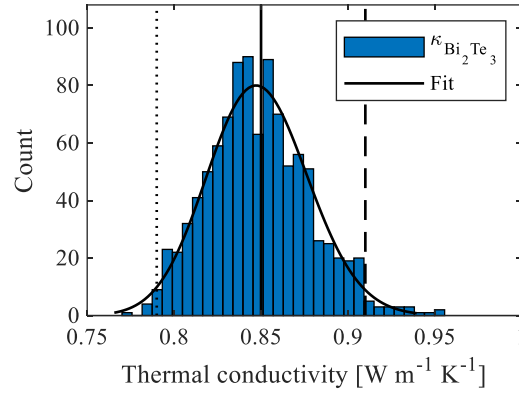


Figure 4.3: Thermal conductivity distribution and fit (using `lognfit` Matlab built-in function) of the measured  $\text{Bi}_2\text{Te}_3$  film, where solid lines represent mean, while dotted and dashed lines represent the lower and upper confidence intervals at 95%, respectively.

Figure 4.4(a) shows the sensitivity in terms of the phase difference as described in Section 3.6.5 due to a  $\pm 10\%$  shift in the thermal conductivity and volumetric heat capacity of the  $\text{Bi}_2\text{Te}_3$  film over the measured frequency range. The sensitivity is relatively poor compared to the typical baseline Au-SiO<sub>2</sub> sample as seen in Figure 3.14(a), especially the noise at around 10 MHz. Figure 4.4(b) shows that the thermal conductivity and volumetric heat capacity are highly distinguishable at around 2.2 kHz. Using Eq. (3.46), at 2.2 kHz modulation frequency, the thermal diffusion length in this  $\text{Bi}_2\text{Te}_3$  film is calculated to be 5.9  $\mu\text{m}$  with  $\alpha_d = 2.42 \times 10^{-7} \text{ m}^2 \text{ s}^{-1}$ . Although the phase lag profile can be sensitive to the individual thermal properties, much of the effect from such a feature is often cancelled out in the resulting phase lag profile when considering the product of these properties.

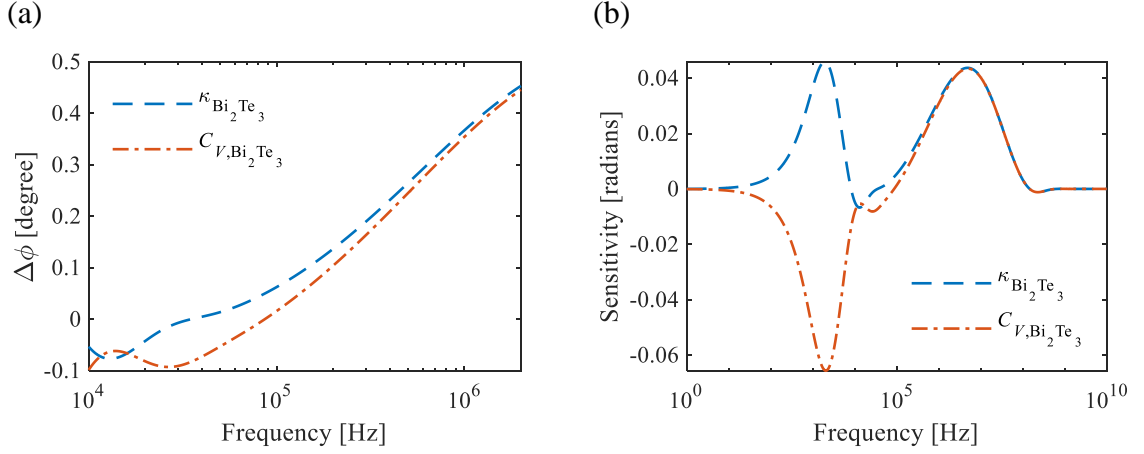


Figure 4.4: (a) A phase difference plot, where the phase difference is calculated by subtracting the phase lag with  $-10\%$   $\text{Bi}_2\text{Te}_3$  thermal conductivity and volumetric heat capacity, respectively, while holding other parameters constant. (b) Theoretical sensitivity to the thermal conductivity and volumetric heat capacity calculated using Eq. (3.47) based on the measured values for the thermoelectric test device.

#### 4.3.2 Performance of electrodeposited $\text{Bi}_2\text{Te}_3$ thermoelectric device

In this section, we gathered the measured parameters and calculated  $ZT$  of the thermoelectric device described in Section 4.2. The Seebeck coefficient, thermal conductivity, electrical conductivity, and heat flux were measured in that order. This arrangement considers the effect of each parameter measurement has on the heat flow capability in the system along with practicalities, such as sample degradation and damage due to electrical/laser testing. The electrical characterisation is carried out first to ensure the functionality of the device. Figure 4.5(b) shows the measured total resistance  $\mathcal{R}_{\text{tot}}$  with different pad diameter  $d_d$  and fit of the data using the Eq. (3.7), and we determined the electrical conductivity of the  $\text{Bi}_2\text{Te}_3$  film to be  $\rho_{r,\parallel} = 5.2 \times 10^4 \pm 0.32 \times 10^4 \text{ S m}^{-1}$  at room temperature [140]. Figure 4.5(c) shows how contact resistance influences the total resistance as a function of  $1/d_d^2$ . For thin films, if the electrical contact resistance is high, it can negate the cooling effect completely. In order to attain net cooling, the contact resistance must at least be  $< 10^{-11} \text{ } \Omega \text{ m}^{-2}$  [140]. Direct measurement of net cooling confirms that these films achieve this condition. The Seebeck coefficient was measured to be  $S = -121 \pm 6 \text{ } \mu\text{V K}^{-1}$  using a custom built CCD-

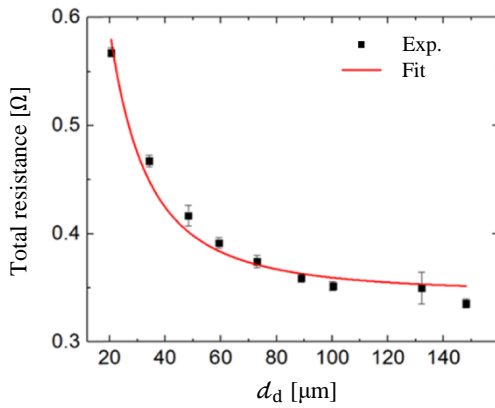
TR system [140]. The CCD-TR technique is beyond the scope of this thesis, and in-depth details of this technique used for thermoelectric characterisation can be found elsewhere [139]. Using the same CCD-TR system, 100 mA was applied as electrically induced heating and temperature maps were recorded. The finite element method (FEM) was used to predict the surface temperature. The device was demonstrated to achieve a maximum cooling  $\Delta T$  of  $-4.4$  K under zero load [140]. Now that all the parameters are gathered, using Eq. (4.1) we get  $ZT = 0.26 \pm 0.04$ . Although  $ZT$  values between 0.05 and 0.45 for n-type  $\text{Bi}_2\text{Te}_3$  has been seen reported [141], [144], [145], only  $ZT$  values up to 0.1 included direct measurement of the cross-plane thermal conductivity. This is the highest reported  $ZT$  for electrodeposited  $\text{Bi}_2\text{Te}_3$  in which all the relevant parameters were measured, to our knowledge.



(a)



(b)



(c)

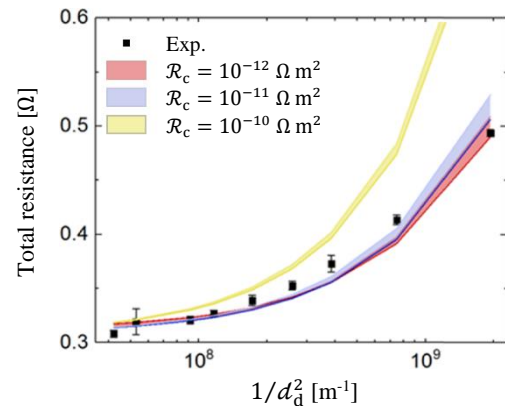


Figure 4.5: Electrical conductivity and contact resistance measurements [140]. (a) Plan view optical images of the test pads. (b) Measured four-point resistance as a function of pad diameter and fit using Eq. (3.7). (c) Total resistance as a function of reciprocal pad diameter squared and the effect of contact resistance on total resistance.

### 4.3.3 Phonon scattering in electrodeposited $\text{Bi}_2\text{Te}_3$ film

Although volumetric heat capacity is not required to calculate  $ZT$ , measuring it can give us some information about the mean free path of phonons in the  $\text{Bi}_2\text{Te}_3$  film. Since we are dealing with transport in the diffusive regime and not having details of the dispersion relation of this  $\text{Bi}_2\text{Te}_3$  film, we used kinetic theory [49] by considering a gas of phonon particles as illustrated in Figure 2.1(d) and related the measured thermal conductivity and volumetric heat capacity to the mean free path,  $\ell$ , by [146]

$$\kappa = \frac{1}{3} C_V v_{g,ave} \ell. \quad (4.3)$$

Using Eq. (4.3) with Bi<sub>2</sub>Te<sub>3</sub> average group velocity  $v_{g,ave} = 2000 \text{ m s}^{-1}$ , along with the measured thermal conductivity  $\kappa = 0.85 \text{ W m}^{-1} \text{ K}^{-1}$ , and volumetric heat capacity  $C_V = 1.9 \text{ MJ m}^{-3} \text{ K}^{-1}$ , the mean free path was calculated to be  $6.7 \text{ \AA}$ . This result is comparable to the mean free path obtained from a first principles approach [147], but is slightly lower than literature value of  $10 \text{ \AA}$  [148]. The lower values determined could be due to defects or/and because it is electrodeposited and not a perfect single crystal. This result is essentially the effective phonon mean free path,  $\ell_{eff}$ , and can be decomposed into Umklapp scattering, defect/impurity scattering, and boundary/surface scattering as [149]

$$\ell_{eff}^{-1}(\omega, T) = \ell_{Umklapp}^{-1}(\omega, T) + \ell_{defect}^{-1}(\omega) + \ell_{boundary}^{-1}, \quad (4.4)$$

which satisfies the physics of 3-phonon interactions (phonon-phonon). It is worth noting that no normal scattering processes are present in Eq. (4.4) as both momentum and energy are conserved (i.e.,  $\hbar\mathbf{k}_3 = \hbar\mathbf{k}_1 + \hbar\mathbf{k}_2$ , and  $\hbar\omega_3 = \hbar\omega_1 + \hbar\omega_2$ ), therefore there is no impedance to heat flow. Since the film thickness is much greater than the mean free path, the film thermal conductivity should not be meaningfully affected by surface scattering at the boundary. However, surface scattering is still possible when  $d_t > \ell$ , as the mean free path is just the average phonon travel distance between collisions. More realistically, imperfections and impurities of the materials are most likely to be the main contributors to why the values deviate from bulk. Such as, any imperfections and defects present in the thermoelectric layer would affect its thermal conductivity and thus the thermoelectric figure of merit.

#### 4.3.4 Thermal boundary conductance (TBC) across Bi<sub>2</sub>Te<sub>3</sub>-W interface

In this section, we used the DMM as described in Section 2.3.2 to gain some insight on how the TBC of the measured effective Bi<sub>2</sub>Te<sub>3</sub>-W interface would behave over a wide range of temperatures. Assuming complete elastic and diffusive scattering, we used Eq. (2.21) and (2.23) with physical acoustic values in Table 4.2 and calculated the TBC as a function of temperature as shown in Figure 4.6. The cut-off frequencies in the integral of Eq. (2.21) with Eq. (2.23) is calculated by [49]

$$\omega_{\max,1,j} = (6\pi^2 \rho_{N,1})^{1/3} v_{1,j}, \quad (4.5)$$

where  $\rho_N$  is the number density. The number density is calculated by  $\rho_N = \rho N_A / M_u$ , where  $N_A$  is the Avogadro constant, and  $M_u$  is the molar mass which is the mass of a substance per number of moles of the substance. The predicted TBC at room temperature is just within the lower bound of the measured TBC. However, it is not uncommon to see that DMM under-predicts or over-predicts the TBC for many interfaces across dissimilar materials depending on the Debye temperatures [150]. Here we refrain from using DMM to present more TBC predictions between Bi<sub>2</sub>Te<sub>3</sub> and other materials. Although many improvements have been made to enhance the predictability of DMM as mentioned in Section 2.3.2, for more accurate predictions and rigorous understanding of interfacial thermal transport across solid-solid interfaces, first-principles approaches (i.e., Boltzmann transport equation or atomistic Green's function) are available and should be used instead [151]–[153]. Nevertheless, the crude DMM predictions suggest that the TBC should not be greatly affected within the TEC device's operation temperature range.

Table 4.2: Acoustic and thermodynamic parameters used in DMM calculations. The acoustic velocities of  $\text{Bi}_2\text{Te}_3$  are taken from literature [154]. The remaining parameters are taken from the CRC Handbook of Chemistry and Physics [155].

	$\rho$ [ $\text{kg m}^{-3}$ ]	$M_u$ [ $\text{g mol}^{-1}$ ]	$v_L$ [ $\text{m s}^{-1}$ ]	$v_T$ [ $\text{m s}^{-1}$ ]
W	19250	183.84	5220	2890
$\text{Bi}_2\text{Te}_3$	7740	800.76	2400	1800

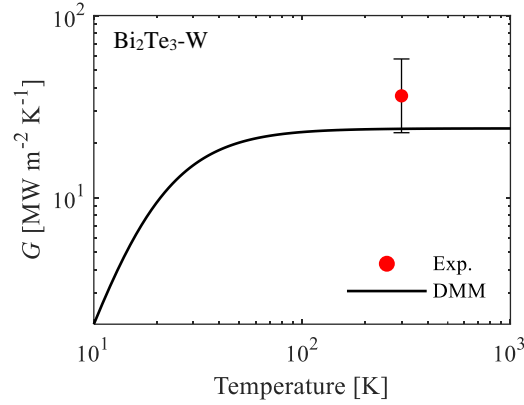


Figure 4.6: Predicted TBC across  $\text{Bi}_2\text{Te}_3$ -W interface as a function of temperature using Eq. (2.21) and (2.23) with acoustic values in Table 4.2, and experimental measurement of the TBC at room temperature using FDTR.

## 4.4 Conclusions

In this chapter we introduced the concept of thermoelectric figure of merit, which is used to determine the performance of thermoelectric devices. We introduced the electrical and thermal parameters involved in calculating the figure of merit. We discovered that several thermoelectric figures of merit reported for  $\text{Bi}_2\text{Te}_3$  did not involve measurements of thermal conductivity and little to no error analysis was performed for those that were measured. We appropriately measured the cross-plane thermal conductivity of an electrodeposited n-type  $\text{Bi}_2\text{Te}_3$  film in the thermoelectric device and determined the 95% confidence intervals using a conservative but robust Monte Carlo method. We reported the highest thermoelectric figure

of merit to our knowledge with  $ZT = 0.26 \pm 0.04$  for electrodeposited n-type  $\text{Bi}_2\text{Te}_3$  film where all electrical and thermal parameters are measured experimentally.

To observe if the measured thermal conductivity of the  $\text{Bi}_2\text{Te}_3$  film is subjected to a size effect, we measured the  $\text{Bi}_2\text{Te}_3$  volumetric heat capacity and determined the phonon mean free path through kinetic theory. The results indicate that no size effect should be in play, as the film thickness is much greater than the mean free path. Although the mean free path is comparable to literature, the slightly shorter mean free path could be due to imperfections, defects, or/and the fabrication technique.

Finally, we used a basic DMM model to predict the TBC across  $\text{Bi}_2\text{Te}_3$ -W interface as a function of temperature. The measurement of the effective TBC across  $\text{Bi}_2\text{Te}_3$ -W interface is within the lower bound of the 95% confidence interval at room temperature. We concluded that the TBC involving  $\text{Bi}_2\text{Te}_3$  do not fluctuate enough to impact the overall performance of the thermoelectric device under operation temperatures.

Part of the work presented in this chapter has been published in ACS Applied Materials & Interfaces [III][140].

## Chapter 5.

# Effect of wettability on interfacial thermal transport

## 5.1 Introduction

In Chapter 2 and 3, the theories and methodologies were presented for solid-state systems, respectively. Similarly, Chapter 4 focused on characterisation of a solid-state cooling device. This chapter will detail the theories for thermal transport across solid-liquid interfaces, and methodologies centring around the frequency-domain thermoreflectance (FDTR) technique to better understand the effect that wettability has on interfacial thermal transport.

The need for well-controlled interface thermal transport characteristics has led to several investigations focused on improving thermal conductance at solid-liquid interfaces [13], [156]–[159]. The use of self-assembled monolayers (SAMs) to tailor the TBC through modification of the van der Waals interaction strength at solid-liquid interfaces has been demonstrated. Using time-domain thermoreflectance (TDTR), Harikrishna *et al.* showed that thermal boundary conductance (TBC),  $G$ , is proportional to the thermodynamic work of adhesion between functionalised Au and water for a series of five alkane-thiol monolayers at the Au-water interface [157]. They were able to achieve TBC across Au-water interfaces up to  $190 \text{ MW m}^{-2} \text{ K}^{-1}$  with hydrophilic 11-mercapto-undecanoic acid (COOH) surface treatment. They also determined uncertainty values of  $\pm 30 \text{ MW m}^{-2} \text{ K}^{-1}$  by using a range of TBC values that could fit the experimental data. This is a common method in quantifying the margin of error in TBC. However, this practice assumes that the measuring technique is sensitive to TBC, which is not always the case especially when dealing with the relatively low effusivity of dielectric fluids for thermal applications (i.e., Novec, Galden, Genetron, etc.) where heat is not carried by electrons. For this reason, we will introduce and use

dynamic confidence intervals from distributions obtained by the Monte Carlo method described in Section 3.6.6, to determine the lower and upper bounds of TBC involving SAMs.

The first experimental part of this chapter is to gain confidence of the custom FDTR system in measuring solid-liquid interfaces. To do this we measured the TBC of Au-water interfaces with and without SAMs. We accompanied the experimental data with analytical predictions. We then study the effect of wettability on TBC across Au-dielectric fluid interfaces, we also probed the accuracy of a modified analytical model in predicting such systems.

## 5.2 Materials and methods

### 5.2.1 Sample preparation and fabrication

The key materials used in the first experimental section are 1-Decanethiol (96%)  $\text{CH}_3(\text{CH}_2)_9\text{SH}$  and 1H,1H,2H,2H-Perfluorodecanethiol (97%)  $\text{CF}_3(\text{CF}_2)_7\text{CH}_2\text{CH}_2\text{SH}$ , purchased from Sigma-Aldrich, and may be worth noting that both are  $\text{C}_{10}$  SAM molecules for comparison purposes. These chemicals were chosen as they have not been seen used in investigating the effect of wettability on interfacial thermal transport and are also relatively safe compared to other chemicals used in literature [157]. The simple structure diagrams of these two thiol molecules are shown in Figure 5.1. High performance liquid chromatography grade deionised water ( $\rho_r = 18.2 \text{ M}\Omega \text{ cm}$ ), diiodomethane ( $\text{CH}_2\text{I}_2$ ) (purity  $\geq 99\%$ ), isopropyl alcohol (suitable for HPLC, purity 99.9%), and pure ethanol ( $\text{C}_2\text{H}_6\text{O}$ ) (anhydrous, purity  $\geq 99.5\%$ ), were also purchased from Sigma-Aldrich for cleaning the  $\text{SiO}_2$  substrate prior to Au deposition, contact angle measurements and synthesis, respectively.

Thiol chemistry is implemented on an Au-coated SiO<sub>2</sub> substrate which the Au layer doubles as the thermoreflectance transducer for the thermal measurements, where the fabrication process steps are as shown in Figure 5.2. Alkylated thiols can be adhered to the Au surface through a chemical self-assembly process. A single layer of a SAM is composed of three main parts: the active thiol head group, the carbon back bone, and the functionalised end group. Chemisorption is driven by the soft sulphur ligand having favourable interaction with the Au atoms indicated by the hard and soft acids and bases theory [160], [161]. The mechanism of this type of adhesion to Au is still unclear [162], however several mechanisms have been proposed by Abraham Ulman [163]–[165].

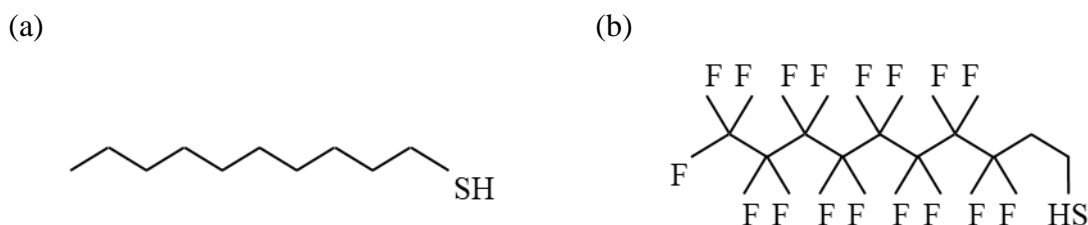


Figure 5.1: Simple structure diagrams of the investigated thiolated SAMs: (a) 1-Decanethiol (1DT). (b) 1H,1H,2H,2H-Perfluorodecanethiol (PFDT). Adapted from CRC Handbook of Chemistry and Physics [155]

Firstly, the removal of the H atom from the thiol active group results in the generation of H<sub>2</sub>. Additionally, these H atoms are generated from the metal hydrides on the surface of the metal at surfaces where the SAM have not been bound. Finally, the side products that can generate from the reaction may also produce hydrogen peroxide and water. Ulman thermodynamically calculated the overall free energy of the exothermic adsorption process to be  $-5 \text{ kcal mol}^{-1}$ , identifying the reaction as spontaneous at room temperature. Thiolated SAMs can be easily formed on an Au surface via self-assembly from solution [166].



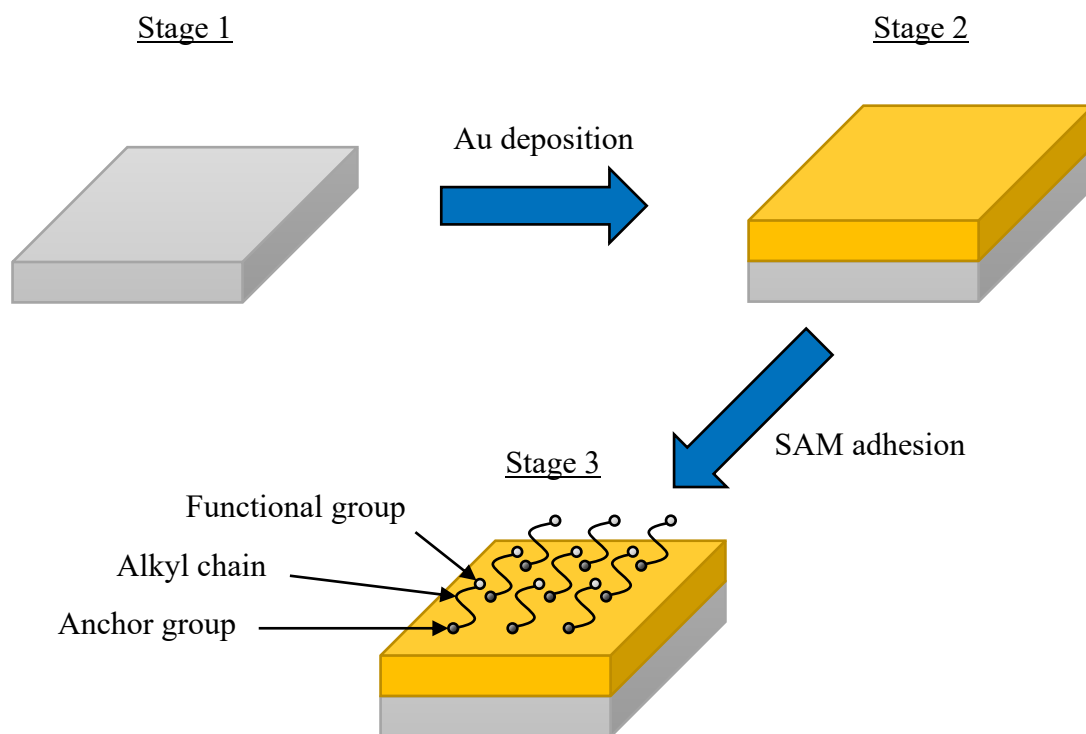


Figure 5.2: Process steps for adhesion of SAM to Au surface.

The SiO<sub>2</sub> substrate was cleaved into 2.5 × 2.5 cm pieces and degreased by sonication using isopropyl alcohol for 20 minutes. All sample surfaces were oxygen plasma treated to remove organic contamination using the Diener PICO barrel asher before Au deposition. Thin Ti adhesion layer (< 5 nm) followed by 100 nm of Au were deposited on to the substrates using the Temescal FC-2000 electron beam evaporation system as described in Section 3.6.3. After Au deposition, the substrates were firstly washed in ethanol with some substrates followed by a vertical immersion into a 5 mmol thiol ethanolic solution (1DT or PFDT) that was left approximately 24 hours at room temperature. Samples were then sonicated in ethanol for 10 minutes to terminate self-assembly followed by N<sub>2</sub> purge, which vaporises any remaining ethanol residue. Samples were stored in desiccators to minimise contamination prior to atomic force microscopy (AFM), contact angle goniometry (CAG), and FDTR measurements.

The typical liquid cell is assembled by creating a cavity using a nitrile O-ring between the sample and a quartz substrate as window, where the working fluid is injected into the cell using a pipette; it is then secured onto the sample stage for FDTR measurement as shown in Figure 5.3.

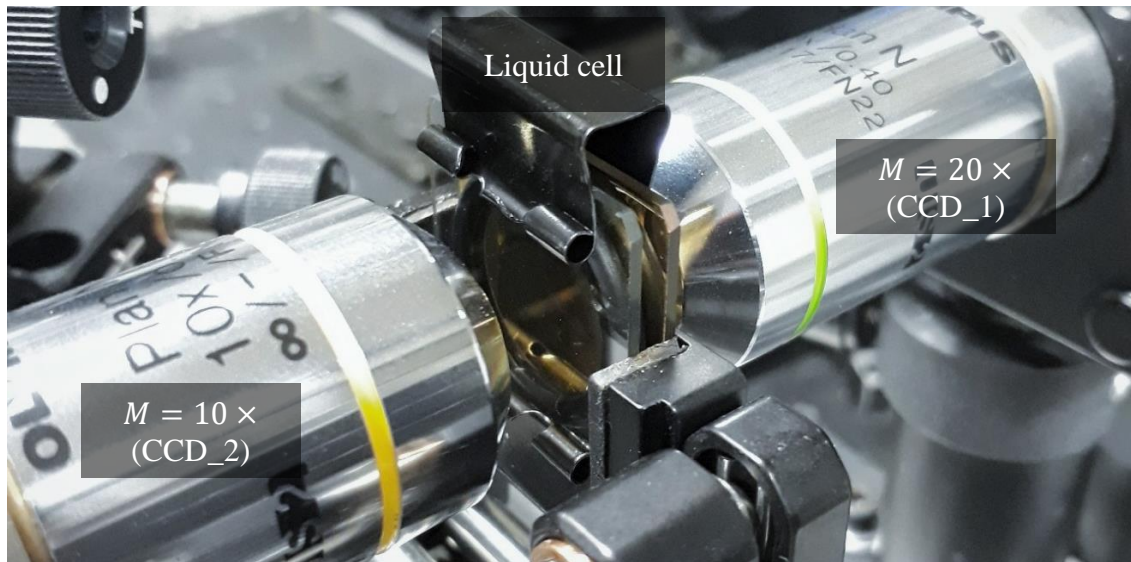


Figure 5.3: Image of the liquid cell installed in the beam line of the custom FDTR setup.

The key materials used in the second experimental section are identical to the first experimental section apart from the working fluid. In this study, we will be using  $C_2H_6O$  instead of deionised water.

### 5.2.2 Bidirectional heat transfer model for thermorefectance techniques

Recalling the transfer matrix equation in Section 3.6.4, an approximation of unidirectional heat flow may be appropriate by using Eq. (3.35) when the thermal conductivity of the medium on top of the first layer is approaching  $0 \text{ W m}^{-1} \text{ K}^{-1}$ . Since this liquid cell structure has a layer of  $SiO_2$  substrate in contact with the top surface of the first layer (i.e., transducer layer), it is necessary to consider bidirectional heat flow for any measurements involving such stacking structure where the top surface of the transducer is not in contact with the likes

of air as shown in Figure 5.4. In the bidirectional heat transfer model, the temperature of the transducer surface at the transducer-substrate interface is given by [117]

$$T = \mathcal{G}(\kappa_H, \omega)q = \left( \frac{-D_1 D_2}{D_1 C_2 + D_2 C_1} \right) q. \quad (5.1)$$

Here,  $C_1$ ,  $C_2$ ,  $D_1$ , and  $D_2$  are elements in matrix  $\mathbf{M}_1$  and  $\mathbf{M}_2$  of layer 1 and 2, respectively in Eq. (3.34). Substituting Eq. (3.35) with (5.1) gives the final frequency response

$$H(\omega) = \frac{P_{\text{pu,abs}}}{2\pi} \int_0^\infty \left( \frac{-D_1 D_2}{D_1 C_2 + D_2 C_1} \right) e^{-\frac{\kappa_H^2 (\omega_{\text{pu}}^2 + \omega_{\text{pr}}^2)}{8}} \kappa_H d \kappa_H. \quad (5.2)$$

We used Eq. (5.2) to extract thermal properties for all solid-liquid systems.

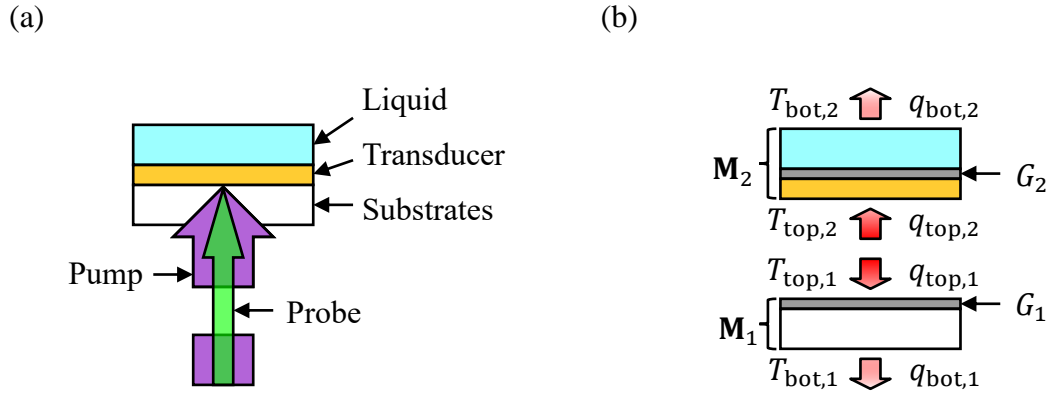


Figure 5.4: Simple schematic of (a) a typical liquid cell structure, and (b) the bidirectional heat flow problem associated to the liquid cell structure separated into simpler and smaller multiple unidirectional heat flow problems. For clarity, a layer of  $\text{SiO}_2$  is present on top of the liquid layer to encapsulate the working fluid and to observe the solid-liquid interface using CCD 2 through a second fluorescence microscope setup (see Figure 3.9). The  $\text{SiO}_2$  can be neglected as the liquid layer is several microns thick and can be considered semi-infinite in the heat diffusion model.

### 5.2.3 AMM for solid-liquid interfaces

Although the first intensive study in interfacial thermal properties was done at a solid-liquid interface, there has been much greater success in understanding the fundamentals of phonon transport across solid-solid interface compared to solid-liquid

interfaces. With advancements of computational capability, the use of the Green-Kubo formalism in molecular-dynamics (MD) simulations has become an integral part in studying thermal transport [167]. MD is a popular approach in studying interfaces as the formalism only involves Newton's equations of motion and interactions of particles through interatomic potential [168], [169], and does not require any understanding of the physics of heat transport. However, MD has its drawbacks of being relatively classical (i.e., lack of bonds forming/breaking, and limited ability in providing accurate details of chemical interactions at the interface).

As described in Section 2.3, the acoustic mismatch model (AMM) and the diffuse mismatch model (DMM) are commonly considered as the backbone in predicting TBC. More recently, frameworks based on the AMM and DMM were developed independently to predict TBC across solid-liquid interfaces [170], [171]. The basis of both frameworks is still primarily differentiated by their phonon scattering assumptions at the interface.

In this chapter, we will use the framework of AMM for two key reasons: The first reason being that the roughness of the samples has a root mean square (RMS) value smaller than 2.5 nm. For the purpose of comparing to the experimental results, AMM is more appropriate as diffuse scattering is unlikely since the incident phonons wavelengths contributing to heat transfer are generally going to be larger than the RMS roughness [172], [173]. The second reason is that an extension to AMM was developed to account for the finite bonding strength between two media,  $K_{12}$ , at solid-liquid interfaces, however this feature is still lacking in DMM. The disordered nature of liquids makes it impossible to study at a more fundamental level, due to the lack of classical description of such system in terms of collective propagative excitations. We will use Frenkel's findings on solid-like behaviours

in fluids to deal with solid-liquid systems [174], [175], and the Lennard-Jones (LJ) potential to describe the van der Waals force interaction between two the media [58].

For dealing with solid-liquid systems, both the AMM and DMM can consider two motions on the liquid side: liquid diffusional motions below the Frenkel frequency,  $\omega_F$ , and phonon motions above the Frenkel frequency ( $\omega \geq \omega_F$ ) as shown in Figure 5.5. Following literature [170], [171], the Frenkel frequency can be approximated by taking the inverse of the temperature dependent liquid viscoelastic relaxation time,

$$\omega_F \simeq \frac{1}{\tau_\alpha(T)} = \frac{G_\infty(T)}{\eta(T)}, \quad (5.3)$$

where  $\tau_\alpha$  is the liquid viscoelastic relaxation time,  $G_\infty$  is the infinite-frequency shear modulus, and  $\eta$  is the shear viscosity. This means that for low-frequency ( $\omega < \omega_F$ ), only longitudinal acoustic waves can propagate in the liquid; while for high-frequency ( $\omega \geq \omega_F$ ), the liquid behaves like solid and may support both longitudinal and transverse acoustic waves. Using Frenkel's theory, the TBC from material of side 1 to material of side 2 (Eq. (2.16) with Eq. (2.17) and (2.18)) may be decomposed into:

$$G = G_0 + G_L + G_T, \quad (5.4)$$

with:

$$\begin{aligned}
G_0 &= \frac{1}{2} \int_0^{\omega_F} \int_0^{\theta_{c,1,L}} \mathcal{T}_0 v_{1,0}(\omega) \mathcal{D}_{1,0}(\omega) \hbar \omega \frac{\partial f_{\text{BE}}^0(\omega, T)}{\partial T} \cos \theta \sin \theta d\theta d\omega, \\
G_L &= \frac{1}{2} \int_{\omega_F}^{\omega_{\text{max}}} \int_0^{\theta_{c,1,L}} \mathcal{T}_L v_{1,L}(\omega) \mathcal{D}_{1,L}(\omega) \hbar \omega \frac{\partial f_{\text{BE}}^0(\omega, T)}{\partial T} \cos \theta \sin \theta d\theta d\omega, \quad (5.5) \\
G_T &= \frac{1}{2} \int_{\omega_F}^{\omega_{\text{max}}} \int_0^{\theta_{c,1,T}} \mathcal{T}_T v_{1,T}(\omega) \mathcal{D}_{1,T}(\omega) \hbar \omega \frac{\partial f_{\text{BE}}^0(\omega, T)}{\partial T} \cos \theta \sin \theta d\theta d\omega,
\end{aligned}$$

where  $\omega_{\text{max}}$  is the cut-off frequency,  $\theta_c$  is the critical angle,  $f_{\text{BE}}^0(\omega, T) = 1/(e^{\hbar\omega/k_B T} - 1)$  and is the Bose-Einstein equilibrium phonon distribution,  $k_B$  is the Boltzmann constant, and  $T$  is the local temperature. The subscripts 0, L, and T refer to low-frequency longitudinal, high-frequency longitudinal, and high-frequency transverse, respectively. Similarly, the phonon transmission probability (Eq. (2.20)) may also be decomposed into:

$$\begin{aligned}
\mathcal{T}_0(\theta) &= \frac{4\rho_1 v_{1,L} \rho_2 v_{2,0} \cos \theta_1 \cos \theta_2}{(\rho_1 v_{1,L} \cos \theta_1 + \rho_2 v_{2,0} \cos \theta_2)^2}, \\
\mathcal{T}_L(\theta) &= \frac{4\rho_1 v_{1,L} \rho_2 v_{2,L} \cos \theta_1 \cos \theta_2}{(\rho_1 v_{1,L} \cos \theta_1 + \rho_2 v_{2,L} \cos \theta_2)^2}, \quad (5.6) \\
\mathcal{T}_T(\theta) &= \frac{4\rho_1 v_{1,T} \rho_2 v_{2,T} \cos \theta_1 \cos \theta_2}{(\rho_1 v_{1,T} \cos \theta_1 + \rho_2 v_{2,T} \cos \theta_2)^2},
\end{aligned}$$

where  $\rho_i$  is the density of material  $i$ , and  $v_{i,j}$  is the acoustic velocity of material  $i$  for polarization  $j$  (i.e., low-frequency longitudinal, 0, or high-frequency longitudinal, L, or high-frequency transverse, T).  $\theta_1$  and  $\theta_2$  are the incident and refraction angles, respectively, and are related to  $v_i$  in material  $i$  through and equivalent of Snell's law.

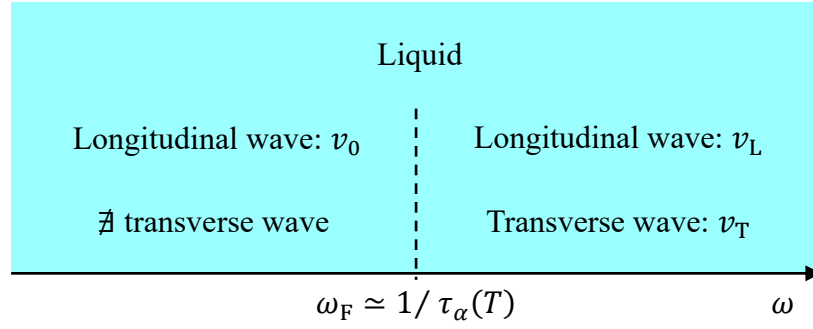


Figure 5.5: Schematic illustration of the different set of acoustic propagation in frequency regime below and above Frenkel frequency for a liquid, where the longitudinal and transverse acoustic velocities in their respective frequency regime can be identified by the variable subscript. Adapted from literature [170].

The van der Waals force interaction between two media may be described by the two media connected by weak springs [58]. Michael Schoenberg [176] derived the angle,  $\theta$ , and frequency,  $\omega$ , dependent phonon transmission,  $\mathcal{T}$ , of acoustic propagation from side 1 to 2 of a solid-solid system shown in Figure 5.6 as

$$\mathcal{T}(\theta, \omega) = \frac{4Z_1Z_2 \cos \theta_1 \cos \theta_2}{(Z_1 \cos \theta_1 + Z_2 \cos \theta_2)^2 + \left(\frac{\omega}{K_{12}}\right)^2 (Z_1Z_2 \cos \theta_1 \cos \theta_2)^2}, \quad (5.7)$$

where  $Z = \rho v$  and is the acoustic impedance. Notice that for strong interfacial bond (i.e.,  $K_{12} \rightarrow \infty$ ), Eq. (5.7) collapses to Eq. (2.20). Similarly, for long wavelengths (i.e.,  $\omega \rightarrow 0$ ), Eq. (5.7) also collapses to Eq. (2.20), as the longer the acoustic propagation wavelengths are less likely going to experience imperfections at the interface [58].

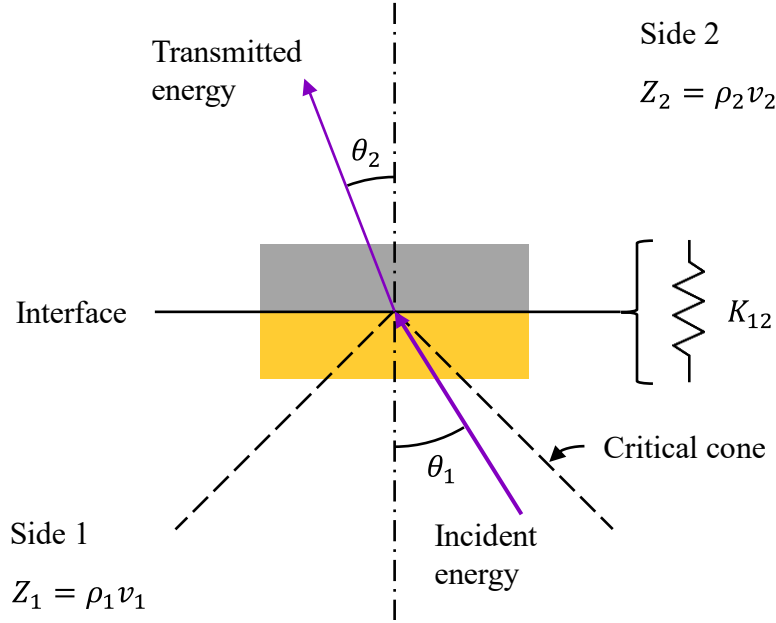


Figure 5.6: Schematic illustration of energy transmission across solid-solid interface.

Combining the definition for Eq. (5.6), and (5.7), we get

$$\mathcal{T}_0(\theta, \omega) = \frac{4Z_{1,L}Z_{2,0} \cos \theta_1 \cos \theta_2}{(Z_{1,L} \cos \theta_1 + Z_{2,0} \cos \theta_2)^2 + \left(\frac{\omega}{K_{12}}\right)^2 (Z_{1,L}Z_{2,0} \cos \theta_1 \cos \theta_2)^2},$$

$$\mathcal{T}_L(\theta, \omega) = \frac{4Z_{1,L}Z_{2,L} \cos \theta_1 \cos \theta_2}{(Z_{1,L} \cos \theta_1 + Z_{2,L} \cos \theta_2)^2 + \left(\frac{\omega}{K_{12}}\right)^2 (Z_{1,L}Z_{2,L} \cos \theta_1 \cos \theta_2)^2},$$

$$\mathcal{T}_T(\theta, \omega) = \frac{4Z_{1,T}Z_{2,T} \cos \theta_1 \cos \theta_2}{(Z_{1,T} \cos \theta_1 + Z_{2,T} \cos \theta_2)^2 + \left(\frac{\omega}{K_{12}}\right)^2 (Z_{1,T}Z_{2,T} \cos \theta_1 \cos \theta_2)^2}.$$

(5.8)

The interaction force between general solid-liquid systems is typically of van der Waals type and is commonly described by the LJ potential [170] (see Section 3.3.1 for description of the LJ potential). The bonding strength or spring stiffness per unit area between a pair of atoms is given by [58]



$$K_{12} = N_{\text{surf}} \left( \frac{\partial^2 U_{\text{LJ}}}{\partial r^2} \right)_{r=2^{1/6}\sigma} = \frac{72N_{\text{surf}}\varepsilon}{2^{1/3}\sigma^2}, \quad (5.9)$$

where  $N_{\text{surf}}$  is the number of surface atoms per unit area,  $r$  is the distance between the centre of the particles,  $\varepsilon$  is the depth of the potential well, and  $\sigma$  is the distance at  $U_{\text{LJ}}(r) = 0$ .

To understand the viscoelastic effects in the TBC of solid-water interfaces, Merabia *et al.* proposed the elastic, and inelastic frameworks for AMM [170]. Figure 5.7 illustrates the main difference between the two frameworks. In elastic phonon scattering events, there is no change in energy, while in inelastic phonon scattering events, there is some change in the resulting phonon energy. This means that transmitted heat flux is not limited by the difference of the population of allowable phonon states per wavevector of the two materials, as phonons on both sides of the interface can participate [55]. As a result, the inelastic framework greatly enhances the capability AMM in general. Merabia *et al.* [170] showed that the inelastic AMM is suitable in predicting TBC across very flat solid-liquid interfaces, and good agreement with experimental [13], [157] and molecular dynamics (MD) simulation [177], [178] results.

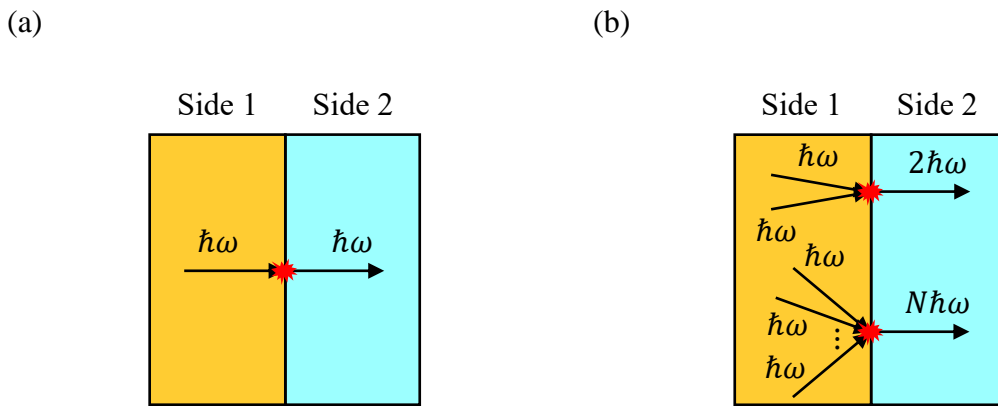


Figure 5.7: Simplified illustration of interfacial phonon processes: (a) 2-phonon scattering (i.e., elastic). (b)  $N$ -phonon scattering (i.e., inelastic).

Using the previous definitions, we predict the TBC across Au-liquid interfaces using the final TBC expression

$$\begin{aligned}
G = & \frac{1}{2} \int_0^{\omega_F} \int_0^{\theta_{c,1,0}} \mathcal{T}_0(\theta, \omega) v_{1,L}(\omega) \mathcal{D}_{1,L}(\omega) \hbar \omega \frac{\partial f_{\text{BE}}^0(\omega, T)}{\partial T} \cos \theta \sin \theta d\theta d\omega \\
& + \frac{1}{2} \int_{\omega_F}^{\omega_{\text{max,L}}} \int_0^{\theta_{c,1,L}} \mathcal{T}_L(\theta, \omega) v_{1,L}(\omega) \mathcal{D}_{1,L}(\omega) \hbar \omega \frac{\partial f_{\text{BE}}^0(\omega, T)}{\partial T} \cos \theta \sin \theta d\theta d\omega \\
& + \int_{\omega_F}^{\omega_{\text{max,T}}} \int_0^{\theta_{c,1,T}} \mathcal{T}_T(\theta, \omega) v_{1,T}(\omega) \mathcal{D}_{1,T}(\omega) \hbar \omega \frac{\partial f_{\text{BE}}^0(\omega, T)}{\partial T} \cos \theta \sin \theta d\theta d\omega,
\end{aligned} \tag{5.10}$$

where we take the inelastic limit by using the Debye frequency of the harder medium  $\omega_{\text{max},j} = \max(\omega_{\text{max},1,j}, \omega_{\text{max},2,j})$ . Similarly, we can also take the elastic limit by using the Debye frequency of the softer medium  $\omega_{\text{max},j} = \min(\omega_{\text{max},1,j}, \omega_{\text{max},2,j})$ . For the cut-off frequencies of the liquid, we used Eq. (4.5). The acoustic and thermodynamic values used in the AMM calculations are listed in Table 5.1.

Table 5.1: Acoustic and thermodynamic parameters used in AMM calculations. \*Calculated using Eq. (4.5).

	$\rho$ [kg m <sup>-3</sup> ]	$M_u$ [g mol <sup>-1</sup> ]	$v_0$ [m s <sup>-1</sup> ]	$v_L$ [m s <sup>-1</sup> ]	$v_T$ [m s <sup>-1</sup> ]	$\omega_{\text{max,L}}$ [THz]	$\omega_{\text{max,T}}$ [THz]
Au	19300 <sup>[49]</sup>	196.97 <sup>[49]</sup>		3390 <sup>[49]</sup>	1290 <sup>[49]</sup>	51.42 <sup>[49]</sup>	19.57 <sup>[49]</sup>
H <sub>2</sub> O	997 <sup>[170]</sup>	18.02 <sup>[170]</sup>	1500 <sup>[170]</sup>	3500 <sup>[170]</sup>	2200 <sup>[170]</sup>	42.04*	27.61*

### 5.3 Results and discussions

Firstly, the surface roughness was measured using AFM, as described in Section 3.3 and as shown in Figure 5.8, for  $5 \times 5 \mu\text{m}$  and  $1 \times 1 \mu\text{m}$  scan areas. The scans performed over larger

areas confirmed that the surfaces were uniform at length scales comparable to the spot size of FDTR pump and probe beams. Moreover, the root mean square (RMS) surface roughness measurements showed that, in all cases, the surfaces were exceptionally smooth and showed no signs of gross defects that could significantly affect the result of FDTR measurements. The smoothest surface was found to be PFDT with an RMS value of  $0.3 \mu\text{m}$ . Since roughness can contribute to the interpretation of the measured contact angles [179], the roughness factor (RF) of each sample were quantified using the small area scans. The RF was found to be  $\approx 1$  for all surface types; ruling out significant roughness effects on the surface energy contributions subsequently inferred from the contact angle measurements.

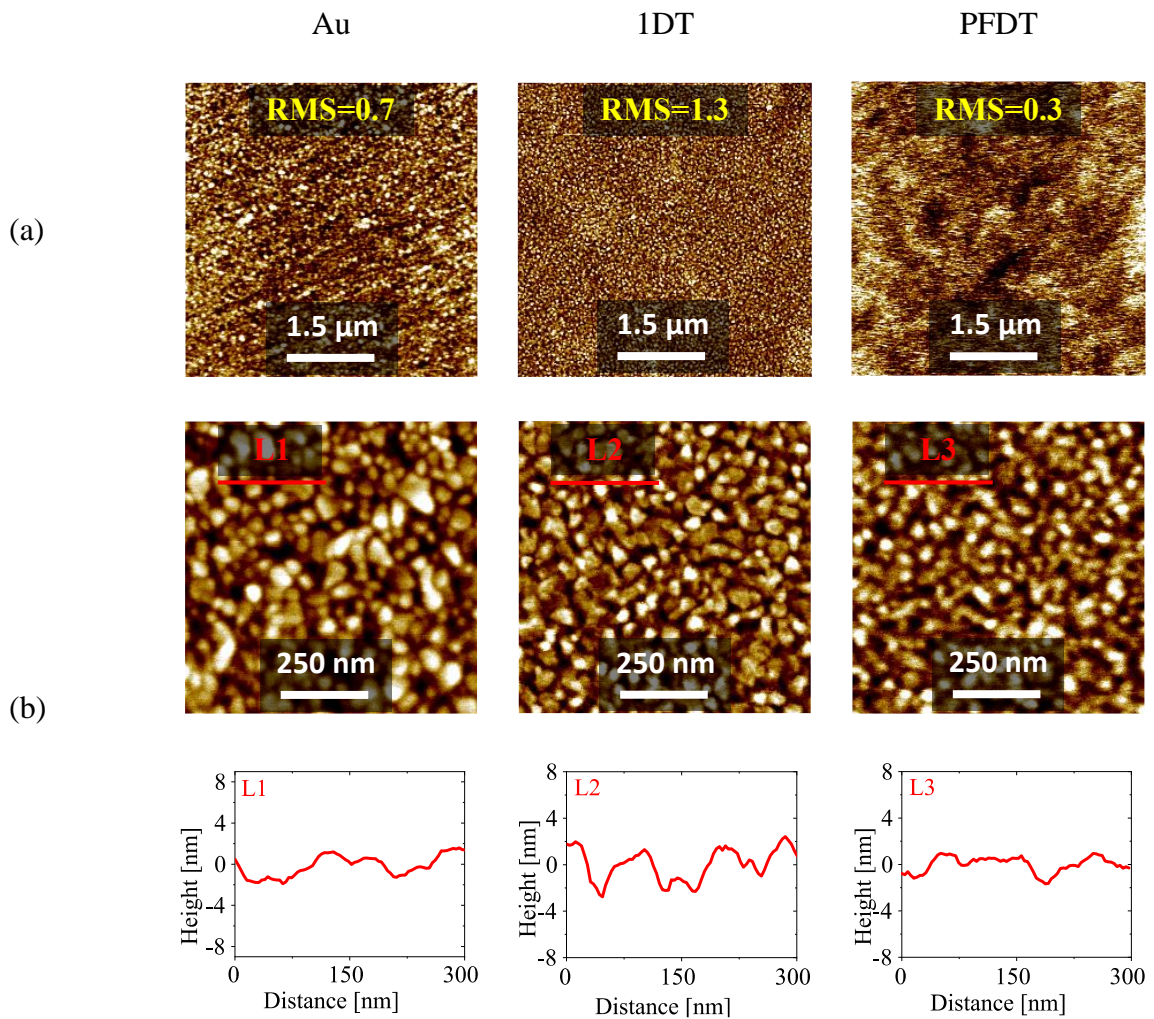


Figure 5.8: AFM images of (a)  $5 \times 5 \mu\text{m}$ , and (b)  $1 \times 1 \mu\text{m}$  of Au, 1DT, and PFDT, respectively.

Secondly, we measured the contact angle using contact angle goniometry (CAG) as described in Section 3.5, on bare Au surfaces and both SAM species (i.e., 1DT, and PFDT) assembled on the Au surface to quantify surface wetting characteristics, as shown in Figure 5.9. To ascertain the surface energy contributions of the surfaces, H<sub>2</sub>O, which is strongly polar, and CH<sub>2</sub>I<sub>2</sub>, which is weakly polar, were used as probe liquids. Advancing,  $\theta_{ca,ad}$ , and receding,  $\theta_{ca,re}$ , contact angles between the surface and the probe liquid were measured at the three-phase contact line of the droplet. Contact angle hysteresis (e.g., the difference between the advancing and receding contact angles,  $\Delta\theta = \theta_{ca,ad} - \theta_{ca,re}$ ) can arise from surface roughness and chemical heterogeneity effects, though  $\theta_{ca,ad}$  is expected to encode relevant information regarding the nominal chemical nature of surface [180]. Thus, the measured  $\theta_{ca,ad}$  were used to determine the surface energy contributions estimated using the Fowkes method [181], [182], and the known polar/dispersive properties of the probe liquids by:

$$\gamma_{sl} = \gamma_{lv} + \gamma_{sv} - 2(\sqrt{\gamma_{lv,dis}\gamma_{sv,dis}} + \sqrt{\gamma_{lv,pol}\gamma_{sv,pol}}), \quad (5.11)$$

where  $\gamma$  is the excess surface energy between solid, liquid, and vapor, represented by subscripts  $s$ ,  $l$ , and  $v$ , respectively, with additional subscripts  $dis$  and  $pol$  interpreted as the dispersive and polar contributions, respectively.

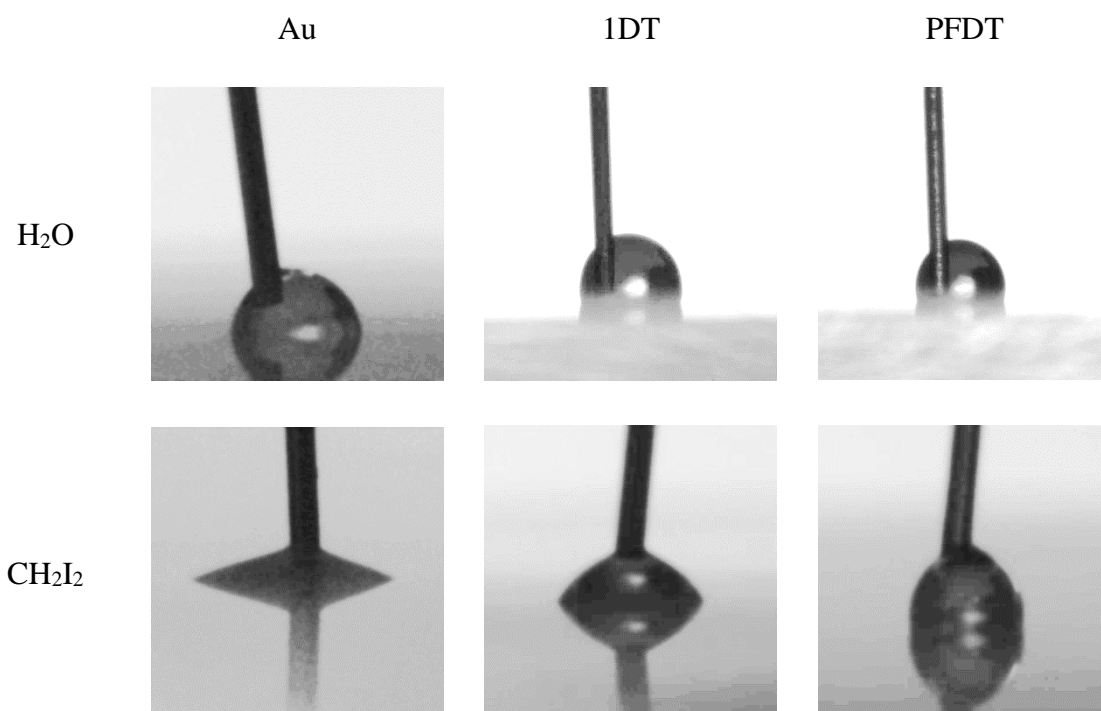


Figure 5.9: Advancing contact angle images for H<sub>2</sub>O, and diiodomethane (CH<sub>2</sub>I<sub>2</sub>) on bare Au, 1DT, and PFDT, respectively. For scale reference, the dispensing needle has an outer diameter of 135  $\mu\text{m}$ .

Figure 5.10(a) shows that PFDT has the highest advancing contact angle with a contact angle hysteresis of  $\sim 10^\circ$  for advancing and receding, indicating that this SAM species is the most hydrophobic. The surface with the highest hysteresis was the Au interface. Literature suggests that Au can be easily contaminated with physisorbed species resulting in impure surfaces [10] and that this occurs rapidly within minutes once the clean surface is exposed to ambient air [183]. The SAM layers appear to have reduced hysteresis on the Au surface by introducing a monolayer that reduces the tendency to adsorb hydrocarbons to the surface. Figure 5.10(a) shows that the energy profiles of both SAMs and the bare Au surface. The presence of the SAMs results in a reduction of the interfacial energy of the Au surface at  $\sim 45 \text{ mJ m}^{-2}$ . As expected, PFDT causes the most dramatic drop in energy due to the presence of the fluorinated groups [184]. This is reflected in Figure 5.10 as the 1DT's CH<sub>3</sub> terminated is still much higher in energy  $\sim 33 \text{ mJ m}^{-2}$ , in relation to the CF<sub>3</sub> terminated PFDT at  $\sim 10 \text{ mJ m}^{-2}$ .

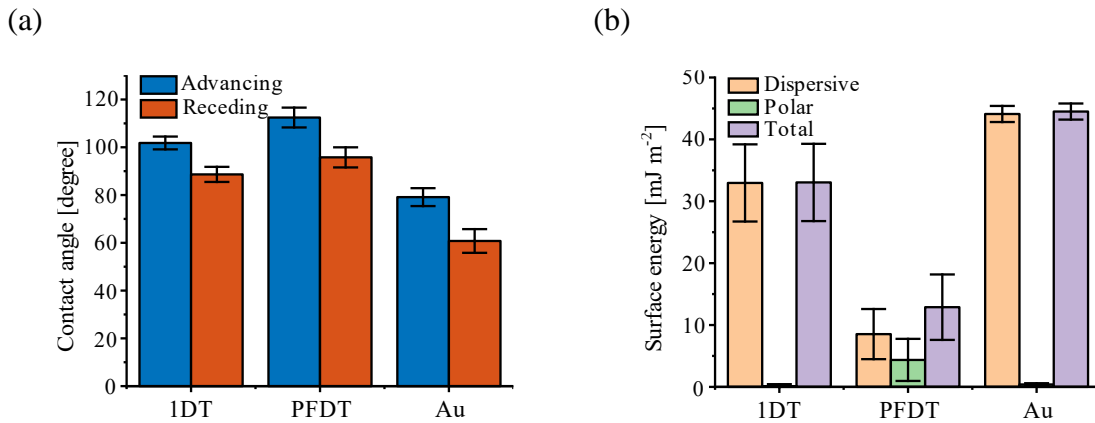


Figure 5.10: (a) Contact angle measurements for advancing and receding behaviour of  $\text{H}_2\text{O}$  on 1DT, PFDT and bare Au. (b) Surface energies of 1DT, PFDT, and bare Au determined using the Fowkes method [181], [182] with advancing contact angle of  $\text{H}_2\text{O}$ , and  $\text{CH}_2\text{I}_2$ .

### 5.3.1 Quantifying effective Au- $\text{H}_2\text{O}$ TBC using FDTR and AMM

We used the FDTR technique as described in Section 3.6 with the bidirectional heat flow theory (see Section 5.2.2) to study the effect of wettability on TBC across the Au-water interface. Figure 5.11 shows the typical pattern of the measured sites in a liquid cell. Before measuring a liquid cell sample, the Au transducer thermal conductivity was measured via the four-point probe method, as described in Section 3.4; this was followed by the measurements of the substrate ( $\text{SiO}_2$ ) thermal conductivity using the FDTR with the measured Au thermal conductivity in the fitting process. These values were then kept as constant when fitting the FDTR data of each liquid cell sample.

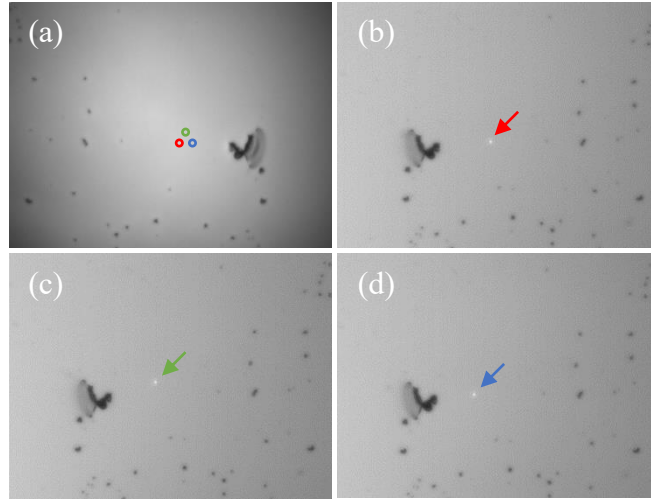


Figure 5.11: Au transducer surface of a liquid cell observed from (a) CCD 1 (Au-SiO<sub>2</sub> interface) and indication of the locations of three sites measured in red, green, and blue, respectively. Surfaces in (b), (c), and (d) were observed through CCD 2 (Au-water interface), where some of the transmitted probe spot can be seen from CCD 2. CCD 1 is located on the FDTR side, while CCD 2 is from the second fluorescence microscope setup.

Considering a thermal resistance model where we allow the SAM interposed as shown in Figure 5.12, to act as part of the effective TBR, the measured effective Au-H<sub>2</sub>O TBC,  $G_{\text{eff,Au-H}_2\text{O}}$ , can be described by

$$G_{\text{eff,Au-H}_2\text{O}}^{-1} = G_{\text{Au-SAM}}^{-1} + \frac{d_{\text{t,SAM}}}{\kappa_{\text{SAM}}} + G_{\text{SAM-H}_2\text{O}}^{-1}, \quad (5.12)$$

where  $d_{\text{t}}/\kappa$  is the ratio of layer thickness to material thermal conductivity and it represents the thermal resistance of the layer per unit area.

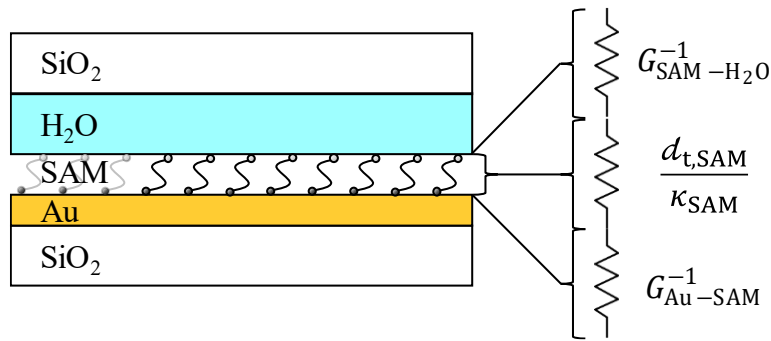


Figure 5.12: Schematic of a multilayered liquid cell sample structure interposed with SAM. The three terms are the resistances that makes up the effective Au-H<sub>2</sub>O TBR.

Figure 5.13 shows the effective TBC distribution of Au-water interfaces with and without SAMs [185] using the Monte Carlo method described in Section 3.6.6. As expected, we observed a noticeable and distinguishable difference in TBC and the width of the confidence intervals becomes narrower for lower TBC. However, the effective TBC distributions for Au-water interfaces are almost Gaussian and remained almost Gaussian regardless of the type of surface treatment.



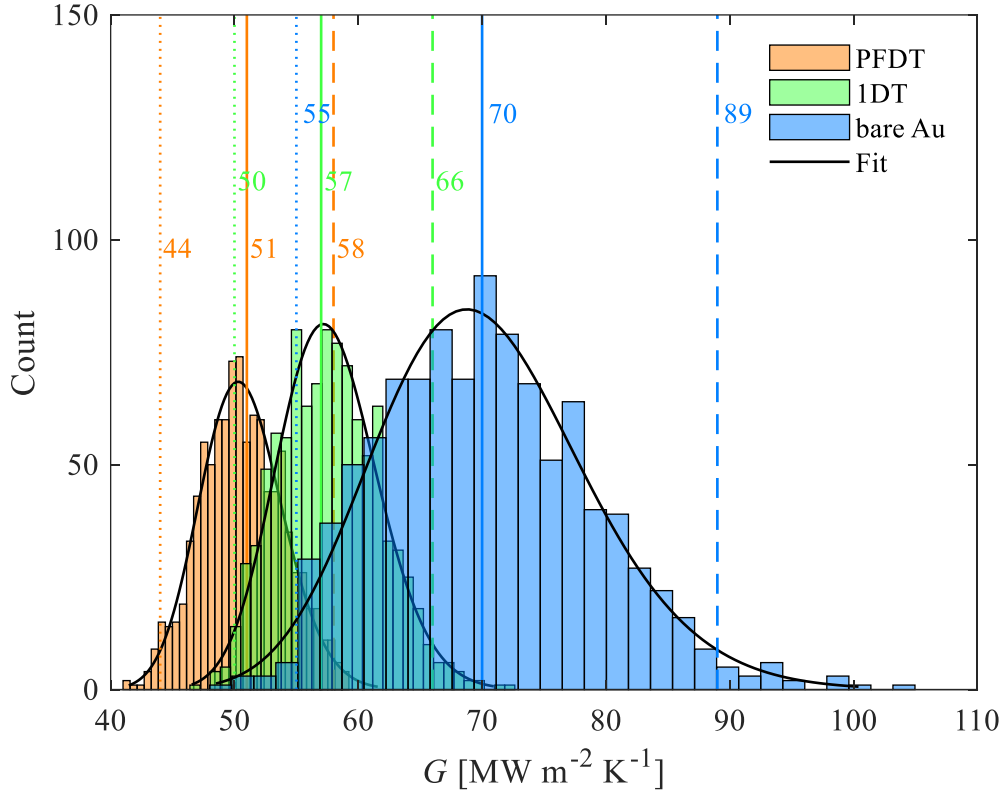


Figure 5.13: Thermal boundary conductance distribution of Au-PFDT-H<sub>2</sub>O, Au-1DT-H<sub>2</sub>O, and Au-H<sub>2</sub>O using Monte Carlo method [185], where solid lines represent mean, while dotted and dashed lines represent the lower and upper confidence intervals at 95%, respectively.

Figure 5.14 shows the measured effective TBC across Au-water interfaces as a function of the dimensionless work of adhesion,  $1 + \cos \theta_{ca}$ , in comparison to previous experimental [13], [157] and simulation [158], [159] studies in the literature. We note that the SAMs samples were submerged immediately in dilute solution with their respective thiol post Au deposition, while the sample with bare Au surface was exposed in ambient air for a short period until the liquid cell was assembled. The measured value of the effect TBC with a 1DT interfacial layer at  $1 + \cos \theta_{ca} \sim 0.76$  is consistent with the value reported by Ge *et al.* for a similar hydrocarbon chain [13]. Our data with PFDT at  $1 + \cos \theta_{ca} \sim 0.59$  is consistent with MD data [158], [159]. To plot the TBC as a function of the dimensionless work of adhesion using the continuum theory described in Section 5.2.3, we related the

measured contact angle to the interaction energy in Eq. (5.9) through the Hamaker constant,  $C_H$ , where  $C_H$  is given by [94]

$$C_H = 4\varepsilon\pi^2\rho_{N,1}\rho_{N,2}\sigma_{12}^6, \quad (5.13)$$

where  $\rho_{N,i}$  is the number density for material  $i$ . The use of Hamaker constant here is reasonable as it gives interaction information about a given van der Waals type pair potential, which these solid-liquid systems are of van der Waals type. The Hamaker constant can also be expressed in terms of adhesion energy and is written as [186] (see Appendix A)

$$C_H = 16\pi z_0^2 \Delta\gamma = 16\pi z_0^2 \gamma_l (1 + \cos \theta_{ca}), \quad (5.14)$$

where  $z_0 = (2/5)^{1/6}\sigma_{12}$  and is the equilibrium distance between the atom pair under zero load [58], and  $\gamma_l$  is the surface tension of the liquid. We calculated  $\sigma_{12}$  by using the Lorentz–Berthelot mixing rule,  $\sigma_{12} = (\sigma_1 + \sigma_2)/2$ , and for water, we used surface tension  $\gamma_l = 72 \text{ mJ m}^{-2}$ . Following literature [170], we approximated the number of surface atoms by  $N_{\text{surf}} = 1/\sigma_{12}^2$ . The experimental data, except for one point, is within the elastic and inelastic limits of the AMM predictions (see Figure 5.14). The 95% confidence interval is comparable to the margin of error from the work of Ge *et al.* [13]. Moreover, based on all previous results shown here, all three, simulations, experimental, and analytical, we expected the effective TBC to scale proportionally with work of adhesion,  $G \propto 1 + \cos \theta_{ca}$ . However, for our well-quantified measurements, we observe TBC to be significantly below the trend when the bare Au surface has been exposed in the optical characterisation lab environment for four days prior to H<sub>2</sub>O introduction onto the surface. Simultaneously, the results indicate that TBC across the Au-water interface is not purely dependent on work of adhesion. The experimental work of Park *et al.* [187] also indicates this.

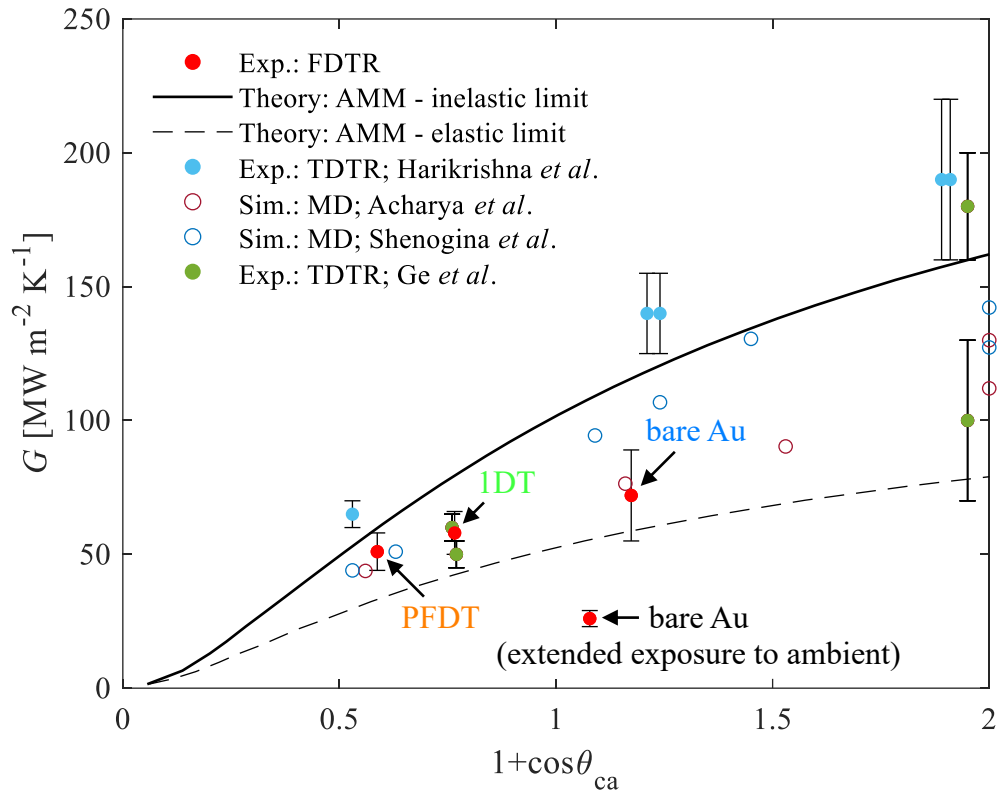


Figure 5.14: Effective TBC across Au-water interface as a function of the dimensionless work of adhesion. The lines represent the analytical model, unfilled markers represent simulation data, and filled markers represent experimental data.

### 5.3.2 Measurement of effective Au-C<sub>2</sub>H<sub>6</sub>O TBC using FDTR

To further confirm the finding in Section 5.3.1, we prepared and replicated the bare Au with extended exposure to ambient and used these samples to form Au-C<sub>2</sub>H<sub>6</sub>O, Au-1DT-C<sub>2</sub>H<sub>6</sub>O, and Au-PFDT-C<sub>2</sub>H<sub>6</sub>O. We chose C<sub>2</sub>H<sub>6</sub>O as it one of the simplest working fluids used in two-phase cooling [188]. The measured FDTR data were fitted, and we determined thermal conductivity and TBC simultaneously. The measured thermal conductivity agrees with the literature (see Table 5.2). This provides confidence in the TBC value of  $2.09 \pm 0.1$  W m<sup>-1</sup> K<sup>-1</sup> for C<sub>2</sub>H<sub>6</sub>O on bare Au and, by extension, to the effective TBC with 1DT, and PFDT SAMs.

Table 5.2: Measured thermal conductivity and TBC for C<sub>2</sub>H<sub>6</sub>O in contact with bare Au, 1DT, and PFDT, respectively.

	$\kappa$ [W m <sup>-1</sup> K <sup>-1</sup> ]	Expected $\kappa$ [W m <sup>-1</sup> K <sup>-1</sup> ] at 298 K	$G$ [MW m <sup>-2</sup> K <sup>-1</sup> ]
Au-C <sub>2</sub> H <sub>6</sub> O	0.172 ± 0.008	0.167 <sup>[155]</sup>	2.09 ± 0.2
Au-1DT-C <sub>2</sub> H <sub>6</sub> O	0.162 ± 0.02		2.71 ± 0.16
Au-PFDT-C <sub>2</sub> H <sub>6</sub> O	0.168 ± 0.02		2.81 ± 0.02

Figure 5.15 compares the TBC measurements with C<sub>2</sub>H<sub>6</sub>O to the only other dataset available for Au-C<sub>2</sub>H<sub>6</sub>O and Au-SAM-C<sub>2</sub>H<sub>6</sub>O systems [156]. We observed that, in comparison, the measured TBC for C<sub>2</sub>H<sub>6</sub>O on bare Au is  $\sim 8.5 \times$  smaller. Moreover, both SAMs measured demonstrated more than an order of magnitude smaller effective TBC in comparison to the measurements of Tian *et al.* despite the similarity of the SAMs studied (e.g., nature of the ligand bond). Therefore, we can rule out the difference in the SAM molecule carbon chain length. As such, the current cause of the inconsistency remains unresolved.

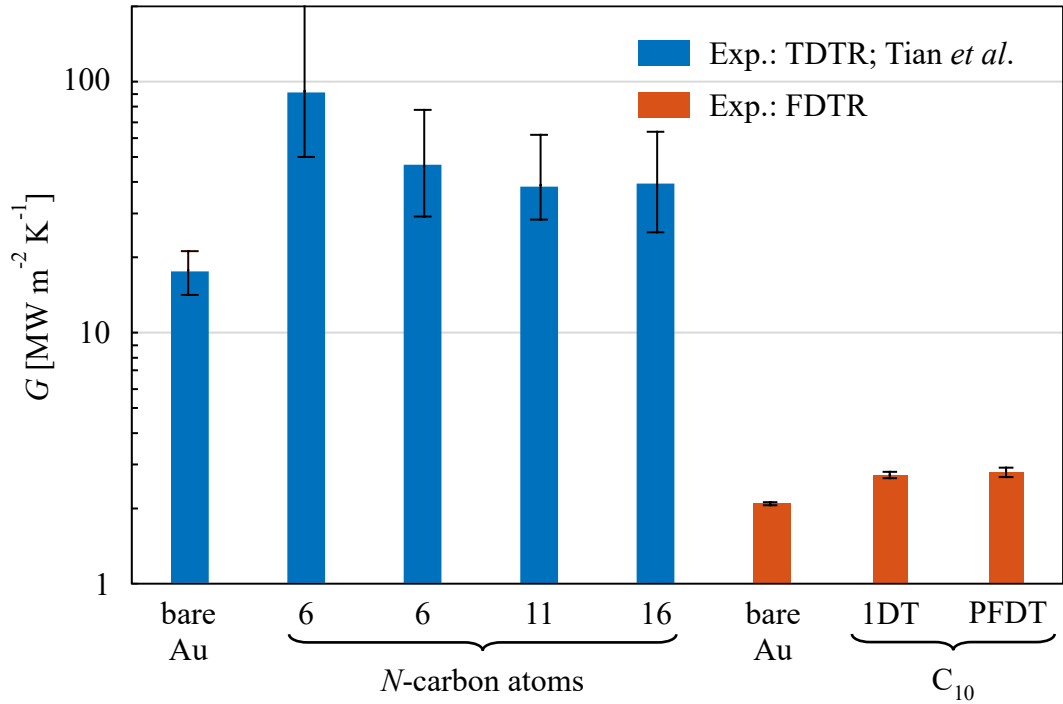


Figure 5.15: Effective TBC across Au-C<sub>2</sub>H<sub>6</sub>O interface with and without hydrogenated SAMs. TDTR data taken from literature [156].

## 5.4 Conclusions

In this chapter we introduced the concept of self-assembled monolayers, and how they can be fabricated and used to manipulate surface energy. We introduced the bidirectional heat transfer model to analyse frequency-domain thermoreflectance data of solid-liquid systems. We also introduced a modified analytical model to predict thermal boundary conductance as a function of wettability. We attempted to create a baseline frequency-domain thermoreflectance measurement of Au-liquid systems for measurements with engineered fluids (fluorinated fluids), by independently investigating the effect of wettability on thermal boundary conductance using well-studied Au-water systems.

We measured the thermal boundary conductance across the Au-H<sub>2</sub>O interface, and the effective thermal boundary conductance across the Au-H<sub>2</sub>O interface with self-assembled monolayers. In general, the experimental results agree well with the literature.

However, we discovered that it is not possible to create a baseline with exposed Au surfaces, since contamination with physisorbed species from ambient air greatly impacts the effective thermal boundary conductance of water on Au.

To confirm the impact of physisorbed species on Au, we measured ethanol on Au with and without self-assembled monolayers. Again, we observed a drastic reduction in thermal boundary conductance when the Au surface was exposed for an extended period prior to introduction of the ethanol. Our results suggest that the enhanced thermal resistance is due to contamination with physisorbed species from ambient, and not due to the self-assembled monolayers or its chain length.

In Chapter 6, we will study the effect on effective thermal boundary conductance across Au-H<sub>2</sub>O with a known physisorbed species on an Au surface and develop an analytical model to predict the effective thermal boundary conductance across the solid-liquid interface.

Part of the work presented in this chapter has been presented at the International Symposium on Thermal Effects in Gas flows in Microscale, *Ettlingen* [V][189], and published in IOP Journal of Physics: Conference Series [IV][185].

## Chapter 6.

# Effect of alkane interlayer on interfacial thermal transport

## 6.1 Introduction

One issue limiting the performance of integrated single-phase and two-phase cooling devices described in Section 1.2.1 and 1.2.3 is contamination on the surface which limits the heat transfer across solid-liquid interfaces. Fabrication of these devices is generally complicated and costly. As such, it is important to verify the actual thermal performance through experiments and understand the effect of physisorbed contaminants that can be formed in an uncontrolled or poorly controlled environment, prior to working fluid introduction, has on the thermal transport across solid-liquid interfaces.

When dealing with devices at the macroscale, interfacial effects are typically ignored as the ratio of volume to surface area is relatively large. However, as characteristic lengths approach to micron and nanoscale, the ratio of surface area to volume to surface area shrinks and thermal boundary conductance (TBC),  $G$ , becomes a concerning thermal parameter. It has been observed that adsorption of contaminants from the environment on a surface could influence the apparent surface energies [181], and therefore also influence energy transfer at the interface.

Shenogina *et al.* [159] showed the TBC proportional to the work of adhesion across metal-liquid interfaces by simulating self-assembled monolayers (SAM) with various functional groups. Motivated by the simulation work, Harikrishna *et al.* [157] experimentally quantified the effect of work of adhesion on TBC across solid-liquid interfaces by using the

time-domain thermoreflectance (TDTR) technique, and confirmed the findings by Shenogina *et al.* [159].

In Chapter 5, we showed that a modified acoustic mismatched model (AMM) can be used to better understand and predict how phonons transport across solid-liquid interfaces which accounts for the viscoelastic and interface bonding effects, and is consistent with the phonon liquid theory and satisfies Frenkel's findings on solid-like behaviours in fluids [174], [175]. The theoretical model demonstrated the capabilities in predicting TBC as a function of interfacial bonding strength with relatively good agreement with literature [13], [157].

The results in Chapter 5 suggests that there is a lack of precise explanation to why TBC across the solid-liquid interface lacks a clear trend with work of adhesion,  $\Delta\gamma_{sl}$ , reported by Qian *et al.* [190]. Unfortunately, the disordered nature of liquids makes it impossible to study at a more fundamental level due to the lack of classical description of such system in terms of collective propagative excitations. This is the main reason to why the fundamental understanding of thermal transport across solid-liquid interfaces is still partial.

In this chapter, the effect of an alkane interlayer on the effective solid-liquid TBC was rationalized by a controlled physisorbed species. We quantify the effect by using the frequency-domain thermoreflectance [95] (FDTR) technique. Additionally, this chapter will present an extension to a continuum theory inspired by the framework developed by Merabia *et al.* [170] to better understand phonon transmission probabilities across solid-liquid interfaces with a van der Waals type bonding interlayer.



## 6.2 Materials and methods

To investigate the effect that Au surface contamination from physisorption due to ambient exposure has on effective thermal transport across the Au-liquid interface, we used a known physisorbed species. Nonane ( $C_9H_{20}$ ) was chosen as it is typically used to represent a model volatile organic compound species found in the atmosphere [191], [192]. This single bond molecule is ideal since it has strong binding energy involving two valence electrons [193] and high vapor pressures at approximately 365 Pa under room temperature [194]. The simple structure diagram and ball and stick model of  $C_9H_{20}$  are shown in Figure 6.1(a) and (b), respectively. High performance liquid chromatography (HPLC) grade deionised water ( $\rho_r = 18.2 \text{ M}\Omega \text{ cm}$ ), HPLC grade acetone (purity  $\geq 99.9\%$ ), isopropyl alcohol (suitable for HPLC, purity 99.9%), and nonane (anhydrous, purity  $\geq 99\%$ ) were purchased from Sigma-Aldrich for cleaning the fused silica ( $SiO_2$ ) substrates prior to Au deposition, contact angle measurements and synthesis, respectively.

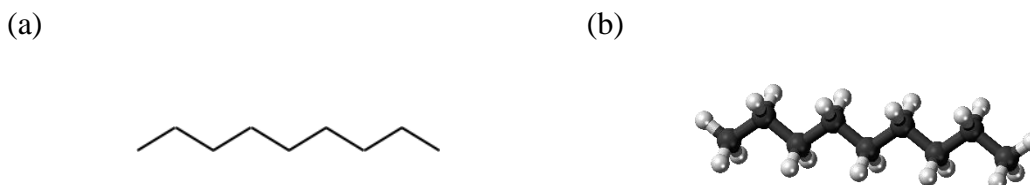


Figure 6.1: Nonane: (a) Line drawing, and (b) ball and stick model. Adapted from CRC Handbook of Chemistry and Physics [155]

To better understand how a physisorbed layer affect thermal transport across solid-liquid interface, we build on the theory presented in Section 5.2.3. We accompanied the continuum theory with experimental data using the frequency-domain thermoreflectance (FDTR) technique and supporting experimental techniques described in Chapter 3 and Section 5.2.2.

### 6.2.1 Sample preparation and fabrication

The samples used to investigate the effect of physisorbed  $C_9H_{20}$  layer on TBC across Au-water interfaces shares similarities of the samples with SAMs used Chapter 5 in terms of the layered structure.

Four samples were fabricated from a 4-inch (101.6 mm) diameter and 1 mm thick fused silica wafer substrate. The wafer surface was oxygen plasma treated to remove organic contamination using the Diener PICO barrel asher. A single 1 nm Ti adhesion layer was deposited onto the wafer using physical vapor deposition followed by 100 nm Au film. Both films were deposited using electron beam evaporation with the Temescal FC-2000 as described in Section 3.6.3. The wafer was covered with a layer of photoresist using the spin coating method [195] to protect the Au surface during dicing. The wafer was then separated into  $20 \times 20$  mm tiles. After the dicing process, the photoresist was removed with acetone, isopropyl alcohol, and then followed by deionised water. The surface of the samples was plasma treated again to remove any remaining organic contamination.

Following literature[181], two samples were placed in a sealed desiccator containing a vial of nonane at room temperature and under atmospheric pressure. One of the samples was used to form a liquid cell with the stack structure  $SiO_2$ -Au- $H_2O$ - $SiO_2$ . The first set of samples completely saturated with the  $C_9H_{20}$  were used to form the liquid cells, which were assembled similarly to the  $SiO_2$ -Au- $H_2O$ - $SiO_2$  sample with the multilayered structure as shown in Figure 6.2. The remaining surface was treated, and non-treated samples were used for Au surface roughness measurements, Au thermal conductivity measurements, and contact angle measurements by using atomic force microscopy as described in Section 3.3, four-point probe method in conjunction with Wiedemann-Franz law described in Section 3.4, and contact angle goniometry as described in Section 3.5, respectively.

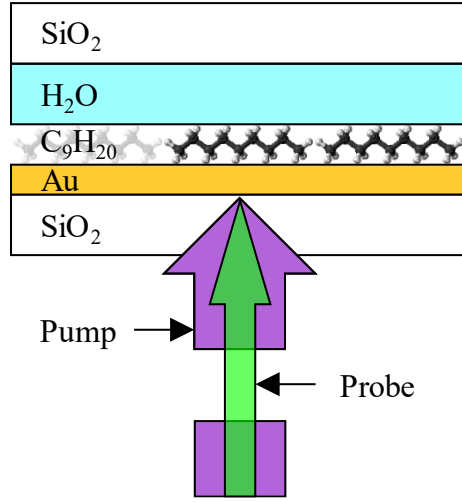


Figure 6.2: Schematic of multilayered liquid cell sample structure with  $C_9H_{20}$  interlayer. The laser induced heating spreads in all directions within the Au transducer.

### 6.2.2 AMM for weakly bonded complex solid-liquid interfaces

Consider a solid-liquid interface with a physisorbed layer interposed, as illustrated in Figure 6.3. The heat flux travels from material 1 to 2, then from material 2 to 3. If energy is conserved and assuming no heat energy remains in 2, we have the heat flux  $q_{13} = q_{12} + q_{23}$  which may be used to describe the overall temperature change from material 1 to 3, thus  $G_{13}$  with transmissions  $\mathcal{T}_{13}$  can be obtained by the definition of TBC. The final transmission terms may be calculated using a transfer matrix method. Considering that the reflected energy back towards the incident direction is relatively small, we approximated  $\mathcal{T}_{13,j}$  by taking the product of  $\mathcal{T}_{12,j}$  and  $\mathcal{T}_{23,j}$  for simplicity. Since the incident angle approaching the second interface depends on the refraction angle  $\theta_2$ , a second critical angle can be defined similarly to the previous critical cone, if  $v_{2,j} < v_{3,j}$ . This means that  $\mathcal{T}_{23,j}$  should also depend on  $v_1$  through an equivalent of Snell's law, and therefore that the average energy transmission,  $\Gamma$ , from material 1 to 3 may effectively be described by

$$\Gamma_{13,j} = \Gamma_{12,j} \Gamma_{23,j}(v_{1,j}) \quad (6.1)$$

with:

$$\Gamma_{12,j} = \int_0^{\theta_{c,12,j}} \mathcal{T}_{12,j} \cos \theta_1 \sin \theta_1 d\theta_1, \quad (6.2)$$

$$\Gamma_{23,j} = \int_0^{\theta_{c,23,j}} \mathcal{T}_{12,j}(v_{1,j}) \cos \theta_2 \sin \theta_2 d\theta_2,$$

and with:

$$\mathcal{T}_{12,j} = \frac{4Z_{1,j}Z_{2,j} \cos \theta_1 \cos \theta_2}{(Z_{1,j} \cos \theta_1 + Z_{2,j} \cos \theta_2)^2 + \left(\frac{\omega}{K_{12}}\right)^2 (Z_{1,j}Z_{2,j} \cos \theta_1 \cos \theta_2)^2}, \quad (6.3)$$

$$\mathcal{T}_{23,j} = \frac{4Z_{2,j}Z_{3,j} \cos \theta_2 \cos \theta_3}{(Z_{2,j} \cos \theta_2 + Z_{3,j} \cos \theta_3)^2 + \left(\frac{\omega}{K_{23}}\right)^2 (Z_{2,j}Z_{3,j} \cos \theta_2 \cos \theta_3)^2},$$

where  $Z_{i,j} = \rho_i v_{i,j}$  and is the acoustic impedance for material  $i$  with polarisation  $j$ . Using Eq. (6.1)-(6.3) and assuming  $\omega_{F,C_9H_{20}} = \omega_{F,H_2O}$ , similar to Eq. (5.4), we rewrite the decomposed effective TBC as

$$G_{13} = G_{13,0} + G_{13,L} + G_{13,T} \quad (6.4)$$

with:

$$G_{13,0} = \frac{1}{2} \int_0^{\omega_F} \Gamma_{13,0} v_{1,L} \mathcal{D}_{1,L} \hbar \omega \frac{\partial f_{BE}^0}{\partial T} d\omega,$$

$$G_{13,L} = \frac{1}{2} \int_{\omega_F}^{\omega_{c,L}} \Gamma_{13,L} v_{1,L} \mathcal{D}_{1,L} \hbar \omega \frac{\partial f_{BE}^0}{\partial T} d\omega, \quad (6.5)$$

$$G_{13,T} = \int_{\omega_F}^{\omega_{c,T}} \Gamma_{13,T} v_{1,T} \mathcal{D}_{1,T} \hbar \omega \frac{\partial f_{BE}^0}{\partial T} d\omega.$$

Here,  $\mathcal{D}$  is the phonon density of states (DOS),  $f_{\text{BE}}^0(\omega, T) = 1/(e^{\hbar\omega/k_{\text{B}}T} - 1)$  and is the Bose-Einstein equilibrium phonon distribution,  $k_{\text{B}}$  is the Boltzmann constant, and  $T$  is the local temperature.

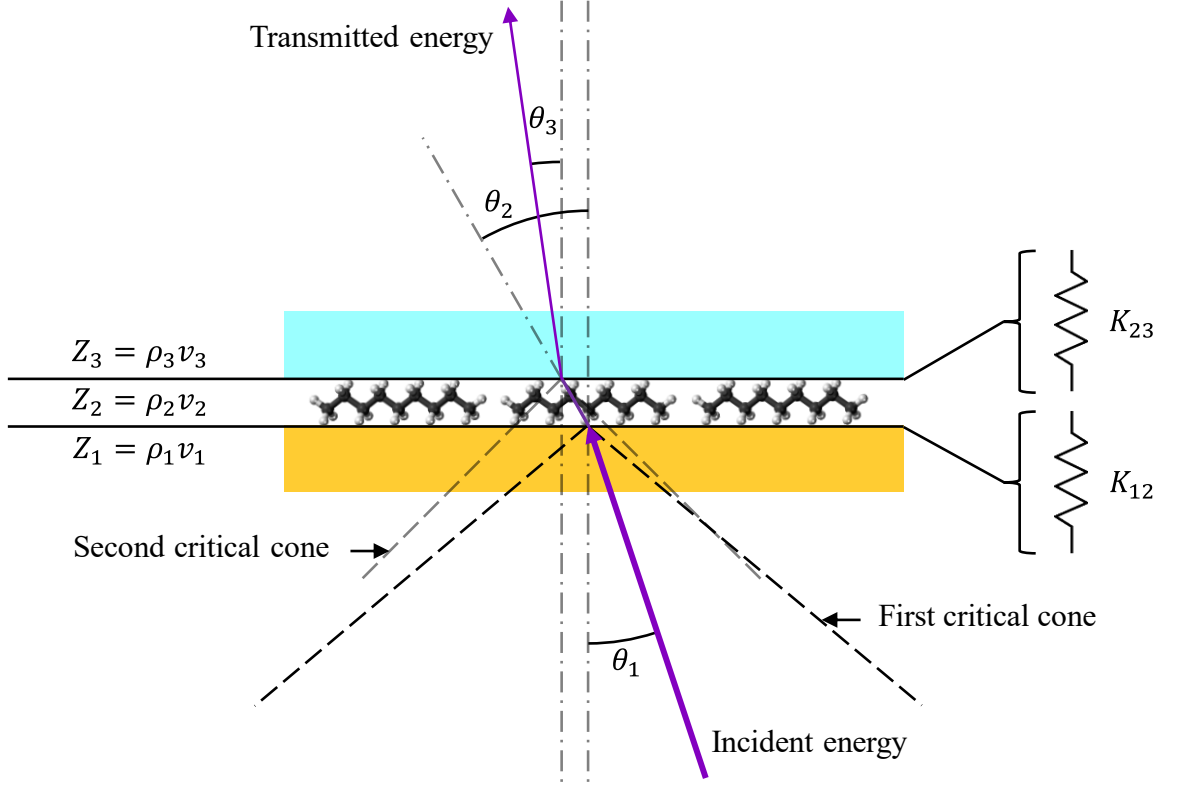


Figure 6.3: Schematic illustration of the energy transmission across solid-nonane-liquid interfaces.

Following Chapter 5, we take the length scale parameter as  $\sigma_{12} = (\sigma_1 + \sigma_2)/2$ , where  $\sigma_1 = (1/\sqrt{2})(4/\rho_1)^{1/3}$ , and similarly for  $\sigma_{13}$ , with  $\sigma_{\text{H}_2\text{O}} = 0.275$  nm. For  $\sigma_2$ , we take  $\sigma_{\text{C}_9\text{H}_{20}} = 0.619$  nm by considering spherical nonane [196]. As for the phonon DOS and number of surface atoms per unit area, we also take  $\mathcal{D}_{1,j} = \omega^2/(2\pi^2 v_{1,j}^3)$  and  $N_{\text{surf},12} = 1/\sigma_{12}^2$ , respectively, and similarly for  $N_{\text{surf},23}$ . Other important physical and acoustic parameters used are contained in Table 5.1 and Table 6.1.

Table 6.1: Acoustic and thermodynamic parameters used in AMM calculations. \*Extrapolated by assuming nonane longitudinal, and transverse sound velocities having a similar relationship to the adiabatic sound velocity as water. \*\*Calculated using Eq. (4.5).

	$\rho$ [kg m <sup>-3</sup> ]	$M_u$ [g mol <sup>-1</sup> ]	$v_0$ [m s <sup>-1</sup> ]	$v_L$ [m s <sup>-1</sup> ]	$v_T$ [m s <sup>-1</sup> ]	$\omega_{\max,L}$ [THz]	$\omega_{\max,T}$ [THz]
C <sub>9</sub> H <sub>20</sub>	719 <sup>[155]</sup>	128.25 <sup>[155]</sup>	1227 <sup>[197]</sup>	2863*	1800*	16.74**	10.52**

## 6.3 Results and discussions

### 6.3.1 Measurement of effective Au-C<sub>9</sub>H<sub>20</sub>-H<sub>2</sub>O TBC using FDTR

Considering a thermal resistance model where we allow the C<sub>9</sub>H<sub>20</sub> interlayer as shown in Figure 6.4 to act as part of the effective TBR, then the measured effective Au-H<sub>2</sub>O TBC,  $G_{\text{eff,Au-H}_2\text{O}}$ , can be described by

$$G_{\text{eff,Au-H}_2\text{O}}^{-1} = G_{\text{Au-C}_9\text{H}_{20}}^{-1} + \frac{d_{t,\text{C}_9\text{H}_{20}}}{\kappa_{\text{C}_9\text{H}_{20}}} + G_{\text{C}_9\text{H}_{20}\text{-H}_2\text{O}}^{-1} \quad (6.6)$$

where  $d_t/\kappa$  is the ratio of layer thickness to material thermal conductivity and it represents the thermal resistance of the layer per unit area.

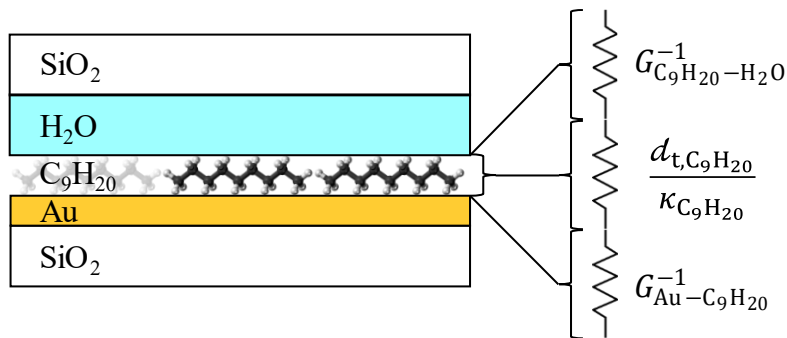


Figure 6.4: Schematic of multilayered liquid cell sample structure with C<sub>9</sub>H<sub>20</sub> interlayer. The three terms are the resistances that makes up the effective Au-H<sub>2</sub>O TBR.

Figure 6.5(a) shows the measured phase lag data and fit for the Au-SiO<sub>2</sub>, Au-H<sub>2</sub>O, and Au-C<sub>9</sub>H<sub>20</sub>-H<sub>2</sub>O samples using the FDTR system. A three-parameter fit was performed on the Au-SiO<sub>2</sub> FDTR data to determine the SiO<sub>2</sub> thermal conductivity, SiO<sub>2</sub> volumetric heat capacity, and the TBC across Au-SiO<sub>2</sub> interfaces, which are used in subsequent fittings, as the substrates of each sample originate from the same fused silica wafer. The measured and fitted results were consistent with the baseline sample (see Figure 3.13). This was followed by a three-parameter fit on the Au-H<sub>2</sub>O FDTR data using the measured substrate thermal parameters. The measured and fitted results were also consistent with the results presented in Section 5.3.1 for well-prepared bare Au surface samples. The TBC across Au-H<sub>2</sub>O interfaces was measured to be 86 MW m<sup>-2</sup> K<sup>-1</sup>, which is in good agreement with literature [13] for hydrophilic Au surfaces. Finally, similarly for Au-C<sub>9</sub>H<sub>20</sub>-H<sub>2</sub>O, the measured parameters of the substrate and the working fluid used to fit the FDTR data. However, noticed that the thermal conductivity and volumetric heat capacity become indistinguishable at 10<sup>5</sup> Hz and above shown in Figure 6.5(b). As a result, they are weighted as the thermal effusivity in the fitted frequency range where it is most sensitive to the TBC.

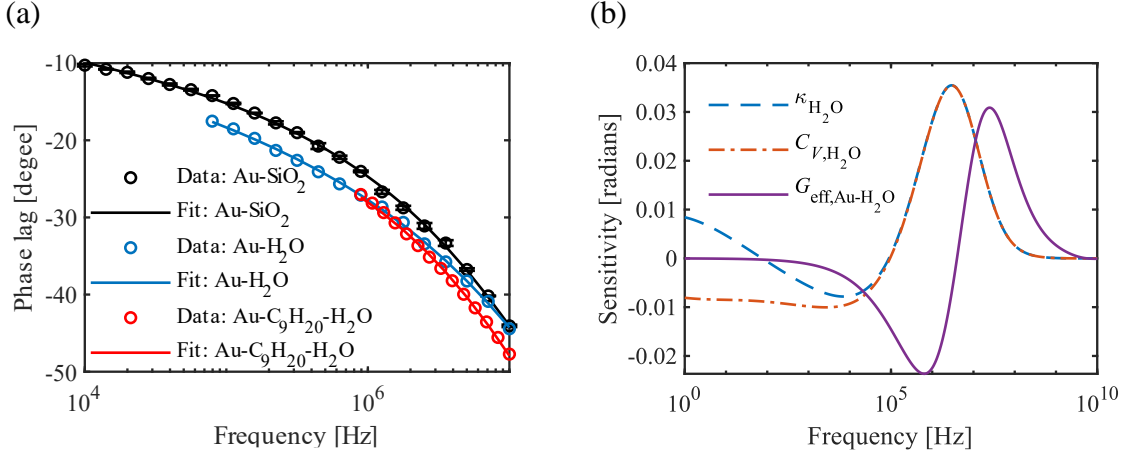


Figure 6.5: (a) Measured phase lag data and fit (using Eq. (3.45)) for Au-SiO<sub>2</sub>, Au-H<sub>2</sub>O, and Au-C<sub>9</sub>H<sub>20</sub>-H<sub>2</sub>O samples. (b) Theoretical sensitivity to the thermal conductivity, volumetric heat capacity, and effective TBC were calculated using Eq. (3.47) based on the measured values for the SiO<sub>2</sub>-Au-C<sub>9</sub>H<sub>20</sub>-H<sub>2</sub>O-SiO<sub>2</sub> liquid cell.

Figure 6.6 shows the advancing and receding contact angles and are measured to be  $\theta_{\text{ca,ad}} = 102 \pm 2^\circ$  and  $\theta_{\text{ca,re}} = 52 \pm 3^\circ$ , respectively. Using the measured contact angle, the dimensionless work of adhesion is  $1 + \cos \theta_{\text{ca}} = 0.79$ . We should expect a TBC value comparable to 1DT, as seen Figure 5.14, or  $65 \text{ MW m}^{-2} \text{ K}^{-1}$  with  $\theta_{\text{ca,ad}} = 118 \pm 2^\circ$  using CH<sub>3</sub> terminated SAM on Au, as demonstrated by Harikrishna *et al.* [157]. However, the effective TBC across Au-H<sub>2</sub>O interface with C<sub>9</sub>H<sub>20</sub> interlayer was measured to be  $4.6 \text{ MW m}^{-2} \text{ K}^{-1}$ . The measured value is significantly lower than when the deionised water is in direct contact with a well-prepared bare Au surface. We showed that the TBC does not necessary trend with the thermodynamic work of adhesion.



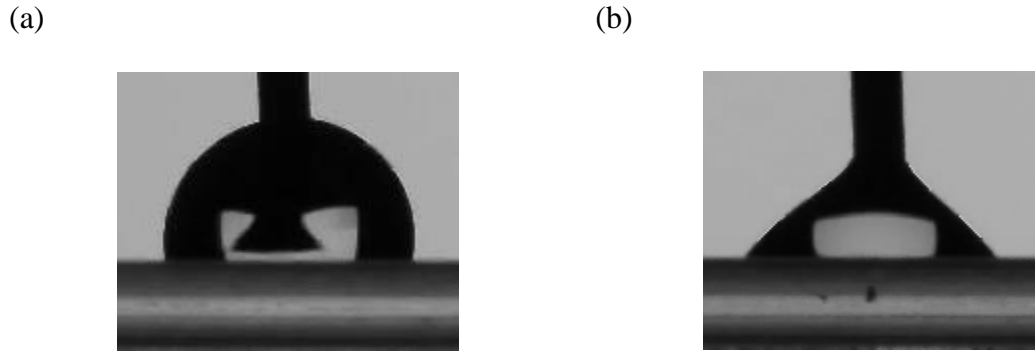


Figure 6.6: (a) Advancing, and (b) receding contact angle images for  $\text{H}_2\text{O}$  on  $\text{C}_9\text{H}_{20}$  saturated surfaces.

Uncertainties due to local variations in the transducer thickness, interfacial condition, and signal noise contribute to data scattering. The standard deviation of the frequency dependent phase response is obtained by taking three measurements at different locations in a triangular pattern for each sample, as described in Section 5.3.1, three data sets for each location, and each data point in a data set is the 1000 times average of the phase lag data points measured at each frequency. In addition, the effects of convection and prolonged heating were examined. We verified that convection and the steady temperature rise of the sample did not affect the data, by using verification methods for FDTR measurements with liquids according literature [117].

### 6.3.2 Effect of $\text{C}_9\text{H}_{20}$ interlayer has on effective Au- $\text{H}_2\text{O}$ TBC using AMM

Figure 6.7 shows the average energy transmission at each excitation frequency calculated using Eq. (6.1) and (6.2). The longitudinal, and transverse Debye frequency of Au listed in Table 5.1 are used as cutoff frequencies for the respective modes. The cutoff frequencies used resulted in the proposed model being bounded by the elastic and inelastic models due to the assumption of the Debye frequency of the softer and harder medium in the respective models presented by Merabia *et al.* [170].

The transmission results indicate that  $\Gamma_{12} \ll \Gamma_{23}$  in general, this is due to the acoustic properties of the physisorbed layer being much more similar to H<sub>2</sub>O than to Au. This means that the effective transmission is significantly reduced as the transmission is largely restricted by the Au-C<sub>9</sub>H<sub>20</sub> interface. The results indicates that the effective transmission is greatly affected by the heavily reduced contribution by the longitudinal mode, when accounting the allowable incident angles at the C<sub>9</sub>H<sub>20</sub>-H<sub>2</sub>O interface after the Au-C<sub>9</sub>H<sub>20</sub> interface.

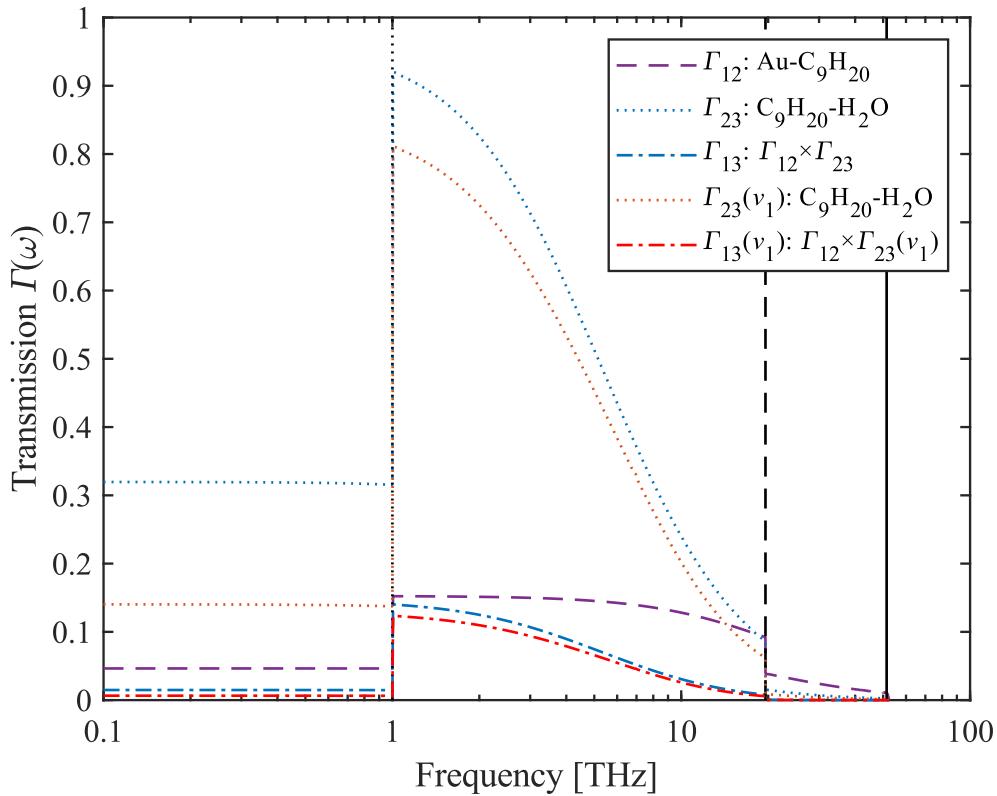
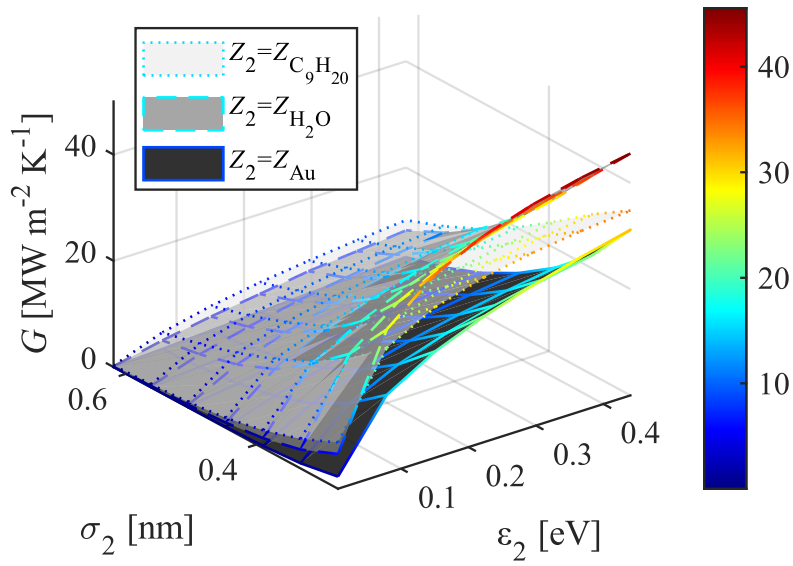


Figure 6.7: Average transmission at Au-C<sub>9</sub>H<sub>20</sub> interfaces; exit angle independent, and dependent average transmission at C<sub>9</sub>H<sub>20</sub>-H<sub>2</sub>O, and effective Au-C<sub>9</sub>H<sub>20</sub>-H<sub>2</sub>O interfaces, respectively. The dotted, dashed, and solid black line marks the Frenkel frequency of the H<sub>2</sub>O, Au transverse cutoff frequency, and Au longitudinal cutoff frequency, respectively.

Theoretical results for the effective TBC were expressed in terms of the LJ potential parameters and acoustic impedance of the physisorbed intermediate layer, as there we can see how artificially varying the properties of the intermediate layer can affect the results.

Figure 6.8 shows surface plots of the effective TBC at Au-H<sub>2</sub>O interfaces having variable LJ potential parameters bounded by the materials involved for the selected acoustic impedance, while maintaining the properties of materials 1 and 3 constant. Note that the phonon DOS was allowed to be described by Debye approximation for comparison purposes, as the Debye model is also often used for its simplicity. The effect of using more sophisticated approximations such as the Born-von Karman model can be found elsewhere [63], [198]. Here we also allowed this model to be partially inelastic, by taking  $\omega_{c,j} = \omega_{c,1,j}$ , and we used the elastic and inelastic limits to define the lower and upper bounds of the prediction, respectively.

(a)



(b)

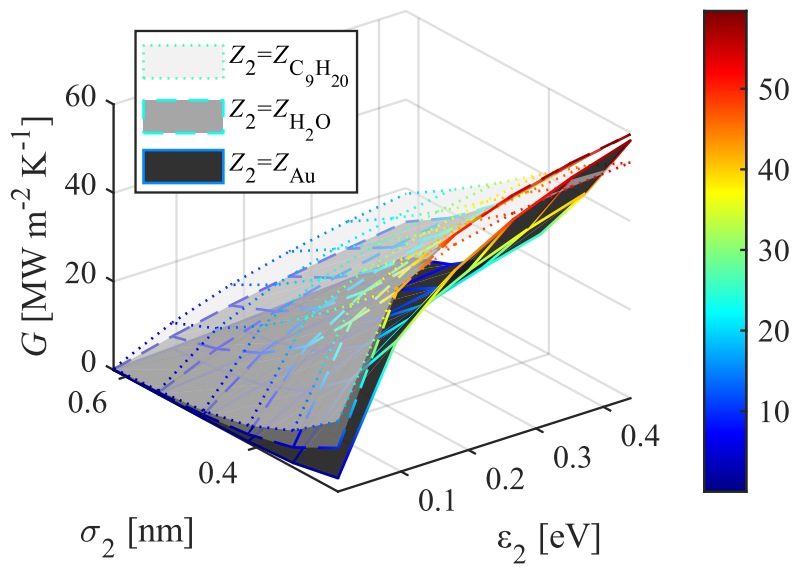


Figure 6.8: Overall TBC as a function of the intermediate layer's Lennard-Jones potential parameters with selected acoustic impedances using (a) Debye frequencies of the solid, and (b) Debye frequencies of the harder medium as defined in Section 5.2.3.

Prior to the thermoreflectance measurements, we measured the contact angle,  $\theta_{ca}$ , using the sessile drop technique, as described in Section 3.5, for both bare Au and Au with the  $C_9H_{20}$  film. We determined the dimensionless work of adhesion to be 1.766 and 1, respectively. This means that the surface of the bare Au is more hydrophilic than the sample with a nonane film. According to the literature [13], [157]–[159] and our previous investigation [185], we should expect  $G_{Au-C_9H_{20}-H_2O} > G_{Au-H_2O} / 2$  based on the work of adhesion with surface tension of  $\gamma_l = 72 \text{ mJ m}^{-2}$ .

Figure 6.9 shows the effective TBC across Au to water, with and without nonane using our AMM calculations and FDTR measurements. As expected, the experimental result for the Au- $H_2O$  system is comparable to the analytical result obtained using the AMM developed by Merabia *et al.* [170]. More importantly, the theoretical result using the proposed model is relatively consistent compared the experimental result for the Au- $C_9H_{20}$ - $H_2O$  system. The relative discrepancies between the two structures may be understood based on what we observed in Figure 6.8, larger separation distance or/and smaller bonding energy of a physisorbed layer like  $C_9H_{20}$  leads to significantly softer spring stiffness, which hinders phonon propagation most on the solid side. The results suggests that the relatively large  $\sigma$  of  $C_9H_{20}$  heavily contributes to the overall TBC reduction.

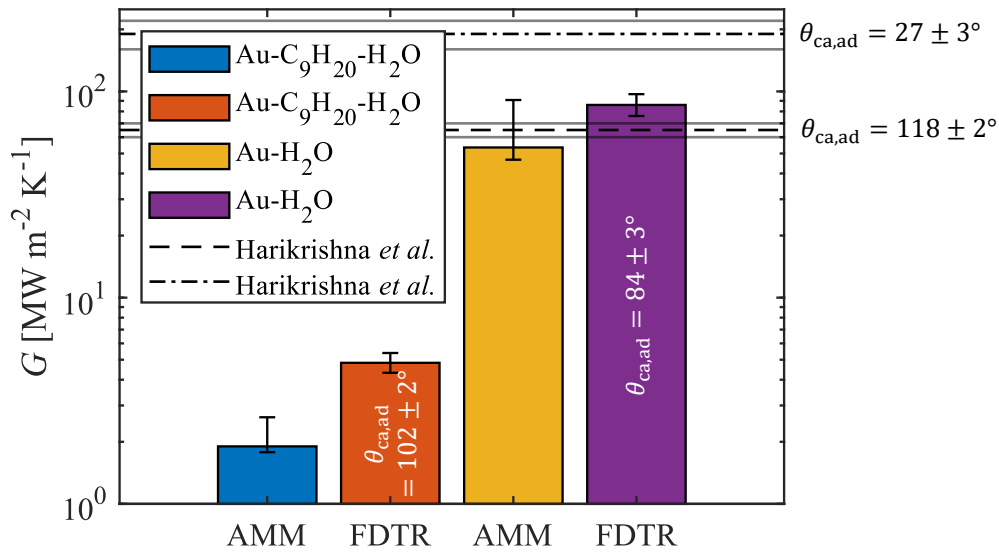


Figure 6.9: AMM predictions and FDTR measurements of the effective Au-C<sub>9</sub>H<sub>20</sub>-H<sub>2</sub>O and Au-H<sub>2</sub>O TBC, respectively. The lower and upper bounds of the AMM predictions are calculated using the elastic and inelastic limits, respectively; while for FDTR, two-sigma standard deviations are presented using the Monte Carlo method described in Section 3.6.6. The dashed and dash-dotted lines are experimental data of Au-H<sub>2</sub>O with near-superhydrophobic using CH<sub>3</sub> terminated SAM and near-superhydrophilic using COOH terminated SAM surfaces, respectively, reported by Harikrishna *et al.* [157].

### 6.3.3 Sensitivity in measuring Au-C<sub>9</sub>H<sub>20</sub> TBC using FDTR

For completeness, we measured and predicted the Au-C<sub>9</sub>H<sub>20</sub> TBC to be  $0.61 \pm 0.07 \text{ MW m}^{-2} \text{ K}^{-1}$  and  $7.9 \text{ MW m}^{-2} \text{ K}^{-1}$  using FDTR and AMM, respectively [II]. Although both experimental and theoretical results both indicate a significant drop in the TBC from H<sub>2</sub>O to C<sub>9</sub>H<sub>20</sub> on well-prepared bare Au surfaces, an order of magnitude difference is observed. This could be due to the inherent limited capability of the analytical model, or lack of sensitivity of the FDTR measurements, or both. Figure 6.10 shows the sensitivity to the H<sub>2</sub>O and C<sub>9</sub>H<sub>20</sub> thermal conductivity and the Au-H<sub>2</sub>O and Au-C<sub>9</sub>H<sub>20</sub> TBC, respectively. The sensitivity analysis indicates that the current FDTR technique is inadequate in measuring the more common fluorinated fluids typically used in thermal applications (i.e., Novec, Galden, Genetron, etc.) as they are dielectric and typically have very low thermal effusivity.

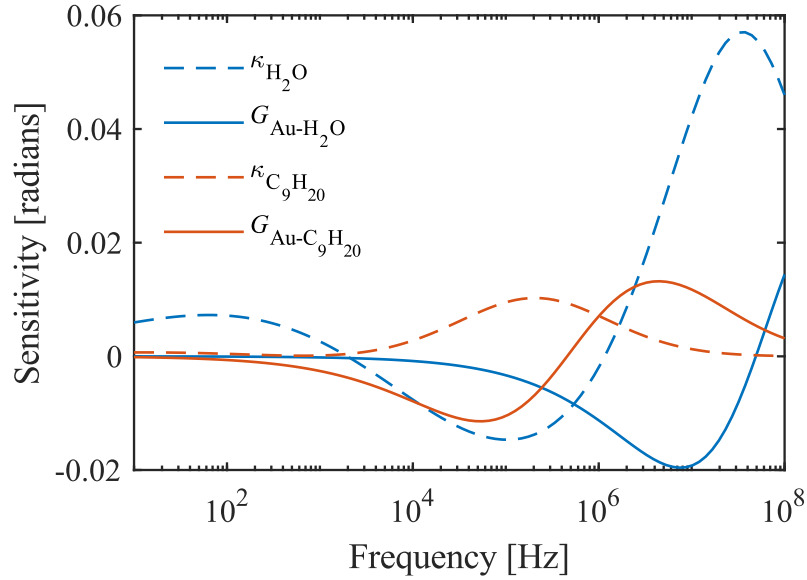


Figure 6.10: Theoretical sensitivity to the thermal conductivity, and TBC were calculated using Eq. (3.47) based on the measured values for the  $\text{SiO}_2\text{-Au-H}_2\text{O-SiO}_2$  and  $\text{SiO}_2\text{-Au-C}_9\text{H}_{20}\text{-SiO}_2$  liquid cells, respectively.

Considering if the heat flow to the working fluid from the heat source (i.e, transducer) is limited by the low thermal effusivity of the liquid, the bidirectional heat transfer may be more balanced by reducing the support substrate thermal effusivity. Figure 6.11 shows that the TBC sensitivity is greatly enhanced when the support substrate thermal effusivity is artificially reduced to 10% of the bulk value. The enhancement scaled better for the lower thermal effusivity as it may be constrained by the radial heating of the transducer layer. To reduce the radial heating contribution, a confined geometry of the transducer layer may be applied and used, with measured FDTR data and finite element element-based numerical fitting to solve for the unknown thermal parameters [118]. However, this may not always be feasible, so a more general unconfined geometry solution may be worth exploring.

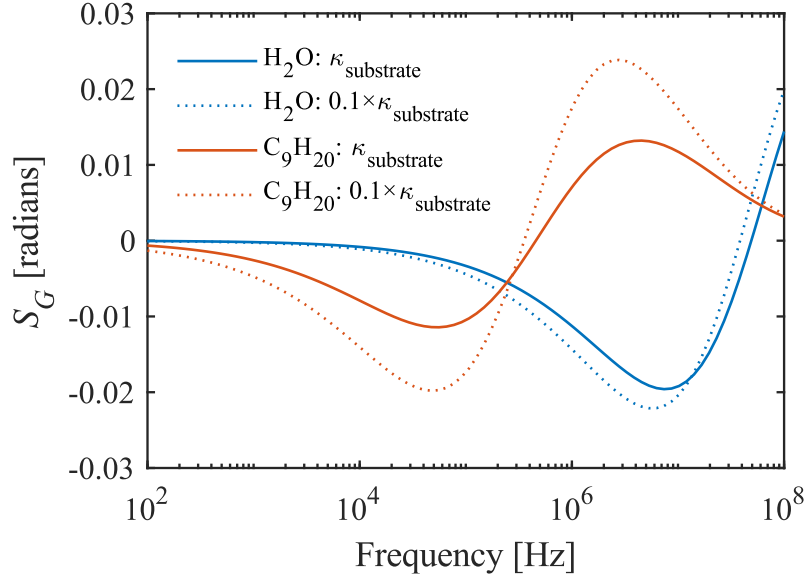


Figure 6.11: Sensitivity plot for TBC, where the dotted lines refers to the sensitivity of Au-H<sub>2</sub>O TBC, and Au-C<sub>9</sub>H<sub>20</sub> TBC when the support substrate (i.e., SiO<sub>2</sub>) thermal conductivity is artificially reduced to 10% of the bulk value, respectively.

## 6.4 Conclusions

In this chapter, we presented an analytical model to predict the effective TBC across solid-liquid interface when a physisorbed layer is present on a solid surface. We showed that the analytical predictions are comparable to the experimental measurements for the Au-C<sub>9</sub>H<sub>20</sub>-H<sub>2</sub>O and Au-H<sub>2</sub>O systems. The FDTR and contact angle data for Au-water is consistent with the literature [13], [157], [185].

The effective TBC that we determined for Au-nonane-water are one order of magnitude smaller than expected. This indicates that if a physisorbed layer is present, understanding the nature of the bonding mechanism between the solid and such species is necessary to accurately predict the effective TBC. However, the results suggests that the bonding strength between a given physisorbed layer and a solid also plays a significant role in phonon transport of such systems.



While we acknowledge that the model assumes complete specularly and does not consider electron-phonon coupling processes. We have shown that surface energy alone may be not enough to accurately predict interfacial heat transport for real systems. This means that when using surface energy to determine the bonding strength between a solid and a liquid, one should determine if a chemi- or physisorbed layer is present, and if it is present, the type of bond, bonding strength, and properties of the intermediate layer in question should be examined and considered for more accurate effective interfacial thermal transport predictions.

Finally, we investigated the sensitivity of Au-C<sub>9</sub>H<sub>20</sub> TBC since the thermal conductivity of C<sub>9</sub>H<sub>20</sub> is an order of magnitude smaller than that of H<sub>2</sub>O. The sensitivity analysis results indicate that the standard FDTR transducer platform is inadequate in measuring TBC with the more common fluorinated fluids typically used in thermal applications. We presented a thermorefectance enhancement method that can be achieved without confined geometry of the transducer layer, making this solution a more general thermorefectance enhancement solution.

The work related to the need to enhance thermorefectance measurement sensitivity for measuring low thermal effusivity fluids presented in this chapter has been presented at the Intersociety Conference on Thermal and Thermomechanical Phenomena in Electronic Systems, *San Diego* [II], while the remaining work presented in this chapter has been submitted to AIP Applied Physics Letters [I].

## Chapter 7.

### Conclusions

Thermal transport in thin films and across interfaces of dissimilar phase materials is key to emerging electronic and photonic devices with integrated microscale solutions. Frequency-domain thermoreflectance (FDTR) is a powerful technique for experimental investigation of heat transfer mechanisms in integrated microscale solutions such as thin film thermoelectrics, microfluidics, and two-phase evaporators. This thesis demonstrates the importance of rigorous experimental characterisation on thermal transport in thin films, makes contributions toward improving the FDTR technique for characterising interfacial thermal properties of dissimilar phase materials, and extends the capabilities of the acoustic mismatch model to better understand and predict how phonons transport across solid-liquid interfaces with physisorbed surfaces.

#### 7.1 Summary of the thesis

In the first part of the thesis, the thermal properties of electrodeposited n-type thin film thermoelectric material in a microscale thermoelectric cooler ( $\mu$ TEC) developed in Tyndall Institute, University College Cork were measured using the FDTR technique to aid the overall thermoelectric performance characterisation. We reported the highest thermoelectric figure of merit of  $0.26 \pm 0.04$  for electrodeposited n-type  $\text{Bi}_2\text{Te}_3$  film where all electrical and thermal parameters are measured experimentally. Using kinetic theory and values measured using the FDTR, we concluded that no size effect should be in play as the electrodeposited  $\text{Bi}_2\text{Te}_3$  film thickness in the  $\mu$ TEC is much greater than the mean free path. Using a basic diffuse mismatch model, we showed that interfacial thermal transport should

not meaningfully impact the overall device performance under the normal operating temperature range.

In the second part of the thesis, we sought to better understand the effect of wettability on thermal transport across solid-liquid interfaces using self-assembled monolayer (SAMs). We showed that interfacial thermal transport across Au-H<sub>2</sub>O interfaces only trends with the thermodynamic work of adhesion for a well-prepared surface, and that the effective Au-H<sub>2</sub>O interfacial thermal resistance is greatly dependent on surface conditions. However, using FDTR, we concluded that the SAM chain length does not play an important role in the overall thermal resistance of solid-SAM-liquid structures.

In the third and final part of the thesis, we investigated the effect of contamination from physisorption due to ambient exposure on thermal transport across solid-liquid interfaces, by using a controlled physisorbed species, nonane (C<sub>9</sub>H<sub>20</sub>). Using FDTR, we showed that a C<sub>9</sub>H<sub>20</sub> interlayer has strong and consistent influence over the effective Au-H<sub>2</sub>O interfacial thermal resistance. We observed an interfacial thermal resistance more than twice as large as the most hydrophilic case from the literature. An acoustic mismatch model (AMM) was developed to aid the investigation and we found that the bonding potential energy of the interlayer plays a dominating role in the effective interfacial transport. This means that solid-liquid interfacial thermal transport calculations of real single- or two-phase microscale heat exchangers cannot simply rely on the thermodynamic work of adhesion.

## **7.2 Outlook for future work**

### **7.2.1 Enhancing TR measurement sensitivity**

Enhancing the sensitivity of thermoreflectance measurements expands the capability to measure materials with more extreme thermal properties, such as fluorinated fluids for

thermal applications. These engineered fluids are typically dielectrics and have very low effusivity, with thermal conductivity values in the same order as air ( $0.025 \text{ W m}^{-1} \text{ K}^{-1}$ ). In Chapter 5, we showed that reducing the substrate thermal conductivity could enhance the sensitivity as it forces a more balanced bidirectional heat transfer from the heat source (i.e., thermoreflectance transducer). Warzoha [118] demonstrated that confining the transducer geometry can enhance thermal transport across the interface. This is due to the heat being unable to diffuse beyond the boundary. We can use this effect by introducing a thermal barrier layer between the transducer and the substrate of the multilayered structure, as shown in Figure 5.4(a). We investigated the sensitivity of a commonly used Genetron R-245fa refrigerant in two-phase evaporators [40], and showed that, theoretically, an aerogel thermal barrier layer could greatly enhance the thermoreflectance sensitivity, as shown in Figure 7.1. Therefore, advancement on this topic could further expand the thermal characterisation capability of FDTR and TDTR techniques.

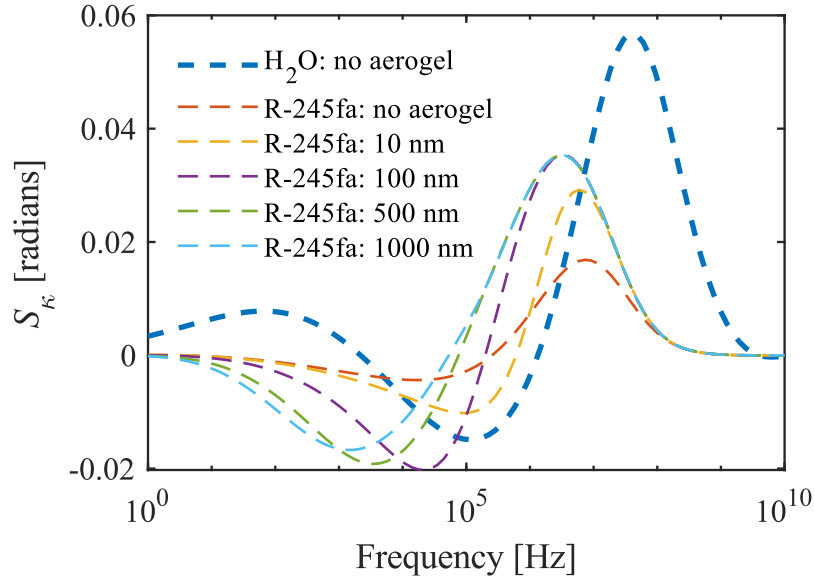


Figure 7.1: Sensitivity plot for working fluid thermal conductivity with structure  $\text{SiO}_2\text{-Au-H}_2\text{O-SiO}_2$ ,  $\text{SiO}_2\text{-Au-245fa-SiO}_2$ , and  $\text{SiO}_2\text{-aerogel-Au-245fa-SiO}_2$  with aerogel thickness 10 nm, 100 nm, 500 nm, and 1000 nm, respectively. Theoretical sensitivity to the thermal conductivities were calculated using Eq. (3.47) based on the measured values. The thermal conductivity value used for R-245fa is  $0.88 \text{ W m}^{-1} \text{ K}^{-1}$  which is taken from the product data sheet [199].

### 7.2.2 Temperature- and pressure-controlled FDTR measurements

The FDTR technique has proven to be a useful non-invasive method in thermal characterisation of thin films and across interfaces of dissimilar materials. More advanced studies can be done using the FDTR technique, especially when it comes to non-atmospheric pressure conditions. The time-domain thermoreflectance (TDTR) technique has demonstrated that thin film thermal conductivity and thermal boundary conductance across solid-solid interfaces can be measured as a function of temperature [200]–[204]. Although in theory, FDTR should also be capable in doing the same, but it has yet to be tested. However, both FDTR and TDTR have yet to demonstrate the capability to measure thermal conductivity and thermal boundary conductance (TBC) across solid-solid or solid-liquid interfaces as a function of pressure.

Figure 7.2 shows a mini environmental chamber<sup>1</sup> designed to experimentally characterise and test the thermal properties and performance of 3D die stacked architectures, and  $\mu$ TEC devices, respectively. This chamber is designed such that it is compatible with common optical tables, specifically our optical table and our FDTR system. This setup will allow us to measure thermal properties as a function temperature and pressure to better understand the thermal performance of novel microscale thermal management designs.

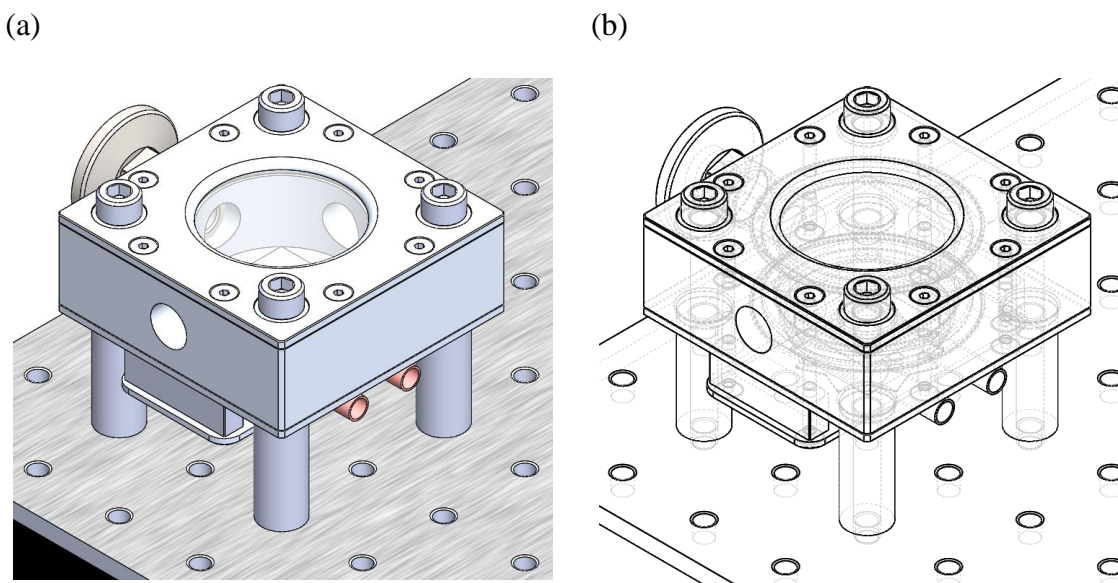


Figure 7.2: (a) Solid, and (b) wireframe view of the mini environmental chamber designed using SolidWorks to experimentally characterise and test the thermal properties and performance of 3D die stacked architectures, respectively.

This work could also potentially be used to experimentally verify the ability for AMM to predict TBC as a function of pressure, as Prasher [59] showed that pressure may be included in the AMM if the surface traction force per area,  $\mathbb{T}_{LJ}$ , under static pressure,  $p$ ,

---

<sup>1</sup> Unfortunately, due to COVID-19, we were unable to source all the necessary components to finish the experimental part of this work within the timeframe.

is considered, then  $T_{LJ}(z, \rho)$  is given by [186] (see Appendix A for the form without the pressure term)

$$T_{LJ}(z, \rho) = \frac{8\Delta\gamma}{3z_0} \left( \left( \frac{z_0}{z} \right)^3 - \left( \frac{z_0}{z} \right)^9 \right) + \rho. \quad (7.1)$$

Eq. (7.1) can then directly influence the phonon transmission probability term in Eq. (5.7) through the modified spring constant,  $K'_{12}$ , and  $K'_{12}$  is then given by

$$K'_{12} = \left( \frac{\partial T_{LJ}(z, \rho)}{\partial z} \right)_{z=z'_0}, \quad (7.2)$$

where  $z'_0$  is the equilibrium separation distance under static pressure.

### 7.2.3 Liquid-vapour, and steady state studies using FDTR

More recently, Mehrvand and Putnam [205] showed that the TDTR technique can be used to quantify the effective TBC during a bubble ebullition cycle in a microchannel as shown in Figure 7.3. Details of the liquid cell sample and TDTR setup from their transient two-phase heat transport study can be found elsewhere [205], [206]. Figure 7.4(a)-(e) illustrate each stage of the ebullition cycle of a single vapor bubble due to laser induced heating. Although essentially all stages of the ebullition cycle contribute to the enhancement of the overall heat transfer coefficient, the majority of the heat is carried away through latent heat of evaporation of a thin liquid layer over the heat source. This dominates heat dissipation through sensible heat by mixing of the liquid near the low-pressure region as the vapor bubble quenches and detach from the surface.

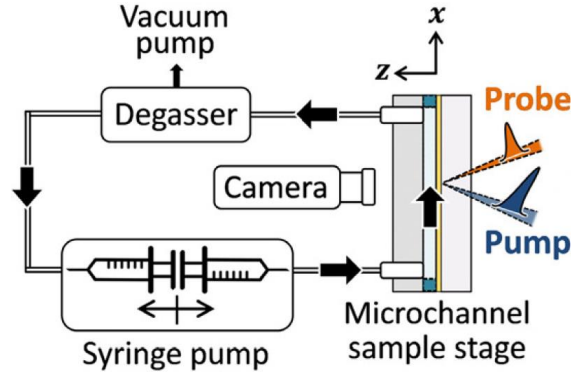


Figure 7.3: Schematic illustration of a syringe pump-based microchannel flow loop. Taken from literature [206].

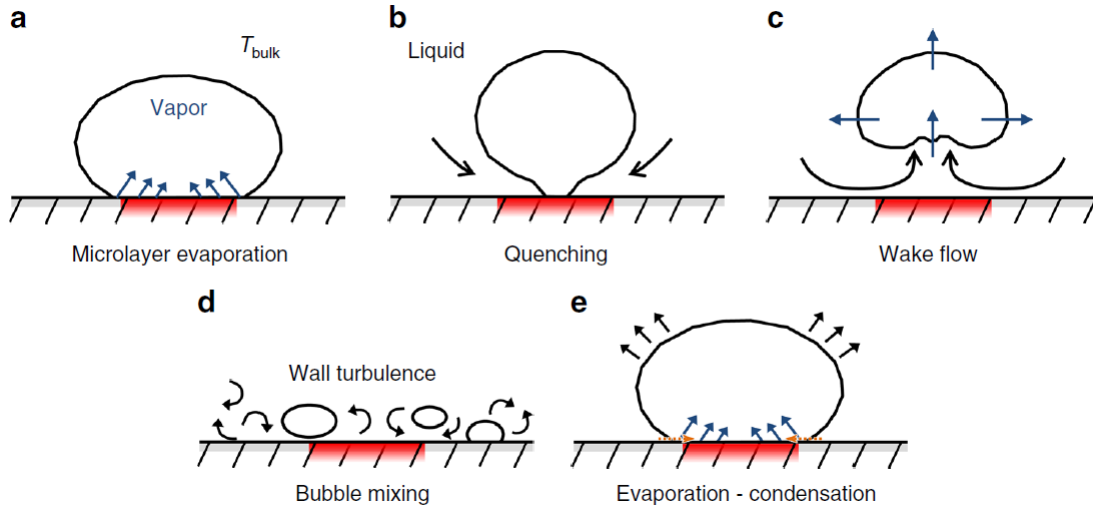


Figure 7.4: An illustration each stage of the ebullition cycle of a single vapor microbubble due to laser induced heating. Taken from literature [205].

A more detailed experimental study on the stage, as shown in Figure 7.4(a) can be done through a steady state approach. We could potentially extract the effective liquid-vapor TBC,  $G_{\text{eff}}$ , if we define  $G_{\text{eff}}$  as

$$G_{\text{eff}}^{-1} = G_{sl}^{-1} - G_{lv}^{-1}, \quad (7.3)$$

where  $G_{sl}$  and  $G_{lv}$  are the solid-liquid TBC and liquid-vapor TBC, respectively. As a proof of concept, we fabricated the liquid cell shown in Figure 7.5. To prevent drying out, a superhydrophilic surface was used by forming  $\text{Al}_2\text{O}_3$  nanostructures using the hot water



treatment method on a 50 nm aluminium (Al) thin film surface [207]. Recalling the relationship between the change in reflectivity and temperature described in Eq. (3.12), we can see that the amplitude of the FDTR phase lag signal is directly proportional the temperature rise. Using this fact, we demonstrated that at a given modulation frequency, the FDTR is sensitive to a drop in temperature rise when a vapor bubble is formed and maintained, as shown in Figure 7.6. However, experimentally measuring the effective TBC across the solid-vapor interface with a thin liquid film in between using the FDTR, is non-trivial. The effect of natural and Marangoni flow about the vapor bubble, and the evaporation and condensation with a vapor bubble have been widely investigated, and may be understood analytically [208]. However, the frequency dependence on the amplitude signal, the chaotic nature of laser induced vapor bubbles, and potential dewetting due to laser induced heating makes this type of measurement extremely challenging. With the recent development of analysing FDTR data of structured surfaces [118], more robust materials may be deployed to form the necessary wicking surfaces. The FDTR technique is a promising in-situ steady state and local two-phase heat transport characterisation method.

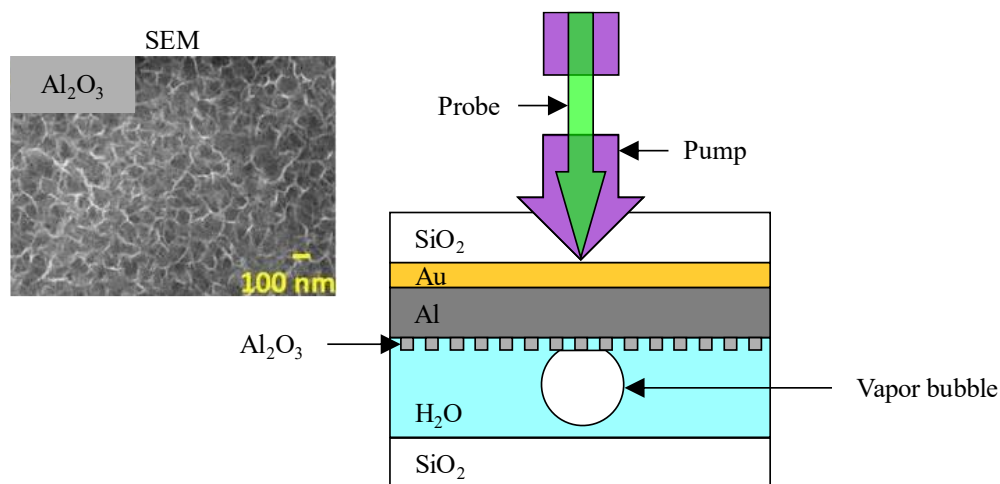


Figure 7.5: Schematic of multilayered liquid cell sample structure with  $\text{Al}_2\text{O}_3$  nanostructured superhydrophilic surface along with a SEM image of the  $\text{Al}_2\text{O}_3$  surface morphology.

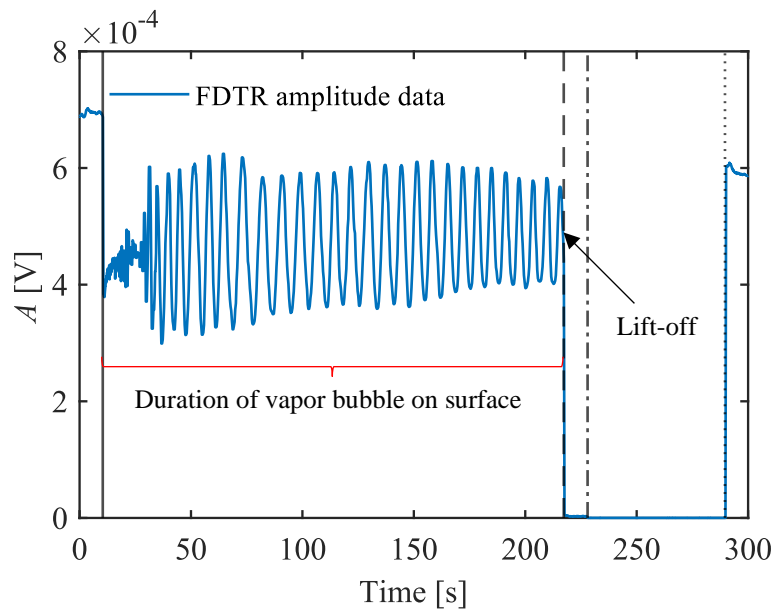


Figure 7.6: A temperature rise observation plot using the FDTR, where the solid, dashed, dash-dotted and dotted lines represent the instance for nucleation point, pump laser off, probe laser off and both lasers on, respectively. The amplitude difference between the starting point and ending point is due to dewetting from excessive power used to stimulate nucleation.

# Appendix A

## Derivation of adhesion energy from surface traction

We reproduce the derivation of [186] for the adhesion energy by starting with the surface traction force per area,  $\mathbb{T}_{\text{LJ}}$ , due to the Lennard-Jones (LJ) potential [77],

$$U_{\text{LJ}}(r) = 4\varepsilon \left( \left( \frac{\sigma}{r} \right)^{12} - \left( \frac{\sigma}{r} \right)^6 \right), \quad (\text{A.1})$$

The interaction in the  $-z$  direction is given by [186]

$$\mathbb{T}_{\text{LJ}}(z) = \frac{2\pi\rho_{N,1}\rho_{N,2}\varepsilon\sigma^6(15z^6 - 2\sigma^6)}{45z^9}. \quad (\text{A.2})$$

Here,  $\varepsilon$  is the depth of the potential well of the LJ potential,  $r$  is the distance between the centre of the particles,  $\sigma$  is the distance at  $U_{\text{LJ}}(r) = 0$ ,  $\rho_{N,i}$  is the number density for material  $i$ . The number density is calculated by  $\rho_N = \rho N_A / M_u$ , where  $\rho$  is the mass density,  $N_A$  is the Avogadro constant, and  $M_u$  is the molar mass which is the mass of the substance per number of moles of the substance. Recall the definition of Hamaker constant,  $C_H$ , where  $C_H$  is given by [94]

$$C_H = 4\varepsilon\pi^2\rho_{N,1}\rho_{N,2}\sigma^6. \quad (\text{A.3})$$

Using Eq. (A.3), Eq. (A.2) could be rewritten as

$$\mathbb{T}_{\text{LJ}}(z) = \frac{C_H}{6\pi z^3} - \frac{C_H\sigma^6}{45\pi z^9}. \quad (\text{A.4})$$

When  $\mathbb{T}_{\text{LJ}}(z) = 0$ , the two surfaces have an equilibrium distance  $z_0$ , where  $z_0$  is given by

$$z_0 = \left(\frac{2}{15}\right)^{1/6} \sigma \quad (\text{A.5})$$

Using Eq. (A.5), Eq. (A.4) could be rewritten as

$$\mathbb{T}_{\text{LJ}}(z) = \frac{C_{\text{H}}}{6\pi z_0^3} \left( \left(\frac{z_0}{z}\right)^3 - \left(\frac{z_0}{z}\right)^9 \right). \quad (\text{A.6})$$

Finally, by considering the adhesion energy,  $\Delta\gamma$ , being the work done moving the two surfaces from equilibrium position,  $z = z_0$ , to infinity,  $z = \infty$ , we get

$$\Delta\gamma = \int_{z_0}^{\infty} \mathbb{T}_{\text{LJ}}(z) dz = \frac{C_{\text{H}}}{16\pi z_0^2}. \quad (\text{A.7})$$

## References

- [1] R. Wang, J. Qian, T. Wei, and H. Huang, "Integrated closed cooling system for high-power chips," *Case Stud. Therm. Eng.*, vol. 26, p. 100954, Aug. 2021, doi: 10.1016/j.csite.2021.100954.
- [2] N. H. Naquiuddin, L. H. Saw, M. C. Yew, F. Yusof, T. C. Ng, and M. K. Yew, "Overview of micro-channel design for high heat flux application," *Renewable and Sustainable Energy Reviews*. 2018. doi: 10.1016/j.rser.2017.09.110.
- [3] S. A. Wirdatmadja, D. Moltchanov, S. Balasubramaniam, and Y. Koucheryavy, "Microfluidic System Protocols for Integrated On-Chip Communications and Cooling," *IEEE Access*, 2017, doi: 10.1109/ACCESS.2017.2662798.
- [4] S. Lal, D. Gautam, and K. M. Razeeb, "Fabrication of micro-thermoelectric devices for power generation and the thermal management of photonic devices," *J. Micromechanics Microengineering*, 2019, doi: 10.1088/1361-6439/ab18f1.
- [5] X. Meng, J. Zhu, X. Wei, and Y. Yan, "Natural convection heat transfer of a straight-fin heat sink," *Int. J. Heat Mass Transf.*, 2018, doi: 10.1016/j.ijheatmasstransfer.2018.03.002.
- [6] S. Zeng, B. Kanargi, and P. S. Lee, "Experimental and numerical investigation of a mini channel forced air heat sink designed by topology optimization," *Int. J. Heat Mass Transf.*, vol. 121, pp. 663–679, Jun. 2018, doi: 10.1016/j.ijheatmasstransfer.2018.01.039.
- [7] V. Guruviah, "Design of microheaters with better thermal management for sensor applications," *Int. J. Mech. Eng. Technol.*, vol. 8, no. 10, 2017.
- [8] Y. Yu, W. Zhu, X. Kong, Y. Wang, P. Zhu, and Y. Deng, "Recent development and application of thin-film thermoelectric cooler," *Front. Chem. Sci. Eng.*, vol. 14, no. 4, pp. 492–503, Aug. 2020, doi: 10.1007/s11705-019-1829-9.
- [9] Y. Qiu, W. Hu, C. Wu, and W. Chen, "An Experimental Study of Microchannel and Micro-Pin-Fin Based On-Chip Cooling Systems with Silicon-to-Silicon Direct Bonding," *Sensors*, vol. 20, no. 19, p. 5533, Sep. 2020, doi: 10.3390/s20195533.
- [10] D. F. Hanks *et al.*, "Nanoporous membrane device for ultra high heat flux thermal management," *Microsystems Nanoeng.*, vol. 4, no. 1, p. 1, Dec. 2018, doi: 10.1038/s41378-018-0004-7.
- [11] X.-H. Yang and J. Liu, "Advances in Liquid Metal Science and Technology in Chip Cooling and Thermal Management," in *Advances in Heat Transfer*, 2018, pp. 187–300. doi: 10.1016/bs.aiht.2018.07.002.
- [12] W. D. Nix, "Mechanical properties of thin films," *Metall. Trans. A*, vol. 20, no. 11, pp. 2217–2245, Nov. 1989, doi: 10.1007/BF02666659.

- [13] Z. Ge, D. G. Cahill, and P. V. Braun, “Thermal conductance of hydrophilic and hydrophobic interfaces,” *Phys. Rev. Lett.*, vol. 96, no. 18, p. 186101, 2006, doi: 10.1103/PhysRevLett.96.186101.
- [14] E. T. Swartz and R. O. Pohl, “Thermal boundary resistance,” *Rev. Mod. Phys.*, vol. 61, no. 3, pp. 605–668, 1989, doi: 10.1103/RevModPhys.61.605.
- [15] E. T. Ritz and N. A. Benedek, “Understanding mechanisms of thermal expansion in complex oxide thin-films from first principles: Role of high-order phonon-strain anharmonicity,” *J. Appl. Phys.*, 2021, doi: 10.1063/5.0068321.
- [16] X. Wang and B. Huang, “Computational Study of In-Plane Phonon Transport in Si Thin Films,” *Sci. Rep.*, vol. 4, no. 1, p. 6399, Dec. 2014, doi: 10.1038/srep06399.
- [17] T. Ahn, J. Kang, J. J. Jeong, and B. Yun, “Measurement of local wall temperature and heat flux using the two-thermocouple method for a heat transfer tube,” *Nucl. Eng. Technol.*, vol. 51, no. 7, pp. 1853–1859, Oct. 2019, doi: 10.1016/j.net.2019.05.007.
- [18] J. Zhu, D. Tang, W. Wang, J. Liu, K. W. Holub, and R. Yang, “Ultrafast thermoreflectance techniques for measuring thermal conductivity and interface thermal conductance of thin films,” *J. Appl. Phys.*, 2010, doi: 10.1063/1.3504213.
- [19] H. Amano *et al.*, “The 2018 GaN power electronics roadmap,” *Journal of Physics D: Applied Physics*. 2018. doi: 10.1088/1361-6463/aaaf9d.
- [20] A. C. Liu *et al.*, “The evolution of manufacturing technology for gan electronic devices,” *Micromachines*. 2021. doi: 10.3390/mi12070737.
- [21] S. Sudhindra, F. Kargar, and A. A. Balandin, “Noncured graphene thermal interface materials for high-power electronics: Minimizing the thermal contact resistance,” *Nanomaterials*, 2021, doi: 10.3390/nano11071699.
- [22] R. Sun *et al.*, “A Novel Concept Methodology of In-direct Cold Plate Liquid Cooling Design for Data Center in CPU Socket Area,” in *2020 19th IEEE Intersociety Conference on Thermal and Thermomechanical Phenomena in Electronic Systems (ITherm)*, Jul. 2020, pp. 471–421. doi: 10.1109/ITherm45881.2020.9190567.
- [23] S. I. Guggari, “Analysis of Thermal Performance Metrics—Application to CPU Cooling in HPC Servers,” *IEEE Trans. Components, Packag. Manuf. Technol.*, vol. 11, no. 2, pp. 222–232, Feb. 2021, doi: 10.1109/TCPMT.2020.3029940.
- [24] R. van Erp, R. Soleimanzadeh, L. Nela, G. Kampitsis, and E. Matioli, “Co-designing electronics with microfluidics for more sustainable cooling,” *Nature*, 2020, doi: 10.1038/s41586-020-2666-1.
- [25] Y. Yu, Y. Yin, Y. Li, M. Li, and J. Song, “Thermal Analysis on Active Heat Dissipation Design with Embedded Flow Channels for Flexible Electronic Devices,” *Micromachines*, vol. 12, no. 10, p. 1165, Sep. 2021, doi: 10.3390/mi12101165.
- [26] T. L. Bergman, A. S. Lavine, F. P. Incropera, and D. P. DeWitt, *Introduction to Heat*

*Transfer*, 6th ed. John Wiley & Sons, 2011.

- [27] F. Ahmed, Y. Yoshida, J. Wang, K. Sakai, and T. Kiwa, "Design and validation of microfluidic parameters of a microfluidic chip using fluid dynamics," *AIP Adv.*, 2021, doi: 10.1063/5.0056597.
- [28] J. Kim, J. Kim, Y. Shin, and Y. Yoon, "A study on the fabrication of an RTD (resistance temperature detector) by using Pt thin film," *Korean J. Chem. Eng.*, vol. 18, no. 1, pp. 61–66, Jan. 2001, doi: 10.1007/BF02707199.
- [29] H. Y. Zhang, Y. C. Mui, and M. Tarin, "Analysis of thermoelectric cooler performance for high power electronic packages," *Appl. Therm. Eng.*, 2010, doi: 10.1016/j.applthermaleng.2009.10.020.
- [30] S. B. Riffat and X. Ma, "Improving the coefficient of performance of thermoelectric cooling systems: A review," *Int. J. Energy Res.*, 2004, doi: 10.1002/er.991.
- [31] B. Yang, H. Ahuja, and T. Tran, "Review Article: Thermoelectric Technology Assessment: Application to Air Conditioning and Refrigeration," *HVAC&R Res.*, vol. 14, no. 5, pp. 635–653, Sep. 2008, doi: 10.1080/10789669.2008.10391031.
- [32] R. Enright *et al.*, "A Vision for Thermally Integrated Photonics Systems," *Bell Labs Tech. J.*, vol. 19, pp. 31–45, 2014, doi: 10.15325/BLTJ.2014.2364431.
- [33] V. A. Drebuschak, "The Peltier effect," *J. Therm. Anal. Calorim.*, vol. 91, no. 1, pp. 311–315, Jan. 2008, doi: 10.1007/s10973-007-8336-9.
- [34] M. Siahmargoi, N. Rahbar, H. Kargarsharifabad, S. E. Sadati, and A. Asadi, "An Experimental Study on the Performance Evaluation and Thermodynamic Modeling of a Thermoelectric Cooler Combined with Two Heatsinks," *Sci. Rep.*, 2019, doi: 10.1038/s41598-019-56672-9.
- [35] D. M. Rowe, *Thermoelectrics handbook: macro to nano*. CRC Press, 2005.
- [36] Laird Technologies, "Thin Film Thermoelectric Handbook," 2012. [https://www.mouser.com/pdfDocs/Laird\\_ThinFilmThermoelectricHandbook.pdf](https://www.mouser.com/pdfDocs/Laird_ThinFilmThermoelectricHandbook.pdf)
- [37] D. Pellicone, "Passive and active two-phase cooling for power electronics applications," in *PCIM Europe 2017 - International Exhibition and Conference for Power Electronics, Intelligent Motion, Renewable Energy and Energy Management*, 2017, pp. 1–15. doi: 10.1109/SBMicro.2017.7990819.
- [38] C. H. Hoang *et al.*, "A Review of Recent Developments in Pumped Two-Phase Cooling Technologies for Electronic Devices," *IEEE Trans. Components, Packag. Manuf. Technol.*, 2021, doi: 10.1109/TCPMT.2021.3117572.
- [39] D. F. Hanks *et al.*, "Nanoporous evaporative device for advanced electronics thermal management," in *Thermomechanical Phenomena in Electronic Systems -Proceedings of the Intersociety Conference*, 2014, pp. 290–295. doi: 10.1109/ITHERM.2014.6892295.

- [40] D. F. Hanks *et al.*, “High heat flux evaporation of low surface tension liquids from nanoporous membranes,” *ACS Appl. Mater. Interfaces*, 2020, doi: 10.1021/acsami.9b20520.
- [41] M. Bongarala, H. Hu, J. A. Weibel, and S. V. Garimella, “A figure of merit to characterize the efficacy of evaporation from porous microstructured surfaces,” *Int. J. Heat Mass Transf.*, vol. 182, p. 121964, Jan. 2022, doi: 10.1016/j.ijheatmasstransfer.2021.121964.
- [42] S. A. Khrapak and A. G. Khrapak, “Minima of shear viscosity and thermal conductivity coefficients of classical fluids,” *Phys. Fluids*, vol. 34, no. 2, p. 027102, Feb. 2022, doi: 10.1063/5.0082465.
- [43] K. Trachenko and V. V. Brazhkin, “Minimal quantum viscosity from fundamental physical constants,” *Sci. Adv.*, vol. 6, no. 17, Apr. 2020, doi: 10.1126/sciadv.aba3747.
- [44] T. M. Tritt, *Thermal Conductivity*, 1st ed. Springer US, 2004. doi: 10.1007/b136496.
- [45] G. Chen, *Nanoscale Energy Transport and Harvesting*. Oxford University Press, New York, 2015. doi: 10.1201/b15658.
- [46] J. Ravichandran *et al.*, “Crossover from incoherent to coherent phonon scattering in epitaxial oxide superlattices,” *Nat. Mater.*, vol. 13, no. 2, pp. 168–172, 2014, doi: 10.1038/nmat3826.
- [47] B. T. Wong and M. P. Mengüç, “Transport Equations,” in *Thermal Transport for Applications in Micro/Nanomachining*, 1st ed., Springer, 2008, pp. 15–56. doi: 10.1007/978-3-540-73607-3\_2.
- [48] K. Modi, *Thermal energy at the nanoscale*, vol. 56, no. 2. World Scientific, 2015. doi: 10.1080/00107514.2014.999710.
- [49] C. Kittel, *Introduction to Solid State Physics*, 8th ed. Wiley, 2004. [Online]. Available: <http://www.wiley.com/WileyCDA/WileyTitle/productCd-EHEP000803.html>
- [50] M. Bayle, N. Combe, N. M. Sangeetha, G. Viau, and R. Carles, “Vibrational and electronic excitations in gold nanocrystals,” *Nanoscale*, vol. 6, no. 15, pp. 9157–9165, 2014, doi: 10.1039/c4nr02185a.
- [51] J. W. Lynn, H. G. Smith, and R. M. Nicklow, “Lattice dynamics of gold,” *Phys. Rev. B*, vol. 8, no. 8, pp. 3493–3499, Oct. 1973, doi: 10.1103/PhysRevB.8.3493.
- [52] P. L. Kapitza, “Heat transfer and superfluidity of helium II,” *Phys. Rev.*, vol. 60, no. 4, pp. 354–355, 1941, doi: 10.1103/PhysRev.60.354.
- [53] B. N. J. Persson, A. I. Volokitin, and H. Ueba, “Phononic heat transfer across an interface: Thermal boundary resistance,” *J. Phys. Condens. Matter*, vol. 23, no. 4, 2011, doi: 10.1088/0953-8984/23/4/045009.



- [54] D. G. Cahill, "Analysis of heat flow in layered structures for time-domain thermoreflectance," *Rev. Sci. Instrum.*, vol. 75, no. 12, pp. 5119–5122, 2004, doi: 10.1063/1.1819431.
- [55] J. C. Duda *et al.*, "On the assumption of detailed balance in prediction of diffusive transmission probability during interfacial transport," *Nanoscale Microscale Thermophys. Eng.*, vol. 14, no. 1, pp. 21–33, 2010, doi: 10.1080/15567260903530379.
- [56] W. A. Little, "the Transport of Heat Between Dissimilar Solids At Low Temperatures," *Can. J. Phys.*, vol. 37, no. 3, pp. 334–349, 1959, doi: 10.1139/p59-037.
- [57] R. S. Prasher and P. E. Phelan, "A scattering-mediated acoustic mismatch model for the prediction of thermal boundary resistance," *J. Heat Transfer*, vol. 123, no. 1, pp. 105–112, 2001, doi: 10.1115/1.1338138.
- [58] R. Prasher, "Acoustic mismatch model for thermal contact resistance of van der Waals contacts," *Appl. Phys. Lett.*, vol. 94, no. 4, 2009, doi: 10.1063/1.3075065.
- [59] R. Prasher, "Acoustic Mismatch Model for Thermal Contact Conductance of Van Der Waals Contacts Under Static Force," *Nanoscale Microscale Thermophys. Eng.*, vol. 22, no. 1, pp. 1–5, Jan. 2018, doi: 10.1080/15567265.2017.1391905.
- [60] H. K. Lyo and D. G. Cahill, "Thermal conductance of interfaces between highly dissimilar materials," *Phys. Rev. B - Condens. Matter Mater. Phys.*, vol. 73, no. 14, 2006, doi: 10.1103/PhysRevB.73.144301.
- [61] R. J. Stoner and H. J. Maris, "Kapitza conductance and heat flow between solids at temperatures from 50 to 300 K," *Phys. Rev. B*, vol. 48, no. 22, pp. 16373–16387, 1993, doi: 10.1103/PhysRevB.48.16373.
- [62] T. E. Beechem Iii, P. E. Hopkins, J. C. Duda, and P. M. Norris, "On the Role of Optical Phonons in Thermal Boundary Conductance," Albuquerque, 2011. [Online]. Available: <https://www.osti.gov/servlets/purl/1106997>
- [63] P. Reddy, K. Castelino, and A. Majumdar, "Diffuse mismatch model of thermal boundary conductance using exact phonon dispersion," *Appl. Phys. Lett.*, vol. 87, no. 21, pp. 1–3, 2005, doi: 10.1063/1.2133890.
- [64] T. Beechem, S. Graham, P. Hopkins, and P. Norris, "Role of interface disorder on thermal boundary conductance using a virtual crystal approach," *Appl. Phys. Lett.*, vol. 90, no. 5, p. 054104, Jan. 2007, doi: 10.1063/1.2437685.
- [65] P. E. Hopkins, L. M. Phinney, J. R. Serrano, and T. E. Beechem, "Effects of surface roughness and oxide layer on the thermal boundary conductance at aluminum/silicon interfaces," *Phys. Rev. B*, vol. 82, no. 8, p. 085307, Aug. 2010, doi: 10.1103/PhysRevB.82.085307.
- [66] Q. Song and G. Chen, "Evaluation of the diffuse mismatch model for phonon

scattering at disordered interfaces,” *Phys. Rev. B*, vol. 104, no. 8, p. 085310, Aug. 2021, doi: 10.1103/PhysRevB.104.085310.

- [67] N. Erdman, D. C. Bell, and R. Reichelt, “Scanning Electron Microscopy,” in *Springer Handbooks*, 2019, pp. 229–318. doi: 10.1007/978-3-030-00069-1\_5.
- [68] M. M. Freundlich, “Origin of the Electron Microscope,” *Science (80-. )*, vol. 142, no. 3589, pp. 185–188, Oct. 1963, doi: 10.1126/science.142.3589.185.
- [69] C.-O. A. Olsson, S. E. Hrnstrm, and S. Hogmark, “Auger electron spectroscopy,” in *Surface Characterization*, Weinheim, Germany: Wiley-VCH Verlag GmbH, 2007, pp. 272–288. doi: 10.1002/9783527612451.ch17.
- [70] J. Goldstein *et al.*, *Scanning Electron Microscopy and X-ray Microanalysis*, 3rd ed. Springer US, 2003.
- [71] Y. Sakai, T. Yamada, T. Suzuki, and T. Ichinokawa, “Contrast mechanisms of secondary electron images in scanning electron and ion microscopy,” *Appl. Surf. Sci.*, vol. 144–145, pp. 96–100, Apr. 1999, doi: 10.1016/S0169-4332(98)00773-9.
- [72] G. Binnig, C. F. Quate, and C. Gerber, “Atomic Force Microscope,” *Phys. Rev. Lett.*, vol. 56, no. 9, pp. 930–933, Mar. 1986, doi: 10.1103/PhysRevLett.56.930.
- [73] P. Parot *et al.*, “Past, present and future of atomic force microscopy in life sciences and medicine,” *J. Mol. Recognit.*, vol. 20, no. 6, pp. 418–431, Nov. 2007, doi: 10.1002/jmr.857.
- [74] O. Marti, B. Drake, and P. K. Hansma, “Atomic force microscopy of liquid-covered surfaces: Atomic resolution images,” *Appl. Phys. Lett.*, vol. 51, no. 7, pp. 484–486, Aug. 1987, doi: 10.1063/1.98374.
- [75] L. O. Otieno, B. O. Alunda, J. Kim, and Y. J. Lee, “Design and Fabrication of a High-Speed Atomic Force Microscope Scan-Head,” *Sensors*, vol. 21, no. 2, p. 362, Jan. 2021, doi: 10.3390/s21020362.
- [76] M. Marrese, V. Guarino, and L. Ambrosio, “Atomic Force Microscopy: A Powerful Tool to Address Scaffold Design in Tissue Engineering,” *J. Funct. Biomater.*, vol. 8, no. 1, p. 7, Feb. 2017, doi: 10.3390/jfb8010007.
- [77] J. E. Jones, “On the determination of molecular fields. —II. From the equation of state of a gas,” *Proc. R. Soc. London. Ser. A, Contain. Pap. a Math. Phys. Character*, vol. 106, no. 738, pp. 463–477, Oct. 1924, doi: 10.1098/rspa.1924.0082.
- [78] F. Wenner, “A method of measuring earth resistivity,” *Bull. Bur. Stand.*, vol. 12, no. 4, p. 469, May 1916, doi: 10.6028/bulletin.282.
- [79] L. Valdes, “Resistivity Measurements on Germanium for Transistors,” *Proc. IRE*, vol. 42, no. 2, pp. 420–427, Feb. 1954, doi: 10.1109/JRPROC.1954.274680.
- [80] K. Ilse, T. Tänzer, C. Hagendorf, and M. Turek, “Geometrical correction factors for

- finite-size probe tips in microscopic four-point-probe resistivity measurements,” *J. Appl. Phys.*, vol. 116, no. 22, p. 224509, Dec. 2014, doi: 10.1063/1.4903964.
- [81] N. Wakeham, A. F. Bangura, X. Xu, J.-F. Mercure, M. Greenblatt, and N. E. Hussey, “Gross violation of the Wiedemann–Franz law in a quasi-one-dimensional conductor,” *Nat. Commun.*, vol. 2, no. 1, p. 396, Sep. 2011, doi: 10.1038/ncomms1406.
- [82] P. A. Bespalov and O. N. Savina, “Generalized Wiedemann-Franz law and temperature jump in space plasmas with ion-acoustic turbulence,” *Mon. Not. R. Astron. Soc. Lett.*, vol. 382, no. 1, pp. L63–L66, Nov. 2007, doi: 10.1111/j.1745-3933.2007.00389.x.
- [83] I. Miccoli, F. Edler, H. Pfnür, and C. Tegenkamp, “The 100th anniversary of the four-point probe technique: the role of probe geometries in isotropic and anisotropic systems,” *J. Phys. Condens. Matter*, vol. 27, no. 22, p. 223201, Jun. 2015, doi: 10.1088/0953-8984/27/22/223201.
- [84] F. M. Smits, “Measurement of Sheet Resistivities with the Four-Point Probe,” *Bell Syst. Tech. J.*, vol. 37, no. 3, pp. 711–718, May 1958, doi: 10.1002/j.1538-7305.1958.tb03883.x.
- [85] H. Topsoe, “Geometric factors in four point resistivity measurement,” *Bulletin*, 1968. <http://www.four-point-probes.com/haldor.html>
- [86] R. H. Cox and H. Strack, “Ohmic contacts for GaAs devices,” *Solid. State. Electron.*, vol. 10, no. 12, pp. 1213–1218, Dec. 1967, doi: 10.1016/0038-1101(67)90063-9.
- [87] C. Clegg, “History of the ramé-hart Goniometer,” *Ramé-Hart Instrument Company*, 2007. [http://www.ramehart.com/newsletters/2007-12\\_news.htm](http://www.ramehart.com/newsletters/2007-12_news.htm)
- [88] E. G. SHAFRIN and W. A. ZISMAN, “Upper Limits to the Contact Angles of Liquids on Solids,” 1964, pp. 145–157. doi: 10.1021/ba-1964-0043.ch009.
- [89] M. Vuckovac, M. Latikka, K. Liu, T. Huhtamäki, and R. H. A. Ras, “Uncertainties in contact angle goniometry,” *Soft Matter*, vol. 15, no. 35, pp. 7089–7096, 2019, doi: 10.1039/C9SM01221D.
- [90] Y.-L. Hung, Y.-Y. Chang, M.-J. Wang, and S.-Y. Lin, “A simple method for measuring the superhydrophobic contact angle with high accuracy,” *Rev. Sci. Instrum.*, vol. 81, no. 6, p. 065105, Jun. 2010, doi: 10.1063/1.3449325.
- [91] S. Y. Lin, H. C. Chang, L. W. Lin, and P. Y. Huang, “Measurement of dynamic/advancing/receding contact angle by video-enhanced sessile drop tensiometry,” *Rev. Sci. Instrum.*, 1996, doi: 10.1063/1.1147117.
- [92] F. K. Skinner, Y. Rotenberg, and A. W. Neumann, “Contact angle measurements from the contact diameter of sessile drops by means of a modified axisymmetric drop shape analysis,” *J. Colloid Interface Sci.*, vol. 130, no. 1, pp. 25–34, Jun. 1989, doi: 10.1016/0021-9797(89)90074-X.

- [93] C. Huh and R. L. Reed, “A method for estimating interfacial tensions and contact angles from sessile and pendant drop shapes,” *J. Colloid Interface Sci.*, 1983, doi: 10.1016/0021-9797(83)90361-2.
- [94] J. N. Israelachvili, *Intermolecular and Surface Forces*, 3rd ed. Elsevier, 2011. doi: 10.1016/C2011-0-05119-0.
- [95] A. J. Schmidt, R. Cheaito, and M. Chiesa, “A frequency-domain thermorefectance method for the characterization of thermal properties,” *Rev. Sci. Instrum.*, vol. 80, no. 9, p. 094901, Sep. 2009, doi: 10.1063/1.3212673.
- [96] P. Jiang, X. Qian, and R. Yang, “Tutorial: Time-domain thermorefectance (TDTR) for thermal property characterization of bulk and thin film materials,” *J. Appl. Phys.*, vol. 124, no. 16, p. 161103, Oct. 2018, doi: 10.1063/1.5046944.
- [97] A. J. Schmidt, R. Cheaito, and M. Chiesa, “Characterization of thin metal films via frequency-domain thermorefectance,” *J. Appl. Phys.*, vol. 107, no. 2, p. 024908, Jan. 2010, doi: 10.1063/1.3289907.
- [98] K. T. Regner, D. P. Sellan, Z. Su, C. H. Amon, A. J. H. McGaughey, and J. A. Malen, “Broadband phonon mean free path contributions to thermal conductivity measured using frequency domain thermorefectance,” *Nat. Commun.*, 2013, doi: 10.1038/ncomms2630.
- [99] J. Yang, C. Maragliano, and A. J. Schmidt, “Thermal property microscopy with frequency domain thermorefectance,” *Rev. Sci. Instrum.*, vol. 84, no. 10, p. 104904, Oct. 2013, doi: 10.1063/1.4824143.
- [100] J. Christofferson and A. Shakouri, “Thermorefectance based thermal microscope,” *Rev. Sci. Instrum.*, vol. 76, no. 2, p. 024903, Feb. 2005, doi: 10.1063/1.1850632.
- [101] E. Colavita, A. Franciosi, C. Mariani, and R. Rosei, “Thermorefectance test of W, Mo, and paramagnetic Cr band structures,” *Phys. Rev. B*, vol. 27, no. 8, pp. 4684–4693, Apr. 1983, doi: 10.1103/PhysRevB.27.4684.
- [102] R. Rosei, E. Colavita, A. Franciosi, J. H. Weaver, and D. T. Peterson, “Electronic structure of the bcc transition metals: Thermorefectance studies of bulk V, Nb, Ta, and  $\alpha$ TaHx,” *Phys. Rev. B*, vol. 21, no. 8, pp. 3152–3157, Apr. 1980, doi: 10.1103/PhysRevB.21.3152.
- [103] R. Rosei and D. W. Lynch, “Thermomodulation Spectra of Al, Au, and Cu,” *Phys. Rev. B*, vol. 5, no. 10, pp. 3883–3894, May 1972, doi: 10.1103/PhysRevB.5.3883.
- [104] W. J. Scouler, “Temperature-Modulated Reflectance of Gold from 2 to 10 eV,” *Phys. Rev. Lett.*, vol. 18, no. 12, pp. 445–448, Mar. 1967, doi: 10.1103/PhysRevLett.18.445.
- [105] R. B. Wilson, B. A. Apgar, L. W. Martin, and D. G. Cahill, “Thermorefectance of metal transducers for optical pump-probe studies of thermal properties,” *Opt. Express*, vol. 20, no. 27, p. 28829, 2012, doi: 10.1364/oe.20.028829.

- [106] E. Hecht, *Optics*, 5th ed. Harlow: Pearson Education, 2017. [Online]. Available: [https://edisciplinas.usp.br/pluginfile.php/5054148/mod\\_resource/content/1/Hecht-optics-5ed.pdf](https://edisciplinas.usp.br/pluginfile.php/5054148/mod_resource/content/1/Hecht-optics-5ed.pdf)
- [107] A. Yoshida and T. Asakura, “A simple technique for quickly measuring the spot size of Gaussian laser beams,” *Opt. Laser Technol.*, vol. 8, no. 6, pp. 273–274, 1976, doi: 10.1016/0030-3992(76)90042-6.
- [108] Y. Suzaki and A. Tachibana, “Measurement of the  $\mu\text{m}$  sized radius of Gaussian laser beam using the scanning knife-edge,” *Appl. Opt.*, vol. 14, no. 12, p. 2809, 1975, doi: 10.1364/ao.14.002809.
- [109] F. Moisy, “Ezyfit toolbox for Matlab.” 2022. [Online]. Available: <https://www.mathworks.com/matlabcentral/fileexchange/10176-ezyfit-2-44>
- [110] R. Cheaito, C. S. Gorham, A. Misra, K. Hattar, and P. E. Hopkins, “Thermal conductivity measurements via time-domain thermoreflectance for the characterization of radiation induced damage,” *J. Mater. Res.*, vol. 30, no. 9, pp. 1403–1412, 2015, doi: 10.1557/jmr.2015.11.
- [111] D. S. Katzer and M. Cardona, “Thermal-conductivity measurements of GaAs/AlAs superlattices using a picosecond optical pump-and-probe technique,” *Phys. Rev. B - Condens. Matter Mater. Phys.*, vol. 59, no. 12, pp. 8105–8113, 1999, doi: 10.1103/PhysRevB.59.8105.
- [112] D. G. Cahill *et al.*, “Nanoscale thermal transport. II. 2003-2012,” *Appl. Phys. Rev.*, vol. 1, no. 1, p. 011305, 2014, doi: 10.1063/1.4832615.
- [113] S. D. Brorson, J. G. Fujimoto, and E. P. Ippen, “Femtosecond electronic heat-transport dynamics in thin gold films,” *Phys. Rev. Lett.*, vol. 59, no. 17, pp. 1962–1965, 1987, doi: 10.1103/PhysRevLett.59.1962.
- [114] Z. Li, U. Brand, and T. Ahbe, “Step height measurement of microscale thermoplastic polymer specimens using contact stylus profilometry,” *Precis. Eng.*, vol. 45, pp. 110–117, Jul. 2016, doi: 10.1016/j.precisioneng.2016.02.001.
- [115] A. J. Schmidt, “Optical Characterization of Thermal Transport from the Nanoscale to the Macroscale,” PhD thesis, Massachusetts Institute of Technology, 2008. [Online]. Available: <https://dspace.mit.edu/handle/1721.1/44798>
- [116] D. Rodin and S. K. Yee, “Simultaneous measurement of in-plane and through-plane thermal conductivity using beam-offset frequency domain thermoreflectance,” *Rev. Sci. Instrum.*, 2017, doi: 10.1063/1.4973297.
- [117] A. Schmidt, M. Chiesa, X. Chen, and G. Chen, “An optical pump-probe technique for measuring the thermal conductivity of liquids,” *Rev. Sci. Instrum.*, vol. 79, no. 6, p. 064902, 2008, doi: 10.1063/1.2937458.
- [118] R. J. Warzoha *et al.*, “A numerical fitting routine for frequency-domain thermoreflectance measurements of nanoscale material systems having arbitrary

- geometries,” *J. Appl. Phys.*, vol. 129, no. 3, p. 035103, Jan. 2021, doi: 10.1063/5.0030168.
- [119] L. Tang and C. Dames, “Anisotropic thermal conductivity tensor measurements using beam-offset frequency domain thermoreflectance (BO-FDTR) for materials lacking in-plane symmetry,” *Int. J. Heat Mass Transf.*, vol. 164, p. 120600, Jan. 2021, doi: 10.1016/j.ijheatmasstransfer.2020.120600.
- [120] H. S. Carslow and J. C. Jaeger, *Conduction Of Heat In Solids*, 2nd ed. Oxford University Press, New York, 1986.
- [121] J. B. J. Fourier, *The Analytical Theory of Heat*. Cambridge University Press, 2009. doi: 10.1017/CBO9780511693205.
- [122] T. L. Bergman, A. S. Lavine, F. P. Incropera, and D. P. DeWitt, *Fundamentals of Heat and Mass Transfer*, 8th ed. Wiley, 2018.
- [123] R. Cheaito, “The Role of Size Effects on the Thermal Conductivity of Thin Film Alloys and Superlattices,” PhD thesis, University of Virginia, 2015.
- [124] A. J. Schmidt, X. Chen, and G. Chen, “Pulse accumulation, radial heat conduction, and anisotropic thermal conductivity in pump-probe transient thermoreflectance,” *Rev. Sci. Instrum.*, vol. 79, no. 11, 2008, doi: 10.1063/1.3006335.
- [125] T. Beechem, L. Yates, and S. Graham, “Error and uncertainty in Raman thermal conductivity measurements,” *Rev. Sci. Instrum.*, vol. 86, no. 4, p. 041101, Apr. 2015, doi: 10.1063/1.4918623.
- [126] C. Jeong, S. Datta, and M. Lundstrom, “Thermal conductivity of bulk and thin-film silicon: A Landauer approach,” *J. Appl. Phys.*, vol. 111, no. 9, p. 093708, May 2012, doi: 10.1063/1.4710993.
- [127] J. Yang, E. Ziade, and A. J. Schmidt, “Uncertainty analysis of thermoreflectance measurements,” *Rev. Sci. Instrum.*, vol. 87, no. 1, p. 014901, Jan. 2016, doi: 10.1063/1.4939671.
- [128] R. Coleman, N. L. Johnson, S. Kotz, and N. Balakrishnan, “Continuous Univariate Distributions,” *J. R. Stat. Soc. Ser. A (Statistics Soc.)*, vol. 159, no. 2, p. 349, 1996, doi: 10.2307/2983186.
- [129] R. Kumar and R. Singh, *Thermoelectricity and Advanced Thermoelectric Materials*. Elsevier, 2021. doi: 10.1016/C2019-0-01167-3.
- [130] D. Beretta *et al.*, “Thermoelectrics: From history, a window to the future,” *Mater. Sci. Eng. R Reports*, vol. 138, p. 100501, Oct. 2019, doi: 10.1016/j.mser.2018.09.001.
- [131] P.-H. Kao, P.-J. Shih, C.-L. Dai, and M.-C. Liu, “Fabrication and Characterization of CMOS-MEMS Thermoelectric Micro Generators,” *Sensors*, vol. 10, no. 2, pp. 1315–1325, Feb. 2010, doi: 10.3390/s100201315.

- [132] M. S. Dresselhaus *et al.*, “New directions for low-dimensional thermoelectric materials,” *Adv. Mater.*, vol. 19, no. 8, pp. 1043–1053, 2007, doi: 10.1002/adma.200600527.
- [133] H. J. Goldsmid, *Thermoelectric Refrigeration*. Plenum Press, New York, 1964. doi: 10.1007/978-1-4899-5723-8.
- [134] L. Song, J. Zhang, and B. B. Iversen, “Enhanced thermoelectric properties of SnSe thin films grown by single-target magnetron sputtering,” *J. Mater. Chem. A*, vol. 7, no. 30, pp. 17981–17986, 2019, doi: 10.1039/c9ta03252e.
- [135] T. H. Chen, P. Y. Lin, H. C. Chang, and C. H. Chen, “Enhanced thermoelectricity of three-dimensionally mesostructured  $\text{Bi}_x\text{Sb}_{2-x}\text{Te}_3$  nanoassemblies: From micro-scaled open gaps to isolated sealed mesopores,” *Nanoscale*, vol. 9, no. 9, pp. 3283–3292, 2017, doi: 10.1039/c7nr00132k.
- [136] K. Mahmood *et al.*, “Investigation of the optimal annealing temperature for the enhanced thermoelectric properties of MOCVD-grown ZnO films,” *J. Exp. Theor. Phys.*, vol. 124, no. 4, pp. 580–583, 2017, doi: 10.1134/S1063776117040045.
- [137] I. Malik, T. Srivastava, K. K. Surthi, C. Gayner, and K. K. Kar, “Enhanced thermoelectric performance of n-type  $\text{Bi}_2\text{Te}_3$  alloyed with low cost and highly abundant sulfur,” *Mater. Chem. Phys.*, vol. 255, p. 123598, Nov. 2020, doi: 10.1016/j.matchemphys.2020.123598.
- [138] Y. Du, J. Li, J. Xu, and P. Eklund, “Thermoelectric Properties of Reduced Graphene Oxide/ $\text{Bi}_2\text{Te}_3$  Nanocomposites,” *Energies*, vol. 12, no. 12, p. 2430, Jun. 2019, doi: 10.3390/en12122430.
- [139] S. Corbett, “Applications of CCD-Thermoreflectance to Thin Film Thermoelectric Characterisation,” PhD thesis, Trinity College Dublin, 2021.
- [140] S. Corbett *et al.*, “Electrodeposited Thin-Film Micro-Thermoelectric Coolers with Extreme Heat Flux Handling and Microsecond Time Response,” *ACS Appl. Mater. Interfaces*, vol. 13, no. 1, pp. 1773–1782, 2021, doi: 10.1021/acsami.0c16614.
- [141] C. V. Manzano, B. Abad, and M. Martín-González, “The Effect of Electrolyte Impurities on the Thermoelectric Properties of Electrodeposited  $\text{Bi}_2\text{Te}_3$  Films,” *J. Electrochem. Soc.*, vol. 165, no. 14, pp. D768–D773, Nov. 2018, doi: 10.1149/2.1131814jes.
- [142] A. Zhou, W. Wang, B. Yang, J. Li, and Q. Zhao, “Thermal conductivity study of micrometer-thick thermoelectric films by using three-omega methods,” *Appl. Therm. Eng.*, vol. 98, pp. 683–689, Apr. 2016, doi: 10.1016/j.applthermaleng.2015.12.145.
- [143] A. Zhou *et al.*, “Enhancing the Thermoelectric Properties of the Electroplated  $\text{Bi}_2\text{Te}_3$  Films by Tuning the Pulse Off-to-on Ratio,” *Electrochim. Acta*, 2015, doi: 10.1016/j.electacta.2015.07.164.
- [144] G. Li *et al.*, “Integrated microthermoelectric coolers with rapid response time and

high device reliability,” *Nat. Electron.*, 2018, doi: 10.1038/s41928-018-0148-3.

- [145] C. L. Chen *et al.*, “Fabrication and characterization of electrodeposited bismuth telluride films and nanowires,” *J. Phys. Chem. C*, 2010, doi: 10.1021/jp909926z.
- [146] G. Chen, *Nanoscale Energy Transport and Conversion: A Parallel Treatment of Electrons, Molecules, Phonons, and Photons*. Oxford University Press, New York, 2005.
- [147] O. Hellman and D. A. Broido, “Phonon thermal transport in Bi<sub>2</sub>Te<sub>3</sub> from first principles,” *Phys. Rev. B*, vol. 90, no. 13, p. 134309, Oct. 2014, doi: 10.1103/PhysRevB.90.134309.
- [148] L. D. Hicks and M. S. Dresselhaus, “Thermoelectric figure of merit of a one-dimensional conductor,” *Phys. Rev. B*, 1993, doi: 10.1103/PhysRevB.47.16631.
- [149] D. Zheng, S. Tanaka, K. Miyazaki, and M. Takashiri, “Evaluation of Specific Heat, Sound Velocity and Lattice Thermal Conductivity of Strained Nanocrystalline Bismuth Antimony Telluride Thin Films,” *J. Electron. Mater.*, vol. 44, no. 6, pp. 1679–1687, Jun. 2015, doi: 10.1007/s11664-014-3518-2.
- [150] P. E. Hopkins, J. L. Kassebaum, and P. M. Norris, “Effects of electron scattering at metal-nonmetal interfaces on electron-phonon equilibration in gold films,” *J. Appl. Phys.*, 2009, doi: 10.1063/1.3068476.
- [151] Z. Tian, K. Esfarjani, and G. Chen, “Enhancing phonon transmission across a Si/Ge interface by atomic roughness: First-principles study with the Green’s function method,” *Phys. Rev. B - Condens. Matter Mater. Phys.*, 2012, doi: 10.1103/PhysRevB.86.235304.
- [152] W. Zhang, T. S. Fisher, and N. Mingo, “Simulation of interfacial phonon transport in Si-Ge heterostructures using an atomistic green’s function method,” *J. Heat Transfer*, 2007, doi: 10.1115/1.2709656.
- [153] W. Zhang, T. S. Fisher, and N. Mingo, “The Atomistic Green’s Function Method: An Efficient Simulation Approach for Nanoscale Phonon Transport,” *Numer. Heat Transf. Part B Fundam.*, vol. 51, no. 4, pp. 333–349, Mar. 2007, doi: 10.1080/10407790601144755.
- [154] A. Jacquot, B. Bayer, M. Winkler, and M. Jaegle, “Coupled theoretical interpretation and experimental investigation of the lattice thermal conductivity of Bi<sub>2</sub>Te<sub>3</sub> single crystal,” in *AIP Conference Proceedings*, 2012, pp. 61–64. doi: 10.1063/1.4731497.
- [155] J. R. Rumble, T. J. Bruno, and M. J. . Doa, *CRC Handbook of Chemistry and Physics*, 102nd ed. CRC Press, 2021.
- [156] Z. Tian, A. Marconnet, and G. Chen, “Enhancing solid-liquid interface thermal transport using self-assembled monolayers,” *Appl. Phys. Lett.*, vol. 106, no. 21, p. 211602, 2015, doi: 10.1063/1.4921758.



- [157] H. Harikrishna, W. A. Ducker, and S. T. Huxtable, “The influence of interface bonding on thermal transport through solid-liquid interfaces,” *Appl. Phys. Lett.*, vol. 102, no. 25, p. 251606, 2013, doi: 10.1063/1.4812749.
- [158] H. Acharya, N. J. Mozdzierz, P. Keblinski, and S. Garde, “How chemistry, nanoscale roughness, and the direction of heat flow affect thermal conductance of solid-water interfaces,” *Ind. Eng. Chem. Res.*, vol. 51, no. 4, pp. 1767–1773, 2012, doi: 10.1021/ie2010274.
- [159] N. Shenogina, R. Godawat, P. Keblinski, and S. Garde, “How wetting and adhesion affect thermal conductance of a range of hydrophobic to hydrophilic aqueous interfaces,” *Phys. Rev. Lett.*, vol. 102, no. 15, p. 156101, 2009, doi: 10.1103/PhysRevLett.102.156101.
- [160] R. G. Pearson, “Absolute electronegativity and absolute hardness of Lewis acids and bases,” *J. Am. Chem. Soc.*, vol. 107, no. 24, pp. 6801–6806, Nov. 1985, doi: 10.1021/ja00310a009.
- [161] R. G. Pearson, “Absolute electronegativity and hardness: application to inorganic chemistry,” *Inorg. Chem.*, vol. 27, no. 4, pp. 734–740, Feb. 1988, doi: 10.1021/ic00277a030.
- [162] R. Colorado and T. R. Lee, “Thiol-based Self-assembled Monolayers: Formation and Organization,” in *Encyclopedia of Materials: Science and Technology*, 2001, pp. 9332–9344. doi: 10.1016/b0-08-043152-6/01682-x.
- [163] A. Ulman, *Thin Films: Self-Assembled Monolayers of Thiols: Thin Films. Vol. 24*. San Diego: Academic Press, 1998.
- [164] A. Ulman, “Formation and structure of self-assembled monolayers,” *Chem. Rev.*, 1996, doi: 10.1021/cr9502357.
- [165] A. Ulman, *An Introduction to Ultrathin Organic Films*. Elsevier, 1991. doi: 10.1016/C2009-0-22306-3.
- [166] C. D. Bain, E. B. Troughton, Y. T. Tao, J. Evall, G. M. Whitesides, and R. G. Nuzzo, “Formation of Monolayer Films by the Spontaneous Assembly of Organic Thiols from Solution onto Gold,” *J. Am. Chem. Soc.*, vol. 111, no. 1, pp. 321–335, 1989, doi: 10.1021/ja00183a049.
- [167] J. P. Hansen and I. R. McDonald, *Theory of Simple Liquids*. Elsevier, 2006. doi: 10.1016/B978-0-12-370535-8.X5000-9.
- [168] P. B. Allen and J. L. Feldman, “Thermal conductivity of disordered harmonic solids,” *Phys. Rev. B*, vol. 48, no. 17, pp. 12581–12588, 1993, doi: 10.1103/PhysRevB.48.12581.
- [169] D. C. Rapaport, R. L. Blumberg, S. R. McKay, and W. Christian, “The Art of Molecular Dynamics Simulation,” *Comput. Phys.*, vol. 10, no. 5, p. 456, 1996, doi: 10.1063/1.4822471.

- [170] S. Merabia, J. Lombard, and A. Alkurdi, “Importance of viscoelastic and interface bonding effects in the thermal boundary conductance of solid-water interfaces,” *Int. J. Heat Mass Transf.*, vol. 100, pp. 287–294, 2016, doi: 10.1016/j.ijheatmasstransfer.2016.04.043.
- [171] M. E. Caplan, A. Giri, and P. E. Hopkins, “Analytical model for the effects of wetting on thermal boundary conductance across solid/classical liquid interfaces,” *J. Chem. Phys.*, vol. 140, no. 15, 2014, doi: 10.1063/1.4870778.
- [172] B. R. Walker, F. Alexander, and P. J. Tannenbaum, “Fanconi Syndrome with Renal Tubular Acidosis and Light Chain Proteinuria,” *Nephron*, vol. 8, no. 1, pp. 103–107, 1971, doi: 10.1159/000179912.
- [173] S. B. Soffer, “Statistical model for the size effect in electrical conduction,” *J. Appl. Phys.*, vol. 38, no. 4, pp. 1710–1715, 1967, doi: 10.1063/1.1709746.
- [174] D. Bolmatov, V. V. Brazhkin, and K. Trachenko, “The phonon theory of liquid thermodynamics,” *Sci. Rep.*, vol. 2, 2012, doi: 10.1038/srep00421.
- [175] J. Frenkel, *Kinetic Theory of Liquids*. Oxford University Press, 1946.
- [176] M. Schoenberg, “Elastic wave behavior across linear slip interfaces,” *J. Acoust. Soc. Am.*, vol. 68, no. 5, pp. 1516–1521, Nov. 1980, doi: 10.1121/1.385077.
- [177] A. Pham, M. Barisik, and B. Kim, “Pressure dependence of Kapitza resistance at gold/water and silicon/water interfaces,” *J. Chem. Phys.*, vol. 139, no. 24, 2013, doi: 10.1063/1.4851395.
- [178] H. Hu and Y. Sun, “Effect of nanopatterns on Kapitza resistance at a water-gold interface during boiling: A molecular dynamics study,” in *Journal of Applied Physics*, 2012, vol. 112, no. 5. doi: 10.1063/1.4749393.
- [179] R. N. Wenzel, “Resistance of solid surfaces to wetting by water,” *Ind. Eng. Chem.*, vol. 28, no. 8, pp. 988–994, Aug. 1936, doi: 10.1021/ie50320a024.
- [180] R. Raj, R. Enright, Y. Zhu, S. Adera, and E. N. Wang, “Unified Model for Contact Angle Hysteresis on Heterogeneous and Superhydrophobic Surfaces,” *Langmuir*, vol. 28, no. 45, pp. 15777–15788, Nov. 2012, doi: 10.1021/la303070s.
- [181] R. Lundy *et al.*, “Exploring the Role of Adsorption and Surface State on the Hydrophobicity of Rare Earth Oxides,” *ACS Appl. Mater. Interfaces*, vol. 9, no. 15, pp. 13751–13760, 2017, doi: 10.1021/acsami.7b01515.
- [182] F. M. Fowkes, “Attractive forces at interfaces,” *Ind. Eng. Chem.*, vol. 56, no. 12, pp. 40–52, Dec. 1964, doi: 10.1021/ie50660a008.
- [183] D. J. Preston, N. Miljkovic, J. Sack, R. Enright, J. Queeney, and E. N. Wang, “Effect of Hydrocarbon Adsorption on the Wetting of Rare Earth Oxides,” in *Proceedings of the 15th International Heat Transfer Conference*, 2014. doi: 10.1615/IHTC15.cds.009296.

- [184] V. H. Dalvi and P. J. Rossky, “Molecular origins of fluorocarbon hydrophobicity,” *Proc. Natl. Acad. Sci. U. S. A.*, 2010, doi: 10.1073/pnas.0915169107.
- [185] K. Yu, R. Enright, and D. McCloskey, “Monte Carlo analysis of frequency domain thermorefectance data for quantitative measurement of interfacial thermal conductance at solid-liquid interfaces modified with self-assembled monolayers,” in *Journal of Physics: Conference Series*, 2021, vol. 2116, no. 1. doi: 10.1088/1742-6596/2116/1/012042.
- [186] N. Yu and A. A. Polycarpou, “Adhesive contact based on the Lennard-Jones potential: A correction to the value of the equilibrium distance as used in the potential,” *J. Colloid Interface Sci.*, vol. 278, no. 2, pp. 428–435, 2004, doi: 10.1016/j.jcis.2004.06.029.
- [187] J. Park and D. G. Cahill, “Plasmonic Sensing of Heat Transport at Solid-Liquid Interfaces,” *J. Phys. Chem. C*, vol. 120, no. 5, pp. 2814–2821, 2016, doi: 10.1021/acs.jpcc.5b11706.
- [188] D. Deng, W. Wan, Y. Qin, J. Zhang, and X. Chu, “Flow boiling enhancement of structured microchannels with micro pin fins,” *Int. J. Heat Mass Transf.*, 2017, doi: 10.1016/j.ijheatmasstransfer.2016.09.086.
- [189] P. Darragh, K. Yu, M. Morris, D. McCloskey, and R. Enright, “Quantifying Enhanced Interfacial Thermal Conductance At Solid-Fluorocarbon Liquid Interfaces Modified With Self-Assembled Monolayers,” in *Proc. of the Int. Symp. on Therm. Effects in Gas flow in Microscale*, 2019, pp. 1–14.
- [190] C. Qian, Y. Wang, H. He, F. Huo, N. Wei, and S. Zhang, “Lower Limit of Interfacial Thermal Resistance across the Interface between an Imidazolium Ionic Liquid and Solid Surface,” *J. Phys. Chem. C*, vol. 122, no. 38, pp. 22194–22200, 2018, doi: 10.1021/acs.jpcc.8b06974.
- [191] M. A. Parra, D. Elustondo, R. Bermejo, and J. M. Santamaría, “Ambient air levels of volatile organic compounds (VOC) and nitrogen dioxide (NO<sub>2</sub>) in a medium size city in Northern Spain.,” *Sci. Total Environ.*, vol. 407, no. 3, pp. 999–1009, Jan. 2009, doi: 10.1016/j.scitotenv.2008.10.032.
- [192] A. Ito, “Spatial and temporal characteristics of urban atmospheric methane in Nagoya City, Japan: an assessment of the contribution from regional landfills,” *Atmos. Environ.*, vol. 35, no. 18, pp. 3137–3144, Jun. 2001, doi: 10.1016/S1352-2310(00)00533-1.
- [193] A. Zangwill, *Physics at Surfaces*. Cambridge University Press, 1988.
- [194] G. F. Carruth and R. Kobayashi, “Vapor pressure of normal paraffins ethane through n-decane from their triple points to about 10 mm mercury,” *J. Chem. Eng. Data*, vol. 18, no. 2, pp. 115–126, Apr. 1973, doi: 10.1021/jc60057a009.
- [195] N. Atthi, O. U. Nimitrakoolchai, W. Jeamsaksiri, S. Supothina, C. Hruanun, and A. Poyai, “Study of optimization condition for spin coating of the photoresist film on

rectangular substrate by Taguchi design of an experiment,” *Songklanakarin J. Sci. Technol.*, vol. 31, no. 3, pp. 331–335, 2009.

- [196] D. Michael and I. Benjamin, “Solute orientational dynamics and surface roughness of water/hydrocarbon interfaces,” *J. Phys. Chem.*, vol. 99, no. 5, pp. 1530–1536, 1995, doi: 10.1021/j100005a025.
- [197] W. J. Tay and J. P. M. Trusler, “Density, sound speed and derived thermophysical properties of n-nonane at temperatures between (283.15 and 473.15)K and at pressures up to 390 MPa,” *J. Chem. Thermodyn.*, vol. 124, pp. 107–122, 2018, doi: 10.1016/j.jct.2018.04.019.
- [198] H. Subramanyan, K. Kim, T. Lu, J. Zhou, and J. Liu, “On the importance of using exact full phonon dispersions for predicting interfacial thermal conductance of layered materials using diffuse mismatch model,” *AIP Adv.*, vol. 9, no. 11, 2019, doi: 10.1063/1.5121727.
- [199] Climalife, “R-245fa data sheet,” *VIN-FP-537/004*.  
<https://climalife.dehon.com/uploads/product/media/document/r-245fa-fp-en.pdf>
- [200] Q. Zheng *et al.*, “Phonon and electron contributions to the thermal conductivity of VN<sub>x</sub> epitaxial layers,” *Phys. Rev. Mater.*, vol. 1, no. 6, p. 065002, Nov. 2017, doi: 10.1103/PhysRevMaterials.1.065002.
- [201] W. Wang and D. G. Cahill, “Limits to thermal transport in nanoscale metal bilayers due to weak electron-phonon coupling in Au and Cu,” *Phys. Rev. Lett.*, 2012, doi: 10.1103/PhysRevLett.109.175503.
- [202] A. J. Minnich *et al.*, “Thermal conductivity spectroscopy technique to measure phonon mean free paths,” *Phys. Rev. Lett.*, 2011, doi: 10.1103/PhysRevLett.107.095901.
- [203] C. Chiritescu *et al.*, “Ultralow Thermal Conductivity in Disordered, Layered WSe<sub>2</sub> Crystals,” *Science (80-. )*, vol. 315, no. 5810, pp. 351–353, Jan. 2007, doi: 10.1126/science.1136494.
- [204] B. C. Gundrum, D. G. Cahill, and R. S. Averback, “Thermal conductance of metal-metal interfaces,” *Phys. Rev. B*, vol. 72, no. 24, p. 245426, Dec. 2005, doi: 10.1103/PhysRevB.72.245426.
- [205] M. Mehrvand and S. A. Putnam, “Transient and local two-phase heat transport at macro-scales to nano-scales,” *Commun. Phys.*, vol. 1, no. 1, p. 21, Dec. 2018, doi: 10.1038/s42005-018-0018-3.
- [206] M. Mehrvand and S. A. Putnam, “Probing the Local Heat Transfer Coefficient of Water-Cooled Microchannels Using Time-Domain Thermorefectance,” *J. Heat Transfer*, 2017, doi: 10.1115/1.4036691.
- [207] N. S. Saadi, L. B. Hassan, and T. Karabacak, “Metal oxide nanostructures by a simple hot water treatment,” *Sci. Rep.*, 2017, doi: 10.1038/s41598-017-07783-8.

- [208] D. M. Christopher, H. Wang, and X. Peng, "Heat transfer enhancement due to Marangoni flow around moving bubbles during nucleate boiling," *Tsinghua Sci. Technol.*, 2006, doi: 10.1016/S1007-0214(06)70229-2.